
THE UNIVERSITY *of* EDINBURGH

# Using geophysical data to understand liquid water dynamics in seasonal snow

*Alex Priestley*


*Doctor of Philosophy*

THE UNIVERSITY OF EDINBURGH

2022

# Abstract

Modelling and monitoring seasonal snow is critical for water resource management, flood forecasting and avalanche risk prediction. Snowmelt processes are of particular importance. The behaviour of liquid water in snow has a big influence on melting processes, but is difficult to measure and monitor non-invasively. Recent work has shown the promise of using electrical self potential and electrical resistivity measurements as snow hydrology sensors. Self potential magnitudes can be used to infer both liquid water content of snow and bulk meltwater runoff, and electrical resistivity is affected by liquid water content. In autumn 2018, a prototype geophysical monitoring array was installed at Col de Porte in the French Alps, alongside full hydrological and meteorological measurements made routinely at the site. Self potential measurements were taken throughout the following two winters, with manual snow pit data obtained in spring 2019. Electrical resistivity measurements were unsuccessful due to problems with power and control units. Observed self potential peaks preceded measured basal runoff peaks, indicating that self potential measurements are sensitive to water dynamics within the snowpack, most clearly during spring melting and rain-on-snow events.

A physically-based snow hydrology model (Flexible Snow Model 2.0) was evaluated at Col de Porte against observations in order to select a best-performing configuration, by utilising the ability to easily change model parameters. Three different hydrology and two density configurations were tested, as well as investigating the effect of varying the irreducible water saturation and saturated hydraulic conductivity. It was found that an irreducible water saturation of 0.03 performed best, and that changing the saturated hydraulic conductivity had little effect on performance. This snow model was then coupled to an electrical model of liquid water in snow to create a synthetic set of self potential observations. These synthetic observations were compared to the observed self potential magnitudes to evaluate the effectiveness of the model and investigate the possibility of using the self potential array as part of a coupled geophysical monitoring and modelling system. It was found that modelled self potential magnitudes are extremely sensitive to small changes in prescribed snow properties, giving large uncertainties. Timings of modelled self potential peaks were able to be related to meteorological and hydrological observations, meaning self potential measurements could be used to improve liquid water flow representation in snow models. An empirical relationship between measured self potential and modelled internal water flow was trialled, which highlighted the potential for future empirical methods to exploit self potential observations. The combination of self potential, and meteorological and hydrological measurements has highlighted the value of combining observations with models both to guide future observation networks, and improve modelling capabilities.

# Lay Summary

Snow is very important. It has major effects on the climate, billions of people depend on it for their water supply and millions of people use it for winter sports tourism every year. Snow is also hazardous: avalanches can damage infrastructure and cause fatalities, and snow can contribute to flood risk when it melts. In order to understand and predict these risks and resources, scientists use observations and computer models to look at what the snow is like on the ground, and predict how this is going to change in the days and months ahead. This allows flood and avalanche risks to be predicted, it allows water and hydroelectricity companies to plan for how much water they will have, and it allows ski resorts to manage their slopes effectively. One of the most important things about snow is the amount of liquid water there is within it, and how slow or fast this liquid moves through the snow to the soil beneath.

Liquid water in the snow is one of the main factors affecting flood and avalanche risk, but it is difficult to measure, and computer models can make errors. There are two main ways which we measure information about the snow on the ground. The first is using instruments on the ground. Some of these need people to operate them, and some are automatic. Most current techniques like this to measure liquid water in the snow are expensive, and can be time and labour intensive. These measurements tend to be accurate but are usually only available in a small number of locations due to the expense of getting them. The second way observations are made is using what's called 'remote sensing' - this means instruments are attached to aeroplanes, drones or satellites, and measurements are made from the air or from space. These techniques are able to make measurements over a much wider area than ground observations, but the trade off is that these measurements are not able to see as much fine detail.

In order to try improve both the measurement techniques for measuring liquid water in snow, and model predictions of it, two electrical measurement techniques were applied, using a prototype system at a field site in the French Alps over two winter seasons. The self potential technique measures tiny electrical voltages generated in the snow by liquid water moving. Previous work has proven this technique works in the laboratory and in the field. The second technique is electrical resistivity tomography. This technique injects an electrical current into the material of interest, and measures the electrical response. This response depends on the material, and how much liquid water is present. This technique has never been used in snow before, but it has been shown to work in permafrost. The data from these electrical measurements were used to help evaluate a computer model of the snow to improve the predictions made. The model is called 'Flexible Snow Model 2' (FSM2), and it allows easy variation of its settings to test different model configurations.

The electrical self potential measurements worked quite well, and were able to detect liquid water in the snow due to melting on sunny days and also from when it rained on the snow. This data showed that the model predicted the water movement too early compared to observations. Unfortunately, the electrical resistivity measurements were not successful. Problems with the power system and control software meant that no useful data was able to be collected. In the second season, the system was adjusted but it still didn't work.

Data from the electrical self potential measurements, alongside weather measurements made at the Col de Porte site, allowed FSM2 to be evaluated over a long period of time, and a best performing configuration selected. FSM2 was also tested over the whole region surrounding the field site, by using weather forecast data from the French national weather agency, Meteo France. This was evaluated with ground observations at Col de Porte, and with satellite data. This experiment found that FSM2 was able to produce good simulations of snow cover over the whole region, and the amount of water held in the snowpack (snow water equivalent, a common measure of water in snow) was well simulated at Col de Porte. These were both predicted using the configuration evaluated before.

In summary, the electrical potential system trialled worked well and provided some insight into movement of water in the snow. The electrical resistivity system did not work at all. The data from the electrical self potential was used alongside weather observations to evaluate a snow model (FSM2), and the settings of the snow model were adjusted using this data to improve the predictions made. The same model with the same settings was then extended to predict snow cover over a whole region, which produced good results when compared with satellite and ground observations.

# Acknowledgements

I've received a lot of help and assistance along the way, without which this project would not have been possible.

At the University of Edinburgh, thanks to Jane Blackford for letting me use the School of Engineering Cold Labs for the first trials of the array. The technical expertise of the team at the NERC Geophysical Equipment Facility (Colin Kay, Alan Hobbs and Graham Mitchell) was absolutely essential. Thank you for building my multiplexer components and lending power supplies. Several members of staff around the School of GeoSciences lent equipment and expertise, including Pete Nienow, Anthony Newton, Kate Heal and Mathew Williams, and for that I am very grateful. As the E3 DTP manager, Stephanie Robin has been incredibly helpful and accommodating, and always friendly and cheerful, which made all the essential admin a breeze.

Thanks to the staff at British Geological Survey in Keyworth for their help and expertise in building and shipping equipment, including Humphrey Barnes-Wallis, Phil Meldrum, Russell Swift and John Chambers. Thanks to Paul Wilkinson and Cornelia Inauen for their help with Python scripts and understanding ERT data.

The staff at the Centre D'Etudes de la Neige in Grenoble were fantastically helpful, accommodating and absolutely integral to this project. Thanks to Yves Lejeune, Marie Dumont, Samuel Morin, Mathieu Fructus and Matthieu Lafaysse for sharing data, model expertise, ski touring routes and espressos with me. Thanks most of all to Erwan Le Gac for spending hours with me installing, testing and commissioning kit at Col de Porte.

Thanks to my supervisory team at Swansea (Bernd Kulessa), BGS (Oliver Kuras) and Edinburgh (Richard Essery). Thanks for all your guidance and help, especially Richard, who always has helpful suggestions, and ideas of how to incorporate a trip to see some snow in real life.

Thanks to the St Kilda office sheep, whose good humour, coffees and quiz winning was a pleasure to be part of.

And finally, thanks to Jenny, without whose unwavering support this work would have been doomed long ago.

# Declaration

I declare that this thesis was composed by myself, that the work contained herein is my own except where explicitly stated otherwise in the text, and that this work has not been submitted for any other degree or professional qualification except as specified.

**Alex Priestley, April 2022**

# Published work

Part of this thesis has already been published in a peer-reviewed journal during the course of the PhD study (Priestley et al., 2021). This manuscript was written entirely by the lead author, with co-authors contributing fieldwork and laboratory assistance and research advice. Because of the structure of this thesis, the already published work was not able to be included whole as a standalone chapter. The description of the design, build and installation of the SP array, the SP results from 2019, and some of the results discussion were taken from the paper.

# Contents

# Figures and Tables

## Figures

## Tables

# Chapter 1

# Introduction

## 1.1 The importance of snow

Snow plays an important role in the hydrology, ecology and climate of Earth. Snow covers on average more than 45 million square kilometres (around 45%) of the Northern Hemisphere surface each year at maximum extent in January and February (Estilow et al., 2015). There is much less seasonal snow cover in the Southern Hemisphere, but it still covers hundreds of thousands of square kilometres in South America (Foster et al., 2009). It is estimated that one sixth of the world population rely on glacier and snow melt for water for drinking, irrigation and hydroelectricity (Barnett et al., 2005). The water stored in firn is expected to influence how quickly glacier meltwater reaches the oceans and affects sea level (Forster et al., 2014). Flooding caused by rapid snow melt is a serious contributor to overall flood risk, but snow also reduces flood risk by locking water up in the snowpack to be released to rivers slowly as snow melts through the spring and summer. Snow can also be a major hazard. It causes delays to ground and air transport, increases the number of injuries in accidents, and can damage crops and livestock. Avalanches in mountain areas are a significant risk to property, infrastructure and life, with countries spending large amounts of money on mitigating and forecasting avalanche risk. Globally, snow is important for tourism and recreation, most obviously for winter sports, but also for the attraction it provides for visitors to Arctic areas, and mountains in the summer. Snow is ecologically very important. It insulates the ground underneath it, keeping the soil much warmer than it would otherwise be, and this allows organisms to continue living under the snow throughout the winter. Snow is an important element of the climate system due to its high albedo, meaning it reflects a lot of the Sun's radiation back into space - much more than is reflected by trees and soil.

### 1.1.1 Snow in the climate system

Snow cover is an important part of the climate system, and it is included as an Essential Climate Variable by the World Meteorological Organisation (WMO, 2019). Snow cover is important because of its effects on the energy balance of the Earth. Snow has high albedo (reflectance) and it is an effective thermal insulator. The albedo of snow is important for the balance of energy at the surface. High albedo surfaces reflect more short-wave solar radiation back into space. Fresh snow can reflect up to 95% of incident solar radiation (Lehning, 2009), but albedo is reduced when snow is old or melting, or contains impurities such as dust or soot (He et al., 2019; Warren, 1984). The albedo of forested areas with snow cover is lower than that of snow-covered treeless areas; for example research in Canada found that snowy forest albedo was no higher than 0.3 (Betts and Ball, 1997). Snow's effect on the overall radiation balance is greatest in Northern Hemisphere spring, as at this time snow is at its greatest extent but solar radiation is also close to its maximum over snow covered areas (Groisman et al., 1994a)(Groisman et al., 1994b). The thermal properties of snow are important for the Earth's climate. Because snow has a large proportion of air in it, it is a very good thermal insulator. The porosity of seasonal snow ranges between around 0.40 to 0.98, corresponding to densities of around 550 kg $m^{-3}$ and 18 kg $m^{-3}$ respectively (Lehning, 2009). Fresh snow has a thermal conductivity (ability to conduct heat) approximately 10-20 times lower than ice or wet soil (Lehning, 2009). Seasonal Alpine-type snow tends to become denser nearer the base of the snowpack, which results in higher thermal conductivity. Arctic tundra snow tends to have a low-density basal layer overlain with denser wind-packed snow, which results in lower thermal conductivity than Alpine snow. This is poorly represented in some models, with consequences for simulating energy balance and permafrost dynamics in these regions (Domine et al., 2019). Understanding snow thermal conductivity has important consequences for freezing and thawing of rivers, lakes, sea ice and permafrost in mountain and high-latitude regions. Snow thermal conductivity depends on the density of the snow, and also the snow microstructure. Work by Sturm et al. (1997) and more recently by Calonne et al. (2011) and Calonne et al. (2019) has used microtomography and 3-dimensional computational modelling to understand the relationships between snow structure, density and thermal conductivity.

### 1.1.2 Snow in a changing climate

It is logical to expect that as our climate warms, the amount of snow cover will decrease. Significant decreases in snow cover duration and snow cover extent have already been observed over recent decades. For example, negative snow cover extent trends in the Northern Hemisphere were identified in all months between 1981 and 2018 in a combined dataset (Mudryk et al., 2020). Since the year 2000, decreases in snow cover and duration have been observed in 78% of mountain areas (Notarnicola, 2020). Whilst different climate models and emissions scenarios show variability in their response, all climate models used in Climate Model Inter-

comparison Project 6 predict these negative trends will continue throughout the 21st century (Mudryk et al., 2020). The Intergovernmental Panel on Climate Change Assessment Report 6 states that it is 'virtually certain' that future Northern Hemisphere snow extent and duration will continue to decrease as global temperatures rise, and that similar trends will be observed in the Southern Hemisphere. These decreases will not be evenly distributed across the globe. In maritime climates like Britain's, where snow cover is marginal, it is expected to decrease during the winter (Kay, 2016). In other parts of the world, spring snow cover is expected to be most affected (Barnett et al., 2005), whilst winter snow cover may increase in some places. This is mainly due to expected changes in precipitation amounts, and even with warming, large areas of the Earth will be cold enough to still receive snow in winter. There is a lot of uncertainty in predictions of future climate, but it is clear that snow will still play a hugely important role in the future.

### 1.1.3 Snow as a water resource

Around one sixth of the world population rely on snowmelt for their water supply (Barnett et al., 2005). This includes drinking water, crop irrigation and hydroelectricity. In a lot of areas, such as the western United States, snowmelt supports river streamflow through summer and autumn when water demand is highest, with over 50% of runoff originating as snowmelt (Li et al., 2017). Changes to snow accumulation and melt timings due to climate change threaten water supplies in catchments all over the world which rely on snowmelt. For example. in the Western USA, the contribution of snowmelt could fall by a third by the year 2100 (Li et al., 2017). These changes to snow accumulation and melt affect ecosystem productivity, groundwater recharge, flood risk, food security and wildfire hazard (Musselman et al., 2021).

### 1.1.4 Snow and ecology

Snow cover has a profound effect on ecosystems. The insulating properties of snow mean that vegetation and animals are protected from the cold underneath and within the snow pack, and some organisms actually live in the snow, such as snow worms and algae (Jones et al., 2001). The temperature of the soil, and freezing and thawing processes have a large influence on ecosystem productivity. Even a relatively shallow snow cover can moderate extremes of temperature; for example a snowdepth of only 10 cm is required for the survival of winter wheat crops in North America (Steppuhn et al., 1981). This moderation of temperature extremes by snow cover allows gas exchanges between the land surface and atmosphere to continue during the winter period (Sommerfeld et al., 1993). Small mammals are able to survive the winter by living in the relatively warm conditions under the snow. Snow cover can also affect food availability for large grazers such as caribou and reindeer, and if hard icy layers develop which prevent grazers from feeding, starvation events can occur (Vikhamar-Schuler et al., 2013).

### 1.1.5 Snow as a hazard

Snowfall and lying snow can be hazardous to life, infrastructure, livestock and crops. Mitigating these risks costs a huge amount globally. For example, in the USA snow clearance from roads and runways costs more than $2 billion annually, and delays and closures of airports cause $3.2 billion economic damage each year. (Adams et al., 2004). In mountainous regions, avalanches cause injuries, fatalities and damage to infrastructure each year. Between 1985 and 2005, about 20-30 people per year died in avalanches in North America, and about 120 per year died in Europe. In winter 2020-2021, 131 people died in avalanches in Europe (EAWS, 2021). Snow causes an increase in the number of accidents, especially road traffic collisions (Eisenberg and Warner, 2005), and increases the number of injuries from slips and falls.

### 1.1.6 Snow and tourism

Winter tourism is a huge global industry, and a large proportion of this relies on snow cover for winter sports. The ski industry is worth around $20 billion per year in the United States (Olick, 2019), with large snowsports industries in Europe, Japan and New Zealand too. In a warming climate, some ski resorts will go out of business due to unreliable snow, and others are turning to increased snowmaking to ensure snow cover for skiers and snowboarders. Snow modelling is playing an increased role in ski resort planning and preparation, especially for predicting the best times to use snowmaking equipment and how to groom snow to ensure long lasting cover, such as the work carried out during the PROSNOW project (Hanzer et al., 2020). Being able to manage snow effectively will be essential for the survival of ski resorts as the climate warms.

## 1.2 Snow structure

The structure of the snowpack is influenced by the atmospheric conditions under which the snow crystals formed, the conditions during snow deposition, and the conditions for the duration that the snow is present on the ground. The snow crystal form is influenced by the humidity and temperature when it forms, and the wind speeds during and after it reaches the ground. These factors alone result in a markedly stratified snowpack in a typical alpine situation, where the snowpack builds up over a period of months due to a sequence of snowfall events. Each of these snowfalls will occur under different atmospheric conditions resulting in differing snow grain sizes and shapes in each layer. Once snow crystals reach the ground, they immediately begin to metamorphose. This allows them to reach a lower energy state by reducing their surface area. In the absence of strong temperature gradients, this transforms snowflakes into more spherical snow grains. The speed of this transformation depends on the wind speed (when the snow is at the surface), humidity, temperature, absorption of solar radiation,

presence of liquid water, and the weight of the snow above the snow grains of interest. When liquid water is present in the snow, either due to melting, or due to rain-on-snow events, the speed of metamorphism is increased. This combination of differing snow characteristics from discrete snowfall events, and the metamorphism occurring once the snow is on the ground, typically results in a snowpack with distinct layers with different properties. Snow is also laterally heterogeneous as well as vertically. This is perhaps an obvious statement when thinking about scales of hundreds of metres or kilometres, but it is also the case on scales of tens of centimetres. These heterogeneities result from small-scale changes of microclimate due to the effects of exposure, shelter from vegetation, man-made structures or topography, aspect and ground type.

## 1.3 Liquid water in snow

The two main sources of liquid water in snow are from melting at the snowpack surface or base, and from rain falling onto the snow. The presence, or lack, of liquid water in snow is an important influence on snow structure and metamorphism, meltwater runoff speed, avalanche hazard and flood risk.

There are several parameters which describe the liquid water present in snow. The **liquid water content** $\theta_w$ is the volume fraction of water in the snow with respect to the total volume. The **water saturation** $S_w$ is the volume fraction of water in the pore space of the snowpack. Both of these measures are often expressed as a percentage. $\theta_w$ and $S_w$ are related through the porosity $\phi$, the volume fraction of pore space in the medium: $S_w = \theta_w/\phi$.

The **irreducible water content** $\theta_e$ is the residual fraction of water, compared to the whole volume of the snow, that cannot be removed from the pore spaces of the snowpack. The **irreducible water saturation** $S_{ir}$ is the volume fraction of water compared to the total pore volume which cannot be removed from the pore spaces of the snow pack. The exact value of $S_{ir}$ is poorly understood. It was found to be 0.07 in experiments by Colbeck (1974). Yamaguchi et al. (2010) found a value of 0.02, and Vionnet et al. (2012) used a value of 0.05 in the CROCUS/SURFEX model.

Water is able to flow through snow due to its granular composition, but this is complicated by snow's heterogeneous structure. This variation affects the permeability of the snow to liquid water, and thus the speed with which liquid water can percolate through the snow. Water flow is controlled by gravitational and capillary forces. Theories of liquid flow through porous media, such as from soil science, apply well to homogeneous 'mature' or 'ripe' snowpacks. This means snow that has been on the ground for long enough to undergo significant metamorphism, resulting in large (1 to 2 mm diameter) rounded grains, and is isothermal at 0 °C. This grain size is large enough to reduce the contribution of capillary forces to water movement, and

thus in mature snow, water movement is primarily governed by gravitational forces (Colbeck, 1972). The theory of Darcian flow of gravitational drainage in a porous medium can be applied to snow in these conditions, resulting in an expression for the water flux $u_w$ (m s$^{-1}$) in terms of water density $\rho_w$ (kg m$^{-3}$), snow permeability to water $k$ (s $^{-1}$), gravitational acceleration $g$ (m s $^{-2}$) and viscosity of water $\mu_w$ (kg m$^{-1}$ s$^{-1}$ ):

$$u_w = \frac{\rho_w k g}{\mu_w}$$

Permeability of snow $k$ depends on the density $\rho_s$ and mean grain diameter $d$ (m). The most commonly used formulation was developed by Shimizu (1970):

$$k = 0.077 d^2 \exp\left[-7.8(\rho_s/\rho_w)\right]$$

More recent work by Calonne et al. (2012) related snow permeability to specific surface area (explained below) and snow density.

Of course, snow is frequently not homogeneous and large-grained, and water flow is usually more complex than simple gravitational drainage. Water flow in dry snow, either from rain-on-snow, or from surface melt flowing into colder layers in the snowpack, is generally slower to reach the base of the snowpack than that in wet snow. Firstly, water entering dry snow must provide enough thermal energy to bring the snow up to 0°C. Secondly, enough water must enter the snow to bring the water saturation up to the irreducible water saturation $S_w$ (Colbeck, 1976). Only once these conditions have been met is downward percolation of water by matrix flow possible.

Preferential vertical flow paths contribute to the complex nature of water movement, which can mean more efficient water transport to the base of the snowpack than is possible with matrix flow (Katsushima et al., 2013; Schneebeli, 1995). Würzer et al. (2016) looked at how snowpack and meteorological conditions affect runoff from rain-on-snow, finding that colder and drier midwinter snowpacks are more likely to increase lag time between rain and catchment response, whereas with ripe spring snowpacks catchment response is more likely to be increased.

Flow varies greatly in the horizontal plane too. When a layer with small grains overlays a layer with large grains, a capillary barrier will exist at the boundary (Mitterer et al., 2011; Peitzsch et al., 2008). Lateral flow can develop along these capillary barriers, and also along ice lenses and very dense layers.

## 1.4 Observing snow

As described above, snow is a complex and heterogeneous material whose properties change over time. Therefore, it is important to understand these properties through measurement. These properties are measured on differing scales, from microscopic to hemispheric, using a huge variety of instruments and sensors. These instruments range from simple manually-operated tools to advanced sensors mounted on satellites.

### 1.4.1 Ground-based snow measurement

A manual snow pit is the traditional method used to gain a vertical profile of snowpack properties. It involves excavating a pit with a smooth vertical wall, and making measurements of snow properties up this vertical face. It is a labour-intensive and time consuming task, and is a destructive measurement. A standard method of carrying out a full snow pit has been codified in the International Classification of Seasonal Snow on the Ground (Fierz et al., 2009). Some of the following measurement methods are used in snow pits, and some are used independently.

**Snow depth (*d*)** is simple to measure manually or using automatic instruments, but snow depth varies considerably over small distances due to wind redistribution of snow, shelter from buildings and trees, and different rates of melting. It is measured manually using a ruler or pole, either inserted vertically into the snow, or by reading off the depth to which a pre-marked pole is buried. Automatic instruments typically send a laser or ultrasound pulse vertically downwards from a fixed height, and measure the changing height of the snow surface to calculate depth. As well as the same uncertainties associated with snow depth variations as manual measurements, automatic measurements can suffer from errors due to ground heave or vegetation growing and being mistaken for snow.

Terrestrial Laser Scanners (TLS) have been used to measure snow depth, for example by Revuelto et al. (2017). Typically, a snow-free high-resolution Digital Elevation Model is created, then repeat scans of the same location are carried out when snow is present. As long as the repeat scans are correctly georeferenced onto the original snow-free scan, it is possible to subtract one from the other to gain a detailed map of snow depth over a large area. Using a TLS is only possible in clear dry weather conditions, which are often infrequent in mountain environments, meaning data acquisition can be difficult.

**Snow density** ($\rho$) is the mass of snow in a given reference volume. Density is measured manually using an extractor of a known volume which is then weighed. This is sometimes a ‘snow tube’ which is a cylindrical tube of known diameter, with a serrated end to cut a core sample of the snowpack. This core is then weighed to calculate a bulk density. If a profile of density is required through the snowpack, such as from a snow pit wall, a smaller snow cutter of a known volume is used. These are often triangular metal wedge cutters, but other

shapes are used too. Dielectric techniques infer the density (or liquid water content) of snow by measuring the relative permittivity (complex dielectric constant) of the snow. Empirical relationships are then used to calculate the snow density. These techniques are quicker than using density cutters or snow tubes. Common instruments include Finnish snow fork (Tiuri et al., 1984) and the Denoth meter (Denoth, 1994). Both of these sensors require the probe to be inserted into the snow, usually in the vertical wall of a snow pit, and thus they are destructive measurements.

**Snow grain type** and **snow grain size** are typically measured by hand during the excavation of a snow pit (Fierz et al., 2009). A profile of snow grain type and size is measured up the wall of the snow pit. A hand lens is used to classify the grain type. Snow grain size is usually estimated by placing a sample of the snow layer onto a card marked with a measurement scale. **Snow hardness** is measured by hand by applying pressure with the hand into the snow layer, first using a clenched fist, then fingers, a pencil and then a knife blade (Fierz et al., 2009). The accuracy of this 'hand hardness' test varies between observers (Pielmeier and Schneebeli, 2003). **Snow layer heights** are assessed by eye, generally using grain size, shape, snow density and snow hardness to differentiate layers. These measurements are subjective, so more objective measures of grain shape, size and snow hardness and layer thickness have been sought.

Near-infrared (NIR) photography can be used to record small-scale layering in snow (Tape et al., 2010). Snow **specific surface area (SSA)** is the ratio between surface area and volume of the ice phase of the snow. SSA is an important parameter for characterising metamorphism, and it determines the snow's radiative properties. SSA is related to the effective diameter of the snow grains, and can be used as a more objective measure of grain size. SSA can be measured using microtomography (Schneebeli and Sokratov, 2004), NIR photography (Matzl and Schneebeli, 2006) and specialist instruments such as DUFISS (Gallet et al., 2009).

**Snow temperature** is measured at regular intervals up the wall of a snowpit (Fierz et al., 2009) with a thermometer. Snow temperature is important for snow metamorphism and snowmelt percolation. Strong temperature gradients, such as those at the surface or base of a cold snowpack, can lead to growth of weak layers which can be important influences on avalanche risk. **Snow thermal conductivity** determines the temperature gradient, but is difficult to measure and can be anisotropic. Thermal conductivity can be measured using needle probes or heat flux plates, or can be simulated numerically if the 3-D microstructure of the snow is known (Riche and Schneebeli, 2013).

Instruments to measure the snow hardness objectively include the rammsonde and Snow MicroPen. The rammsmonde is similar to a cone penetrometer used in soil science, with a cone-shaped head attached to a rod which guides a hammer weight. This hammer is dropped from varying heights and with varying weights attached to it, and the depth of penetration, weight of the hammer and height from which it is dropped can be combined to calculate an in-

dex of snow hardness, the 'Ram Index' (Pielmeier and Schneebeli, 2003). The SnowMicroPen (SMP) measures snow hardness at high resolution by pushing a metal rod with a pointed end with a pressure transducer through the snowpack. Snow properties are related to the resistive force measured by the transducer through empirical relationships (Schneebeli et al., 1999) and related to hand hardness (Pielmeier and Schneebeli, 2003). The SMP has also been used to determine snow particle type and layering (Havens et al., 2013), and SSA and snow density (Proksch et al., 2015).

**Snow water equivalent (SWE)** is a point measurement of the depth of water that would be created if all the snow melted. SWE is defined as $d\bar{\rho}$ where $\bar{\rho}$ is the mean density of the snowpack. SWE is typically reported in mm or kg $m^{-2}$. SWE is manually measured using snow tubes to measure bulk density and poles to measure depth, which are then combined to give SWE. Automatic monitoring of SWE at fixed locations can be carried out using pressure transducers. The most common for of these instruments is the 'snow pillow', such as those used throughout the United States in the 'SNOTEL' network. Snow pillows consist of a pressure transducer filled with a liquid antifreeze chemical. The mass of snow on top of the snow pillow is calculated by measuring changes in fluid pressure. Snow pillows are liable to damage by large animals and frost-heave. Load cells can also be used, where a plate is suspended on load cells and the weight of the snow is measured. It is possible for errors to develop due to ice layers in the snow pack bridging across the snow pillow or load cell plates, affecting the measured snow mass.

It is possible to measure SWE using cosmic ray counters. A sensor is placed at the ground surface, and measures the count of cosmic rays reaching it. The amount of cosmic radiation reaching it is attenuated by the snowpack present. Following some site specific corrections and providing a snow-free measurement is available to use as a baseline, SWE can be automatically monitored with uncertainty of around 10% (Kodama et al., 1979; Morin et al., 2012).

Recent work by Pritchard et al. (2021) developed a method of using pressure sensors under lake ice to measure the mass of the snow on the frozen lake and, given the surface area and these water pressure measurements, calculate SWE.

Global Positioning System (GPS) satellite receivers have been used to monitor bulk snow properties (Koch et al., 2019,1) such as SWE, density and bulk liquid water content. By mounting one sensor above the snow, and one beneath the snow on the ground, these snow properties can be measured using the attenuation of the GPS signal between the two sensors. These measurements were non-destructive and provided continuous records of snow properties for several seasons.

Upward-looking Ground Penetrating Radar (upGPR) has also been used to monitor snow properties. For example, Sundström et al. (2012) were able to reduce errors in estimates of SWE in wet snow using upGPR measurements, and Mitterer et al. (2011) and Heilig et al. (2018,1) carried out experiments over several seasons monitoring snowpack stratigraphy and meltwater percolation. Schmid et al. (2014) used upGPR to estimate volumetric water content of snow, SWE and other snow properties. GPR has also been used to measure snow properties in transects across snow covered areas by being towed behind a snowmobile or mounted on a gondola (Kinar and Pomeroy, 2015).

Measuring **snowmelt runoff** at the base of the snowpack is relatively straightforward using a lysimeter (Kinar and Pomeroy, 2015). A lysimeter consists of a collecting surface of a known area typically flush with ground level, and a method of measuring water which flows through the collecting surface, such as a tipping bucket rain gauge. Kattelmann (2000) describes how lysimeters can be used to verify snow hydrology models.

The **liquid water content (LWC)** of the snowpack can be difficult to measure. A rough estimate can be gained by performing the 'hand' or 'snowball' test to see how sticky or wet the snow is. This puts the LWC into one of five bands between 0% and $>$15%. Calorimetric methods relate changes in heat content of a snow sample due to a phase change. Freezing, melting and heating calorimetry techniques have been used to measure the liquid water content. They can be time consuming and some set-ups are not suited to field applications. Typically these methods can measure liquid water content to within a few %.

Dielectric methods are commonly used to measure liquid water content, such as the Denoth Meter and Finnish snow fork that are described above. Other dielectric methods include the Snow Pack Analyzer (Sommer and Fiel, 2009), Time Domain Reflectometry (Pérez Díaz et al., 2017; Schneebeli et al., 1998; Stein, 1997) and capacitance measurements (Avanzi et al., 2016). Most of these methods are manual i.e. they require an observer to make the measurement, and are destructive. When longer-term monitoring has been tried, problems with air gaps between sensors and the snow have caused errors in the measurements. For example, the Snow Pack Analyzer uses a ribbon as a waveguide, but this ribbon can be prone to vibration when exposed to the wind, which creates a cavity around it.

Dye tracing experiments can be used to study meltwater routes within the snow (e.g. Campbell et al. (2006); Peitzsch et al. (2008); Schneebeli (1995); Williams et al. (2010)), and profiles of relative saturation can be measured with dielectric techniques mentioned above. Dye tracing experiments are time consuming, destructive and not suited to automatic monitoring.

Temperature measurements can be used to infer the water content of firn or snow such as in work by Humphrey et al. (2012); Marchenko et al. (2021); Pfeffer and Humphrey (1996) using strings of thermistors in a profile through the snowpack. These methods are able to detect when water starts moving through the snow, but are unable to monitor how much water is moving once the snowpack reaches 0 °C.

**Snow cover fraction**, when observed from the ground (see below for remote sensing) is typically estimated by an observer as the fraction of a given area covered by snow, and can be carried out remotely using webcams. It is sometimes reported at staffed synoptic meteorological stations.

### 1.4.2 Remote sensing

Remote sensing of snow includes measurements made from satellites orbiting the Earth, and measurements made from aircraft and drones. Satellite remote sensing of snow has a long history, with the first routine snow mapping begun by the National Oceanic and Atmospheric Administration (NOAA) in the USA in 1966. **Snow Cover Extent (SCE)** can be mapped using satellite imagery due to snow's high albedo compared to other natural surfaces. When SCE is mapped over seasonal timescales **Snow Cover Duration** for given locations can be derived. Earlier efforts at mapping snow using satellites produced datasets with spatial resolution of a few kilometres. The launch of the Landsat series of satellites in 1972 made higher resolution datasets possible, with Landsat-1 having a resolution of 80 m. Landsat-8, launched in 2013, has a resolution of 15 m. Landsat's higher resolution makes basin-specific snow mapping possible. Cloud cover is a major constraint, especially in mountainous areas. The repeat-pass interval of 16-18 days is not adequate for some snow mapping requirements, especially during snowmelt when snow can change significantly on diurnal timescales. The MODIS instruments launched by NASA in 1999 and 2002 provide daily snow map products for the whole globe at 500m resolution.

By comparing visible and Near Infra-Red (NIR) or Short-Wave Infra-Red (SWIR) images, processing algorithms are able to differentiate between snow and cloud. This is called the Normalised Difference Snow Index (NDSI). Using it, algorithms are able to produce maps of snow extent automatically.

Agencies in the USA such as the NOAA National Climate Data Center, and Satellite Data and Information Service, collate and produce snow and ice extent maps using several satellites, including MODIS, the European Meteosat Second Generation (MSG), AMSU and GOES.

**SWE** is an important property that can be measured using spaceborne remote sensing techniques. The presence of snow on the ground affects the strength of the local gravitational field. Data from the Gravity Recovery and Climate Experiment (GRACE) satellite has been used to estimate SWE over regional or large basin scales (e.g. Frappart et al. (2011); Niu

et al. (2007)). Passive microwave sensors are used to produce maps of snow depth and SWE on a daily basis at a global scale with a resolution of tens of kilometres. The microwave signal emitted by the underlying soil is attenuated by the snow cover. Microwave retrievals of SWE or snow depth are subject to uncertainties caused by differences in snow grain size spatially and temporally. Models have been developed to predict the snow grain changes through the course of a season (e.g. Brun et al. (1992)). Measurements are also subject to errors due to heterogeneities in land cover and topography, such as in forests or mountainous regions.

Active microwave data from satellite instruments can be used to measure SWE and snow depth through the relationships between the snowpack and the backscattering coefficients (e.g. (Hallikainen et al., 2003; Tedesco and Miller, 2007)). Synthetic Aperture Radar (SAR) can also be used to make SWE and snow depth retrievals, using the ratio of scattering over snow-free ground to snow-covered ground. SAR is not affected by daylight and retrievals can still be made under cloudy conditions. It is possible to differentiate between wet and dry snow due to the differing scattering properties of ice and liquid water (Tsai et al., 2019).

**Snow albedo** and **snow grain size** can be measured by spaceborne instruments. Snow's reflectance in the visible range of the spectrum depends on the presence of pollutants. Fresh unpolluted snow's albedo is high and does not vary much with grain size, whereas in the near infra-red (NIR) range grain size has a greater effect. This means that effective grain size can be measured using the difference between visible and NIR measurements (e.g. Kokhanovsky et al. (2011); Zege et al. (2011)).

Light Detection and Ranging (LiDAR) can be used to create high resolution maps of snow depth. This is possible both from instruments flown on aeroplanes, and instruments on satellites. LiDAR is an active measurement technique where an emitted laser pulse is reflected off the ground, vegetation and snowpack. The time-of-flight is measured, then the range of the reflector can be calculated. To calculate high-resolution snow depth maps, a snow-free and a snow-covered scan are required. Airborne LiDAR systems typically have a vertical sensitivity of tens of cm, and a horizontal resolution of one metre (Deems et al., 2013).

Photogrammetry is also used to measure snow depth from the air and space. To create a snow depth map using this technique, at least two photographs from different positions are needed. By identifying common points between the photographs, a digital elevation model can be created using triangulation. Similarly to LiDAR scans, the 'snow-on' data are then compared with the 'snow-off' data, and snow depth can be calculated. For example, airborne photogrammetry conducted alongside a conventional LiDAR system showed a mean difference between the two techniques of 0.17 m at 1 m horizontal spacing (Meyer and Skiles, 2019). Spaceborne photogrammetry using Pleiades stereo satellite imagery was able to generate maps of snow depth over mountainous terrain with a grid spacing of 3 m with an error of 0.8 m (Deschamps-Berger et al., 2020).

To map wet snow extent and snow melting, thermal and microwave channels can be used. Thermal channels can provide a Land Surface Temperature measurement, which is used to replace in situ surface temperatures e.g. Hall et al. (2013). Where the surface temperature is above a threshold (usually 0°C), snow or ice melting is diagnosed. In the microwave range of the spectrum, the dielectric properties of snow vary between dry and wet snow. This different response can be exploited to differentiate between the type of snow cover. Microwave data has been available for several decades which has allowed long time series of melt onset date to be compiled (e.g. Takala et al. (2009); Tedesco and Monaghan (2009); Wang et al. (2011)).

## 1.5 Electrical self potential (SP)

Electrical self-potential measurement is a well-established technique in environmental and earth sciences. It is a passive electrical method, which measures the electrical potentials generated through several mechanisms in the medium of interest. Self-potential measurements are useful in the respect that they measure a signal caused by dynamic processes within the material of interest, rather than structural contrasts like many active geophysical techniques such as seismic refraction and electrical resistivity tomography. Self-potential methods are unique in their ability to measure and map subsurface water flow non-destructively over large areas. This is inherently difficult to measure, even with borehole sensors in subsurface aquifers for example, and as such, the self-potential method can be particularly useful in this respect.

### 1.5.1 Applications of self potential in Earth and cryospheric sciences

Self potential measurements have been used to answer a wide variety of research questions, including locating backfilled mineshafts (Wilkinson et al., 2005), locating sinkholes in karst landscapes (Jardani et al., 2006), characterising water flow in dams (Moore et al., 2011) and monitoring volcanoes (Di Maio et al., 1997; Friedel et al., 2004). In longer term monitoring studies self potential has been used to study subsurface hydrology (Hu et al., 2020), landslides (Colangelo et al., 2006) and water flow around trees (Gibert et al., 2006; Voytek et al., 2019). In the cryospheric sciences, self potential has been used to investigate subglacial drainage (Kulessa, 2003), glacial moraine dam drainage (Thompson et al., 2012) and permafrost (Weigand et al., 2020).

Work by Kulessa et al. (2012) developed a framework for modelling self potential signals in laboratory snow experiments. A model relating snow properties, meltwater fluxes and the self potential signals was developed and tested by melting snow in controlled conditions, and measuring the resulting self potential signals. This approach was then extended to field ex-

periments on glacial snow cover by Thompson et al. (2016), who were able to map meltwater flux and liquid water content in melting supraglacial snowpacks in Switzerland. Clayton (2021) presented snowmelt flux data calculated from self potential signals in snow over a few days, albeit with large discrepancies when compared with surface energy balance model results.

### 1.5.2 Theory of electrical self potential in snow

Snow typifies a porous medium in which there are ions freely diffusing along with bulk meltwater flow in the pore space, and ions contained within an electrical double layer at the interface between the pore space and the solid matrix composed of ice grains (Kallay et al., 2003; Kulessa et al., 2012). The inner layer contains ions that are electrochemically bound to the solid surface, creating a surface charge fixed onto the ice grains. The outer layer contains ions attracted electrostatically to these surface charges but which, due to electromagnetic interactions, can be dragged along with bulk meltwater flow to create a streaming current. The divergence of this current generates a quasistatic electric field known as the streaming potential (Kulessa, 2003; Revil et al., 2017,0; Sill, 1983) that can be measured with an electrode array.

Other sources of potentials can be identified: electrochemical, thermoelectric and telluric. Electrochemical potentials are caused by electrical charge separation in chemical concentration gradients (Doherty et al., 2010; Kulessa, 2003; Revil et al., 2010). Thermoelectric potentials are caused by temperature gradients leading to differing ion mobilities through the pore fluid, effectively creating chemical potentials. Telluric potentials are caused by large-scale magneto-telluric currents in the Earth's upper atmosphere, which induce currents in the subsurface (Chave et al., 2012; Egbert and Booker, 1992; MacAllister et al., 2016).

## 1.6 Electrical resistivity tomography (ERT)

Electrical resistivity surveying is an active geophysical technique, where a current is injected into the medium of interest with a pair of electrodes. The potential difference which is generated by this injection is measured with a second pair of electrodes. This potential difference, or voltage, is related to the resistivity of the material. Resistivity is a measure of the ability of a material to oppose charge, in units of Ohm metres ($\Omega$m). In the Earth's subsurface, the electrical current is conducted primarily through the movement of ions in fluid within the pores of the medium, therefore resistivity is chiefly related to how much fluid is present, and what the fluid is made up of. Multiple measurements are made in varying combinations from an array of electrodes, and mathematical inversion of the measurements can be used to create an image of the resistivity of the subsurface. This method of surveying was first used in the 1920s, with simple one-dimensional survey geometries. In recent decades, two, three and four dimensional surveying techniques have been developed, and the technique

is now often known as Electrical Resistivity Tomography (ERT). Multiple measurements are made in varying combinations from an array of electrodes, and mathematical inversion of the measurements can be used to create an image of the resistivity of the subsurface. It has wide applications in exploration and site investigation for engineering and environmental fields (Chambers et al., 2007; Kuras et al., 2016; Rucker et al., 2010), archaeology (Tsokas et al., 2008), hydrology (French and Binley, 2004; Miller et al., 2008) and mineral exploration (Bauman, 2005; Legault et al., 2008). Longer term monitoring has been used to investigate leakage from nuclear waste storage (Kuras et al., 2016) and landslides affecting transport infrastructure (Holmes et al., 2020).

In snow and ice, glacial or snow meltwater can actually be highly resistive. In dry snow or ice, conduction happens via the movement of protonic point defects (Kulessa, 2007; Stillman et al., 2013). Temperature and the presence of impurities are important controls on conduction.

In the cryospheric sciences, ERT has been used to monitor permafrost freezing and thawing in laboratory conditions (Murton et al., 2016), for studying permafrost depth and degradation (e.g. (Mollaret et al., 2019; Uhlemann et al., 2021)) and for studying subglacial drainage in moraines and subglacial boreholes (Kulessa et al., 2006; Thompson et al., 2012,1). It has also been used to monitor snowmelt infiltration into soil beneath the snowpack (French and Binley, 2004). There appear to be no papers in the literature describing an attempt to use ERT to monitor snow properties.

## 1.7 Snow modelling

### 1.7.1 Snow model usage

The importance of understanding the state of the snowpack for society is outlined above, as are the limitations in our ability to observe snow properties from the ground, the air and from space. Complex topography, tree and cloud cover, rugged terrain and poorly developed ground observing networks often coincide with areas with significant snow cover such as mountain areas and the high latitudes. These gaps in our observational capability mean that in order to understand the state of snow cover in these regions it is essential to use models to complement existing observations.

Snow models are used in a wide variety of contexts. They are used by hydrologists to predict how much runoff will be generated as snow melts to understand flood risk and help water resource planning for drinking water, irrigation and hydroelectricity. The importance of the effects of snow cover on weather and climate mean that if models used for numerical weather prediction or climate simulations do not represent the snow cover, large errors can develop. Models are also used widely in avalanche forecasting both for mitigating risks to infrastructure, and for people engaging in leisure activities in mountain areas.

### 1.7.2 Snow model types

Snow models can be split into two broad categories: temperature index or degree-day models, and surface energy balance models.

#### Temperature index models

Temperature index models simulate snow or ice accumulation and ablation using just the observed or forecast precipitation and temperature (Ohmura, 2001; Sicart et al., 2008). The simple data requirements mean limited observational data or simple output from numerical weather prediction models are sufficient to run them. This simplicity means they are computationally efficient to run, and are thus suited to distributed modelling or ensemble simulations. Temperature index models are used widely in operational hydrological contexts, and for glacier surface mass balance modelling. The individual surface energy fluxes are not explicitly represented, and are instead parameterised as a function of air temperature. The rate of snowmelt is defined as being proportional to the temperature above freezing point per unit time. The constant relating temperature to melt amount is usually termed the 'degree-day factor' and can be kept constant in both space and time (e.g. Valéry et al. (2014)). Slightly more complex formulations include a varying degree-day factor, either varying seasonally or monthly (e.g. Hottelet et al. (1994)), or varying spatially. This can take into account the slope, aspect or vegetation cover of the catchment (e.g. He et al. (2014)). Most models use 0°C as the threshold temperature for the onset of snowmelt (Todd Walter et al., 2005) but some use a calibrated threshold to account for spatial variations in this process (Viviroli et al., 2009). Different ways of partitioning precipitation into rain and snow are used. Some models use a sharp cut off temperature, others use a gradual transition where rain and snow are permitted at the same time, and some use additional data such as relative humidity.

As mentioned above, the main advantages of temperature index models are their computational simplicity and data requirements. When calibrated they can produce very good predictions of snowmelt runoff. Their main limitations are that they do not represent any internal processes in the snowpack, such as metamorphism and water transport, which affect the speed of melting. They also do not generally represent wind transport or sublimation so can be liable to over-predict lying snow especially in windy and dry climates. Uncertainties can develop in predictions due to precipitation partitioning, which has more potential to cause differences at lower-altitude sites or at the beginning or end of the winter when temperatures are more likely to be near zero.

### Energy balance models

Energy balance models represent more processes explicitly than temperature index models. They include representations of the mass and energy exchanges at the snow surface, and at the interface between the snow and the ground. Surface energy balance models can represent snow accumulation and ablation, compaction, albedo, temperature, sublimation and liquid water retention and refreezing processes. Internal snowpack processes are treated either by representing the snow as a single layer (e.g. Douville et al. (1995); Dutra et al. (2010,1); Gouttevin et al. (2012)), or as a multi-layer system (e.g. Brun et al. (1989); Lehning et al. (1999); Vionnet et al. (2012); Wang et al. (2013)). Energy balance models are widely used operationally by hydrological services, in Earth System Models for numerical weather prediction, and for avalanche forecasting. Early single layer models represented the soil and snow as a single layer, including in this representation processes occurring in the snow itself, the soil, vegetation, and interactions with the atmosphere. These models have mostly been superseded by explicit single-layer models, which represent a separate energy balance for the snow. In these explicit single-layer models internal snow processes are not usually considered, but bulk or surface quantities are represented such as surface temperature, albedo, density, depth and SWE.

In multi-layer models, these bulk and surface quantities are represented, in addition to internal layer quantities such as density, layer thickness, temperature and liquid water content. This allows the calculation of vertical fluxes of liquid water, heat conduction and snow compaction. Water retention is often represented by treating each model snow layer as a ‘bucket’ with a finite water holding capacity. When this capacity is reached water moves to the layer below. This layer water capacity can be adjusted according to snow properties and layer depth. Some models account for horizontal advection of wind-blown snow (Liston et al., 2007; Pomeroy et al., 1993). In the most detailed multi-layer models, snow metamorphism is represented, including grain size evolution. Layer boundaries can be kept at fixed heights, such as in FSM (Essery, 2015) and SNTHERM (Jordan, 1991). Lagrangian frameworks where the number, thickness and position of layer interfaces evolve with time are also used, such as in Crocus (Vionnet et al., 2012) or SNOWPACK (Lehning et al., 1999). These models were developed primarily for avalanche hazard prediction, where interfaces between layers are especially important.

### 1.7.3 Data requirements for snow modelling

Temperature index models have simple data requirements, as they generally only require air temperature and precipitation amount to run. These simple requirements mean it is easy to run them at a wide variety of sites with basic instrumentation or numerical weather prediction output. Surface energy balance models generally require more data to run than temperature index models. In addition to precipitation and air temperature, incoming radiation (short and long wave), air pressure, humidity and wind speed are usually required. These greater data requirements mean that fewer locations have the requisite observed data available than for temperature index models. Long period observational datasets are available which have been specifically compiled for the testing and verification of surface energy models, such as at Col de Porte in France (Lejeune et al., 2019) and Sodankyla in Finland (Essery et al., 2016). It is also possible to run energy balance snow models using numerical weather prediction model data as either forecast data for the future, or reanalysis data from the past, such as by Alonso-González et al. (2021).

### 1.7.4 Current state of the art in snow hydrology modelling

Some key areas in the recent development of snow hydrology models have been improving quantification and understanding of model uncertainty, improving representation of internal snow processes such as water percolation and vapour transport, and improving data assimilation, especially of remotely-sensed data (covered in 1.4.2).

Improvements of water movement in the snowpack have centred on representing preferential flow, rain-on-snow processes and water retention in the snowpack. Work to improve the representation of water retention has led to improved model predictions of capillary barriers between layers of differing properties, such as in Hirashima et al. (2010). Following on from this work, the Richards equation (Richards, 1931) which describes water movement in porous media, was implemented in the SNOWPACK model resulting in improved meltwater runoff simulations (Wever et al., 2014). When compared to the usual bucket water-retention scheme (see above), the implementation of the Richards Equation performed better, but was around 1.5 - 2 times more computationally expensive (Wever et al., 2015). Clark et al. (2017) developed a test case for snow models which solved water transport equations (in idealised conditions) analytically rather than numerically.

Lateral differences in snowmelt percolation have been represented in models. Katsushima et al. (2009) represented vertical preferential flow channels resulting from rain-on-snow events in a multi-layer snow model. Würzer et al. (2017) modified the Richards equation implementation in SNOWPACK (Wever et al., 2014,1) to account for preferential flow during rain-on-snow events. In these studies, model predictions were improved by representing preferential

flow. These studies parametrised preferential flow in a 1-dimensional framework. Leroux and Pomeroy (2017) ran a 2-dimensional model which represented heterogeneous flow through a layered snowpack. This improved representations of warming a snowpack during melting, and was able to predict the development of ice layers.

Work to understand uncertainty in snow model predictions has compared different snow model performance, and quantified uncertainty in individual models due to model structure, parameterisations and forcing data errors. The Earth System Model Snow Model Intercomparison Project (ESM-SnowMIP) (Krinner et al., 2018) aims to quantify uncertainties in a wide range of snow models from across the globe by running them with the same forcing data for the same sites. Similar smaller-scale work in the past has shown that no single model can perform well at all sites in all years (Etchevers et al., 2004). Günther et al. (2019) evaluated a large number of model simulations over a long time period for a site in the Austrian Alps. They found that driving data errors had the largest effect on model performance, with model structure the next biggest factor, followed by parameter choice.

Some snow models have been explicitly designed to investigate the effect of changing parameterisations of processes. The JULES Investigation Model (JIM) was used to investigate how 1701 configurations of model parameterisations affected snow simulations at an Alpine site (Essery et al., 2013). It was found that the best performing models took account of changes to surface albedo and density, and simulated water storage and refreezing. Following on from this, Essery (2015) developed the 'Factorial Snow Model' (FSM) that enabled 5 key processes to be parameterised in 2 different ways, thus giving 32 possible model configurations. The second iteration of this model (FSM2) allows more complex parameterisations to be used, such as numerical solutions to water movement, and three levels of density representation. It is possible to run FSM as an ensemble and compare the spread of results. Similar work was carried out using the French snow model CROCUS in an ensemble configuration (ES-CROC) (Lafaysse et al., 2017). It was found that optimal members of the system were able to account for a large part of the observed uncertainty in snow variables. None of these ensemble approaches outlined above account for driving data uncertainty, which was found by Günther et al. (2019) to be the most important influence on model uncertainty. Using ensemble NWP output to run ensemble snow models could help understand this uncertainty.

Chapter 2

# Knowledge gaps, research aims and thesis structure

## 2.1 Knowledge gaps

Chapter 1 outlines the scientific community's current understanding and capabilities for observing liquid water in snow. Whilst considerable effort has been made to advance our ability in this area, gaps in this knowledge and capability exist, chiefly around our ability to monitor water motion in snow non-destructively, and in a long term (for a season at a time or longer) framework. Current methods are generally either expensive to install, destructive, require intensive manual operation, or do not provide data at a high enough resolution, or a combination of these factors.

Existing liquid water measurement techniques currently employed include GPS sensors, up-GPR, lysimeters and dielectric sensors, as described in section1.4.1. These techniques are subject to the pitfalls listed above. No system has successfully been shown to be able to detect water motion within the snow over a seasonal timescale without manual intervention or destructive measurement. Another factor motivating the progress of exploiting this gap in our capability is cost: if a low-cost method can be shown to work, then wider usage in large enough numbers to gather information across whole mountain catchments or even mountain ranges becomes more possible.

Electrical self potential measurements have been shown to be useful snow hydrology sensors in work by Clayton (2021); Kulessa et al. (2012); Thompson et al. (2016), but work so far has not attempted monitoring over longer than a few days. ERT has not been used as snow sensor, but work with rock freezing and thawing (Murton et al., 2016) and other cryospheric applications (Mollaret et al., 2019; Uhlemann et al., 2021) and those noted above has encouraged an attempt to apply it to snow. Resistivity is controlled partly by temperature, so ERT should be able to detect when the snow is isothermal at 0°C and able to support liquid flow.

The state of the art of snow hydrology modelling is also outlined in Chapter 1. Despite recent advances in representation of liquid water flux in snow models, such as representations of preferential flow (Katsushima et al., 2009), implementing Richards equation (Wever et al., 2014), and moves towards flexible and ensemble modelling frameworks (Lafaysse et al., 2017), there is still a need for development and evaluation of models which represent water movement as realistically as possible, and are able to be run quickly and easily while assessing the effect of parameter selection. Work to assess the influence of choice of parameters in snow models has been carried out previously, using models designed for this purpose. Using large numbers of model configurations made analysis difficult (Essery et al., 2013), or ensemble methods were used which involve complex perturbations of the initial conditions (Lafaysse et al., 2017). Distributed snow modelling over large areas, such as whole catchments or mountain ranges, has generally been carried out using low fidelity models (such as temperature index models - see section 1.7.2), or simpler energy balance models. There is a need to carry out evaluation of state-of-the-art physically-based snow hydrology models in a distributed framework. FSM2 is quick to run and allows the switching of parameters easily so is ideally suited to this task. While there has certainly been some success with modelling liquid water motion (section 1.7.4) by using Richards equation in water drainage schemes (Richards, 1931), implementations such as that by Wever et al. (2014) found numerical instability caused some issues, and SNOWPACK is in any case not a modular model allowing easy comparison of the effect of parameter choice. Using a different approach, solving the equations of water motion analytically worked using idealised examples for Clark et al. (2017), but has not been implemented for real snow. The development of insights gained using JIM (Essery et al., 2013) and from model intercomparison projects e.g. (Krinner et al., 2018) led to the development of Factorial Snow Model (Essery, 2015) which allowed the switching on and off of what were found in previous studies to be the most influential parameters (Essery et al., 2013). There is now a need to use an extended version of Factorial Snow Model, FSM2, (currently unpublished) to evaluate the performance of different model parameter choices at a fully instrumented site with a long observational record. Limited modelling of electrical signals in snow has been carried out, with Kulessa et al. (2012) and Thompson et al. (2016) being the main examples. However, these studies did not combine snow hydrology modelling and electrical measurements in a coupled framework, which is key to both evaluation of the geophysical methods, and model representations of liquid water which cannot be measured directly.

## 2.2 Research aims

Based on the discussion of knowledge and capability gaps in section 2.1, the following research aims will be addressed in this thesis:

1. Design, build and install a system to measure electrical signals in the snowpack from both SP and ERT measurements
2. Relate these measurements to water content and fluxes in the snowpack, and test the system's sensitivity and utility for long term snow hydrology monitoring.
3. Run and evaluate a physically-based snow hydrology model's (FSM2) performance at predicting SWE and basal runoff using long time series of observed driving data at Col de Porte, and investigate the effects of parameter choice on model performance.
4. Couple FSM2 to a model of electrical processes in a thawing snow pack, in order to evaluate the capability of a coupled system to combine model and measured data to monitor snow hydrological variables.
5. Run FSM2 in a distributed framework over the region of the Alps around Col de Porte, and evaluate with the available verification data over several seasons to assess the performance of FSM2 over the region, and the effect of changing model parameters in a distributed framework.

## 2.3 Thesis structure

Following on from the introduction and review of the literature in Chapter 1, and the overview of the knowledge gaps and research aims in this chapter, the rest of the thesis is composed as follows:

Chapter 3 covers the development and installation of the geophysical array at Col de Porte. Previous experiment designs for both ERT and SP measurements are introduced, and the equipment available to use is outlined. Laboratory experiments which were carried to assess and develop the field installation are described, with key results shown. Next, a description of the field site is given, then the final designs of both the ERT and SP measurement arrays are described. Lastly, an overview of the first season performance is given, which leads into the description of design changes carried out for the second season.

Chapter 4 presents the results of the two seasons of field measurements. The prevailing weather and snow conditions for each winter and spring are described, and geophysical data availability is shown. Then the SP results for each season are presented, including data from the reference measurements. Errors and uncertainties in the measurements are quantified, and for each season a diurnal melt period and rain-on-snow event is investigated, linking the measured signals with the meteorological and hydrological conditions.

Chapter 5 presents the snow hydrology modelling work. Firstly, FSM2 is introduced, which includes a description of the model parametrisations of key snow properties. Next, the process, evaluation data requirements and FSM2's performance at Col de Porte is presented. Once FSM2 has been evaluated at Col de Porte, the modelling is extended to a distributed framework across the whole region. This is carried out by running the model with high-resolution simulated weather data from Meteo France, and the performance over the region is evaluated using remotely-sensed snow cover data. Lastly, to assess to potential of using SP measurements as a hydrological sensor, a model is introduced that represents electrical signals in snow generated by water flow. This model is coupled to FSM2 to generate synthetic SP observations, which are compared to measured SP observations. This allows the evaluation of model representations of internal water fluxes.

Chapter 6 provides a synthesis of the findings presented in chapters 3-5 and outlines how the aims set out in Section 2.2 have been met. The limitations of the research are discussed, and these limitations are discussed in an outlook of possible future work to develop the findings further.

# Chapter 3

# Array development and installation

## 3.1 Previous ERT experiment designs

There is no published research outlining ERT experiments in snow. The closest analogue, on which the ERT part of this project is based, is an experiment on permafrost freezing and thawing carried out with a BGS Geotom system by Murton et al. (2016). In that experiment, the Geotom system was used for almost a year to monitor changes to the rock resistivity as rock samples were frozen and thawed in a laboratory to simulate natural permafrost processes. The system was powered from the mains, and was run using pre-programmed regular measurement sequences. The electrodes used were stainless steel rods, which were inserted into holes drilled into the rock samples to give 3-dimensional coverage of each sample.

## 3.2 Previous SP experiment designs

As described in Section 1.5, SP experiments have been carried out in both laboratory and field settings. In lab experiments, Kulessa et al. (2012) used home-made Petiau type (Petiau, 2000) lead-lead chloride electrodes, mounted on a tube containing snow. The tube was filled with snow and the SP was measured across the two ends of the column of snow. It was found that electrical contact with these electrodes was good when snow was pressed into the tube. Differential voltages were measured using a Campbell Scientific datalogger with the capability to make differential voltage measurements. For field surveying, Thompson et al. (2016) used the potential amplitude manual survey method set out by Corry et al. (1983). The SP was measured between a fixed reference electrode and a roving electrode with which measurements were taken across the area of interest. They pressed the Petiau electrodes into the snow to ensure good contact in a regular grid while surveying supraglacial snow in Switzerland. In this manual survey context, it was found that electrical contact was good. Here a high impedance voltmeter was used to measure the SP between the reference electrode and the roving electrode.

## 3.3 Equipment available

Due to the high cost of geophysical equipment, it was intended to make as much use as possible of existing equipment held at the participating institutions (University of Edinburgh, Swansea University and British Geological Survey). Consideration was also made of the possibility to use equipment held by the NERC Geophysical Equipment Facility but this option was not needed. For ERT measurements, a Geotom system held by BGS was available to be used. This system had been used in previous experiments for longer-term monitoring and it was possible to control the system remotely over an internet connection. For SP measurements, a Campbell Scientific CR1000 datalogger belonging to Swansea University was available, along with six Petiau lead-lead-chloride electrodes.

## 3.4 Laboratory testing

To test the ERT and SP set-ups, including the control software, logger programs and electrodes, some small experiments were carried out in the University of Edinburgh School of Engineering Cold Laboratory.

Previous work by Barraclough (2014) developed a method for producing artificial snow. This method was used to create boxes of artificial snow into which electrodes were placed. The method used to create the artificial snow (outlined in appendixes of Barraclough (2014)) resulted in very cold snow which was around minus 40$^\circ$ C. Density was approximately 400 kg m$^{-3}$, with tightly packed roughly spherical grains of approximately 0.5 mm diameter. These properties meant that the artificial snow was not very realistic when compared to real seasonal snow, but it was a useful test medium as it was a porous material composed of ice crystals, which melted when left at room temperature.

In addition to these artificial snow experiments, a small amount of real snow (collected from the car park the previous winter) was available at British Geological Survey to test the ERT system. This snow was less dense than the artificial snow (not enough was available to measure density properly but it was estimated to be around 200 - 300 kg m$^{-3}$), and was at around minus 18$^\circ$C when removed from the freezer. It was mainly composed of rounded grains of approximately 1 - 1.5 mm diameter, with some larger hoar crystals in it.

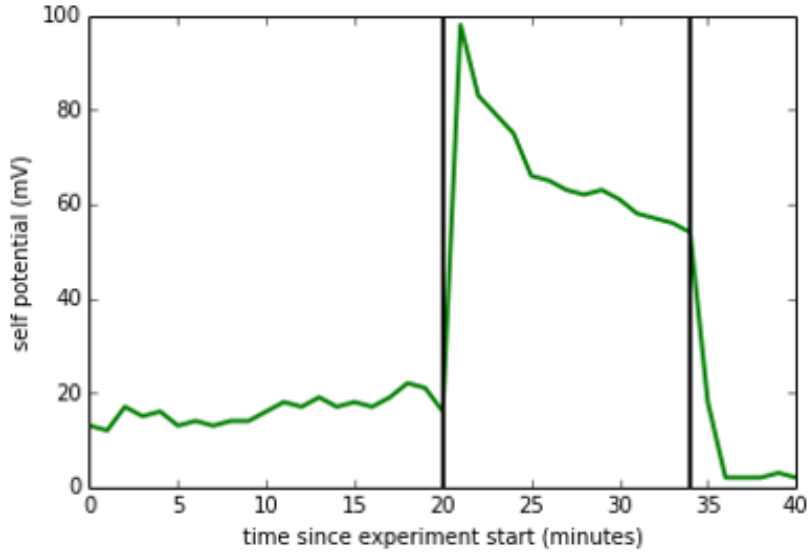


**Figure 3.1:** Measured SP using Petiau electrodes in artificial snow. Black vertical lines indicate injections of 'meltwater'. The second injection causes the breakdown of the snow structure.

## 3.5 Key laboratory results

Both the Petiau and lead strip electrodes were tested for suitability in melting snow. Both types provided stable readings both in thawing artificial snow, and in a water bath, for several days. This corroborates work by Kulessa (2003) showing similar results using lead electrodes. Responses of both types of electrodes to simulated pulses of meltwater were tested. Meltwater pulses were simulated by pouring water onto the snow surface using a watering can. It was found that initially there was a clear response to the pulses of meltwater (see Figure 3.1), but the granular structure of the snow broke down and the response reduced. The structure seemed to break down due to the very cold snow grains causing the injected water to freeze into impermeable ice layers, which then transitioned quickly to completely saturated slush. Once this breakdown in structure occurred the artificial snow was no longer behaving like real thawing snow and the signals were difficult to interpret. These problems with the artificial snow were incidental to this work as it was possible to test the electrodes sufficiently using it.

Similar tests were carried out using artificial snow and the ERT system (see Figure 3.2). Steel nails were used as rod electrodes. These experiments confirmed that dry cold snow has a higher resistivity than wet snow, although again the structure of the artificial snow broke down once water had been poured on it.

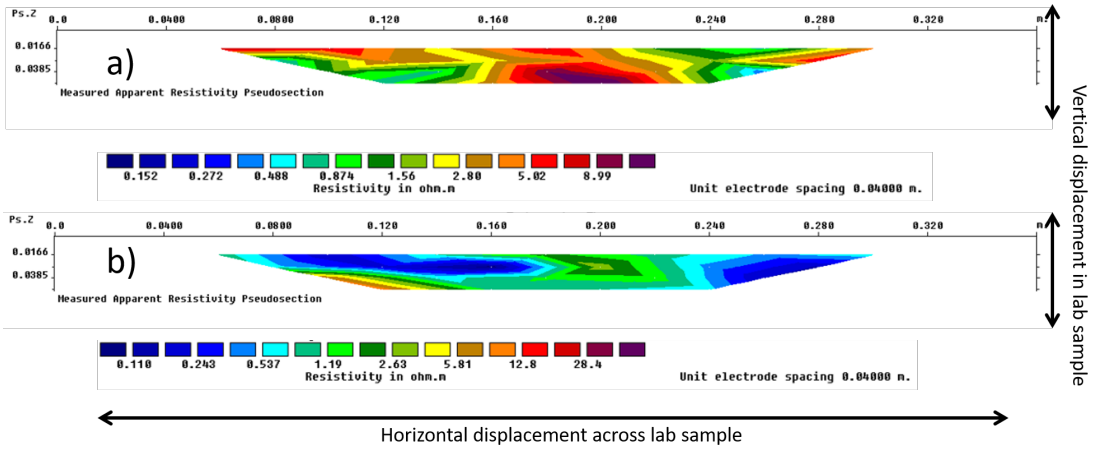


**Figure 3.2:** Artificial snow and ERT: a) Apparent resistivity in dry cold artificial snow. b) Apparent resistivity in wet thawing artificial snow

At British Geological Survey, an experiment was performed using the ERT system with steel rod electrodes in a box of thawing real snow. This snow was left to melt at room temperature and the resistance between the electrodes was measured. It was found that resistance decreased steadily as the snow became wet and isothermal at 0°C; however the structure of the snow broke down and the contact between the electrodes and snow became poor (see Figure 3.3). This experiment showed the utility of the ERT system with steel rods and confirmed that wetting snow reduces the electrical resistance.

## 3.6 Col de Porte field site

The experiments were carried out over a winter season at the snow research station at Col de Porte (45.30° N, 5.77° E), in the Chartreuse Alps in southeastern France. Col de Porte observatory is part of the Centre for Snow Studies (Centre d'Etude de la Neige) run by Meteo France and has a long history of meteorological and hydrological observation for the study of seasonal snow processes. The site opened in 1959 and has daily measurements of snow depth, air temperature and precipitation since 1960. Hourly automatic measurements commenced in 1987. Measured data undergo thorough automatic and manual quality control procedures. A detailed description of the meteorological datasets and associated quality control processes is provided in Lejeune et al. (2019).

The site is a mid-elevation meadow site located at around 1325 m altitude, and is surrounded by mixed forest. There is some limited development nearby, with an adjacent road, hotel and small ski area with associated lift infrastructure. Col de Porte has stable power and wired and wireless internet connections which, along with its proximity to the city of Grenoble, make it a convenient site to locate a geophysical array.

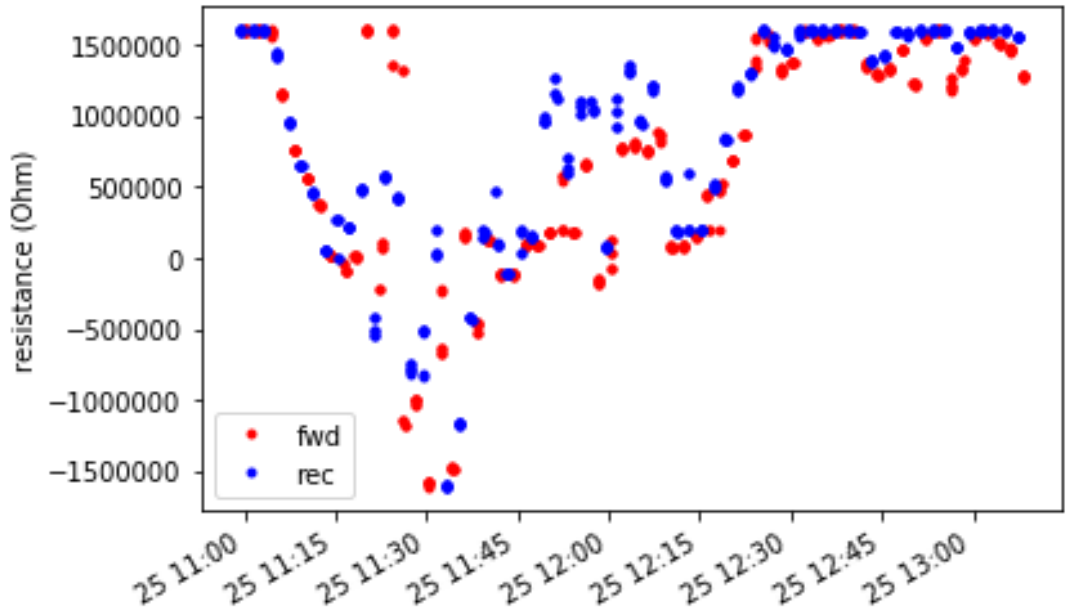


**Figure 3.3:** Measured resistance using steel rod electrodes in thawing real snow sample, showing forward (fwd) and reciprocal (rec) measurements. Forward measurements use one pair of electrodes to inject current and another pair to measure the potential, and reciprocal measurements reverse these electrodes. This is done to evaluate uncertainty in the measurements. A steady decrease in resistance is observed in the first 15 minutes of the experiment, before the snow structure broke down and electrode contact became poor. At this point some erroneous negative resistances were measured.

**Table 3.1:** Automatic hourly meteorological and hydrological data available at Col de Porte. The air temperature and RH measurements are made from a height-adjustable mounting which is changed after each snowfall.

| Variable | Units |
|---|---|
| Snowfall rate | kg $m^{-2}$ $s^{-1}$ |
| Rainfall rate | kg $m^{-2}$ $s^{-1}$ |
| Air temperature (1.5 m above snow surface) | K |
| Relative humidity (1.5 m above snow surface) | % |
| Wind speed (10m) | m $s^{-1}$ |
| Snow melt runoff | kg $m^{-2}$ $s^{-1}$ |
| Snow depth | cm |
| Snow water equivalent | kg $m^{-2}$ |
| Snow surface temperature | K |
| Downwelling long wave radiation | W $m^{-2}$ |
| Downwelling short wave radiation | W $m^{-2}$ |

The site is fairly sheltered from strong winds by trees and local topography. Snow cover is typically observed from early December until mid-April. Snow depths typically reach a maximum of between 0.75-1.5m, but due to the relatively low elevation, positive temperatures and even rainfall are possible throughout the winter. This makes the site ideal for the study of liquid water processes in snow, with the possibility of several melt cycles and rain-on-snow events each winter. Table 3.1 shows meteorological data available at Col de Porte relevant for this study. In addition to the automatic data in Table 3.1, manual snow pit measurements are made approximately weekly through the snow season following standard snow hydrology protocols (Fierz et al., 2009) which provide snow density, grain size, hardness and temperature profiles, and bulk values of SWE.

## 3.7 Array design and installation

An area for conducting the experiment was set aside at Col de Porte which was close to the entrance to an access tunnel beneath part of the site (Figure 3.4). This meant that cables could be routed indoors to the array, and the logger and power supply was available close by. This meant that fewer cables needed to be routed across the site than if the logger was located inside the building. It also meant that some monitoring of meltwater from snowmelt lysimeters was possible as these drained into the tunnel.

The geophysical array was designed to be an ‘inverse borehole’ with electrodes arranged on poles that would be gradually buried by the snow through the winter. The array was composed of 4 poles, each with 10 SP electrodes and 10 ERT electrodes equally spaced up each pole (Figure 3.5). This made 40 electrodes of each type - 80 in total. The poles were constructed from 2 m long 32 mm diameter hollow poles made from white polyvinylidene fluoride (PVDF)

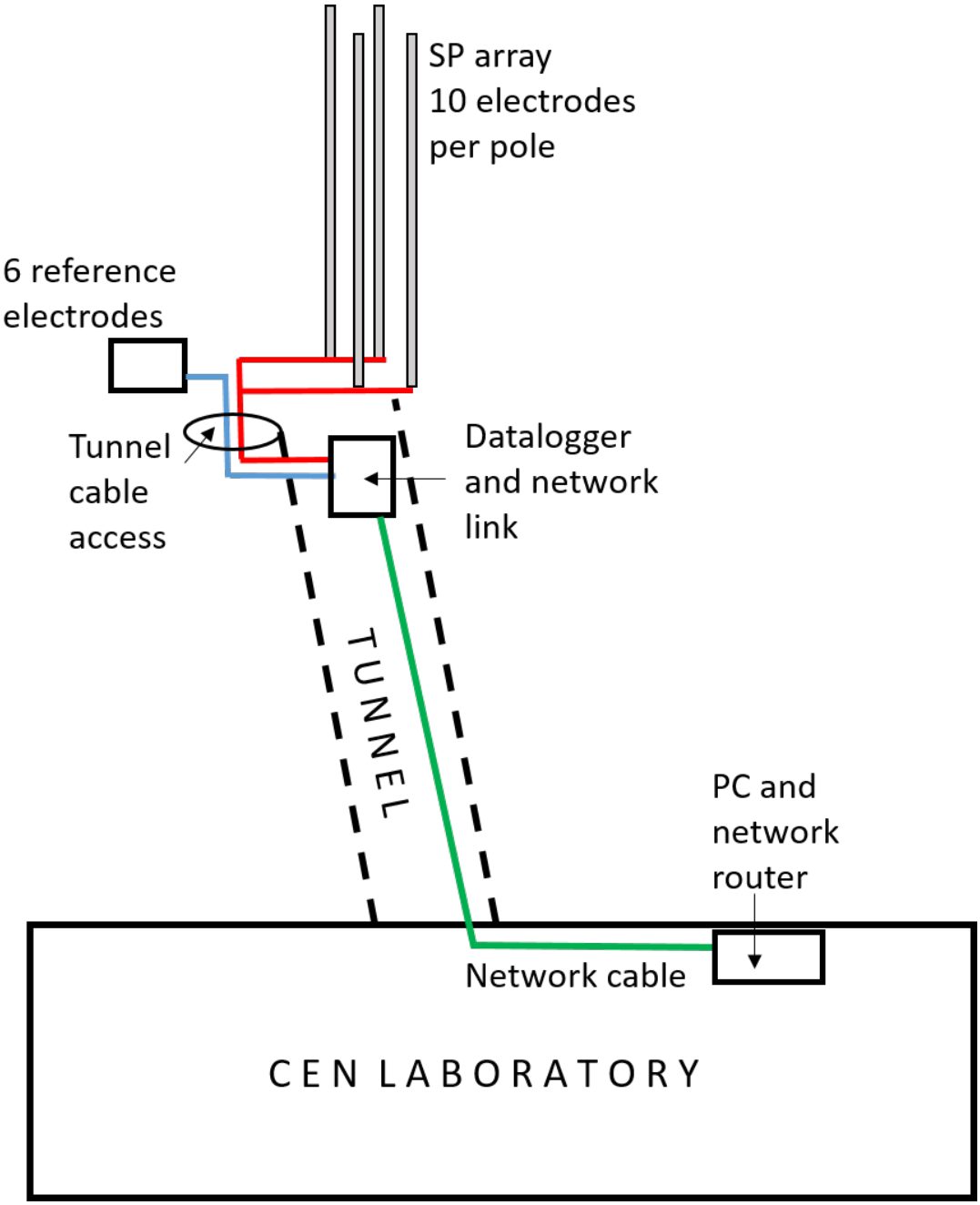


**Figure 3.4:** Layout of SP system relative to laboratory building showing cabling through tunnel

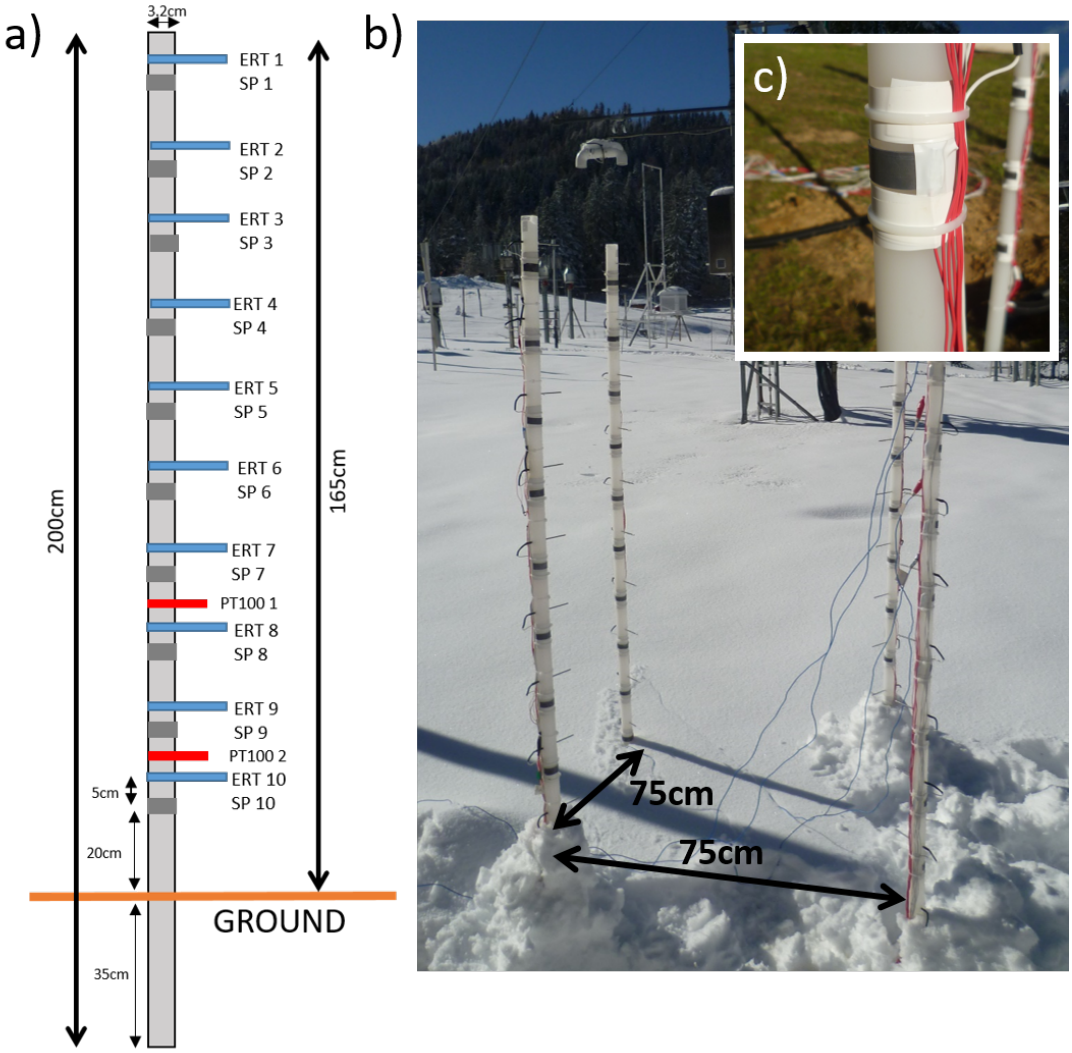


**Figure 3.5:** a) Schematic of a pole showing SP and ERT electrode spacing, and location of PT100 thermistors (only mounted on one pole). b) Photograph of poles during installation in October 2018, with an early snowfall. Pole spacing is marked. Snow around the poles was disturbed during installation but was expected to thaw before lasting snow fell later in the autumn. c) Close up view of lead strip self-potential electrode.

plastic. White plastic was chosen to reduce absorption of solar radiation as much as possible. The poles were arranged in a square with spacing of 75 cm (see Figure 3.5). The spacing and size of the array was partly constrained by the size of the area available for installation, and partly due to the poles also having electrical resistivity electrodes attached to them. The literature and experience from BGS suggest that the horizontal separation of boreholes should be no more than half of the depth of the boreholes, so with snow expected to be up to 1.5 m deep, a pole spacing of 75 cm was used.

The SP array was designed to replicate the potential amplitude manual survey method set out by Corry et al. (1983) and adapted to and used on glacial snowpacks (Thompson et al., 2016). This method employs a fixed reference electrode buried near to, but outside of, the main survey area, and then a roving electrode which is used to measure the SP over a regular grid. Since this was a monitoring study, instead of having a roving electrode, multiplexer chips were used to switch measurements between a regular array of electrodes on the poles.

The ERT array was designed to replicate borehole ERT surveys, with electrodes positioned vertically up the four poles, located in between the SP electrodes. By having electrodes spread on four poles in a square it was hoped that differences in readings between poles could be related to lateral differences in meltwater percolation in the snowpack. Similarly, the differences between readings from electrodes at different heights were intended to be related to the motion of meltwater on its journey from surface melt or rainwater input to basal runoff.

### 3.7.1 SP system design

#### Data logger, multiplexer switching and network equipment

A Campbell Scientific CR1000 data logger was used to make SP measurements. It was mounted in a waterproof instrument enclosure inside the tunnel beneath the site, adjacent to a power supply. Alongside the logger, a network connection was provided by a Campbell Scientific NI201 network interface, wired into the local internet router. This enabled the logger to be programmed, and data to be retrieved, remotely from Edinburgh. The voltage measurements were switched between electrodes using unbranded 16-channel multiplexer chips. These were built onto electrical prototyping boards with screw terminals attached by the staff at the NERC Geophysical Equipment Facility. The screw terminals meant it was simple to attach the electrode cables to the multiplexers.

### Reference electrodes

The reference electrodes were non-polarising lead/lead-chloride self-potential electrodes of the Petiau type (Petiau, 2000) buried next to the main array approximately 10 cm deep in the soil, which was considered to be sufficiently deep, as thermal effects from diurnal heating were not a concern when the ground was covered in snow. Petiau electrodes were used for the reference electrodes because they produce stable readings over longer periods. They have a porous end which needs to remain damp to maintain good electrical contact, and because they were buried in the soil this condition was met over the winter period.

### Pole electrodes

Petiau-type electrodes are too big to mount on poles. Manufacturing smaller bespoke Petiau-style electrodes was considered, as in Kulessa et al. (2012), but they also need to be kept damp to maintain electrical contact. This would not be possible for extended periods of time above the snow as the snowpack builds up before burial. Therefore, the electrodes for the poles were manufactured from lead sheeting and mounted on the poles. Kulessa et al. (2003) used solid lead electrodes for monitoring experiments over a whole year. This corroborated their water bath testing and general expectations that lead is inert and non-polarisable. The lead strip electrodes employed here gave stable self-potential readings in water baths for several days. A lead electrode is shown in Figure 3.5c. They were constructed as strips of lead wrapped around the pole to provide a large surface area for contact with the snow, whilst remaining flush with the pole to reduce the possibility of snow compaction ripping them off.

### Wiring arrangement

The electrodes were wired up to form 43 pairs of electrodes between which differential voltage measurements were made. These consisted of 3 reference pairs between 6 reference electrodes, and then 40 dipoles between a reference electrode and a pole electrode. Three pairs of reference electrodes were required because three multiplexer chips were used. The measurements were made using a Campbell Scientific CR1000 datalogger, with multiplexer chips used to switch between the pole electrodes (Figure 3.6).

### Data collection and processing

Self-potential voltages were measured every 5 seconds between all 43 pairs of electrodes. The PT100 temperatures were measured once per minute. SP was measured at each electrode giving 40 SP values. Data measured at 5 second intervals showed diurnal and shorter-term variability overprinted on longer-term self-potential changes. To remove this shorter-term high-frequency variability and longer-term changes, the data were detrended, and then averaged at a 30 minute interval. This preserved the diurnal fluctuations in the signal that we could relate to meteorological and hydrological data available to us.

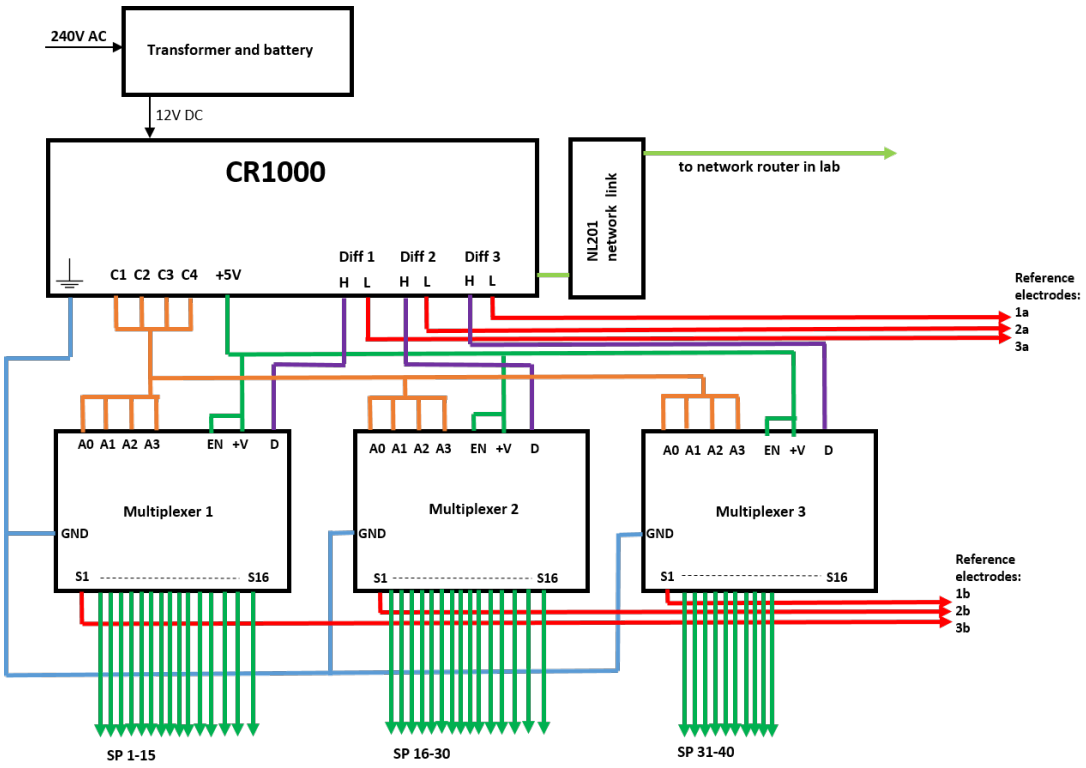


**Figure 3.6:** Wiring layout showing configuration of logger, power supply and multiplexers.

### 3.7.2 ERT system design

#### ERT electrodes

After laboratory testing and following on from BGS experience using them for permafrost experiments (Murton et al., 2016), it was decided to use steel rods as ERT electrodes. This was due to their ease of manufacture and high grade steel's good conductance. These were constructed from 80 mm lengths of high-grade steel at BGS. They were mounted ten per pole, pointing into the middle of the square formed by the four poles. Holes were drilled in the poles, and the electrodes were pushed through so they protruded 50 mm from the poles. The cables were fed down the outside edge of the poles, and then on to the control unit inside the building through the tunnel. White wire casing was chosen to minimise absorption of solar radiation.

#### Wiring arrangement and power supply

Upon entering the tunnel, the ERT cables were fed into a junction box where the individual cables (one per electrode) were attached to two 25 core printer cables. This was to minimise the number of single cables running along the tunnel and to the control unit inside the building (see Figures 3.7 and 3.8).

The control unit ran on an internal 12 V battery, which needed to be charged regularly. A charger was plugged into the mains and controlled with a timer switch. It was important not to charge the internal battery at the same time as making measurements as this could have interfered with the measured potentials.

#### ERT control system

The ERT measurements were controlled by the Geotom system's internal microcomputer, which was connected to a laptop which was running the manufacturer-supplied control software for the system. Because the laptop was connected to the internet and had remote access enabled, this meant that the ERT system could be controlled from Edinburgh.

### 3.7.3 Temperature sensors

In addition to the ERT and SP electrodes on the poles, on one of the poles, two PT100 thermistors were mounted at 30 and 60 cm above ground (see Figure 3.5). The aim of these sensors was to be able to verify when the snow was isothermal at 0°C and hence able to support liquid water flow. It was also useful to be able to verify how much of the pole was exposed in the air: when covered in snow the temperature was at or a few degrees below freezing, but when exposed to the air the temperature was above 10°C in direct sunshine and as low as minus 10°C overnight with clear skies.

### 3.7.4 Installation for winter 2018-19

Final preparations were made at BGS before the equipment was shipped to France. The array was constructed on-site at Col de Porte, with wiring and cable routing finalised as the systems were installed. Installation was carried out in autumn 2018 in mostly snow-free conditions, although some short-lived snow did fall at times.

## 3.8 Companion meteorological and hydrological data

In addition to the automatic data in Table 3.1, manual snow pit measurements are made by Meteo France staff approximately weekly through the snow season following standard snow hydrology protocols (Fierz et al., 2009). These data provide snow density, grain size, hardness and temperature profiles. In addition to the routine measurements made by Meteo France staff, daily manual snow pit measurements were made for one week in March 2019, and dye tracing experiments were carried out to assess qualitatively meltwater percolation (Campbell et al., 2006; Kinar and Pomeroy, 2015). Rhodamine B dye in powder form was mixed with water, then poured evenly onto a marked 1 m square using a gardening watering can with a

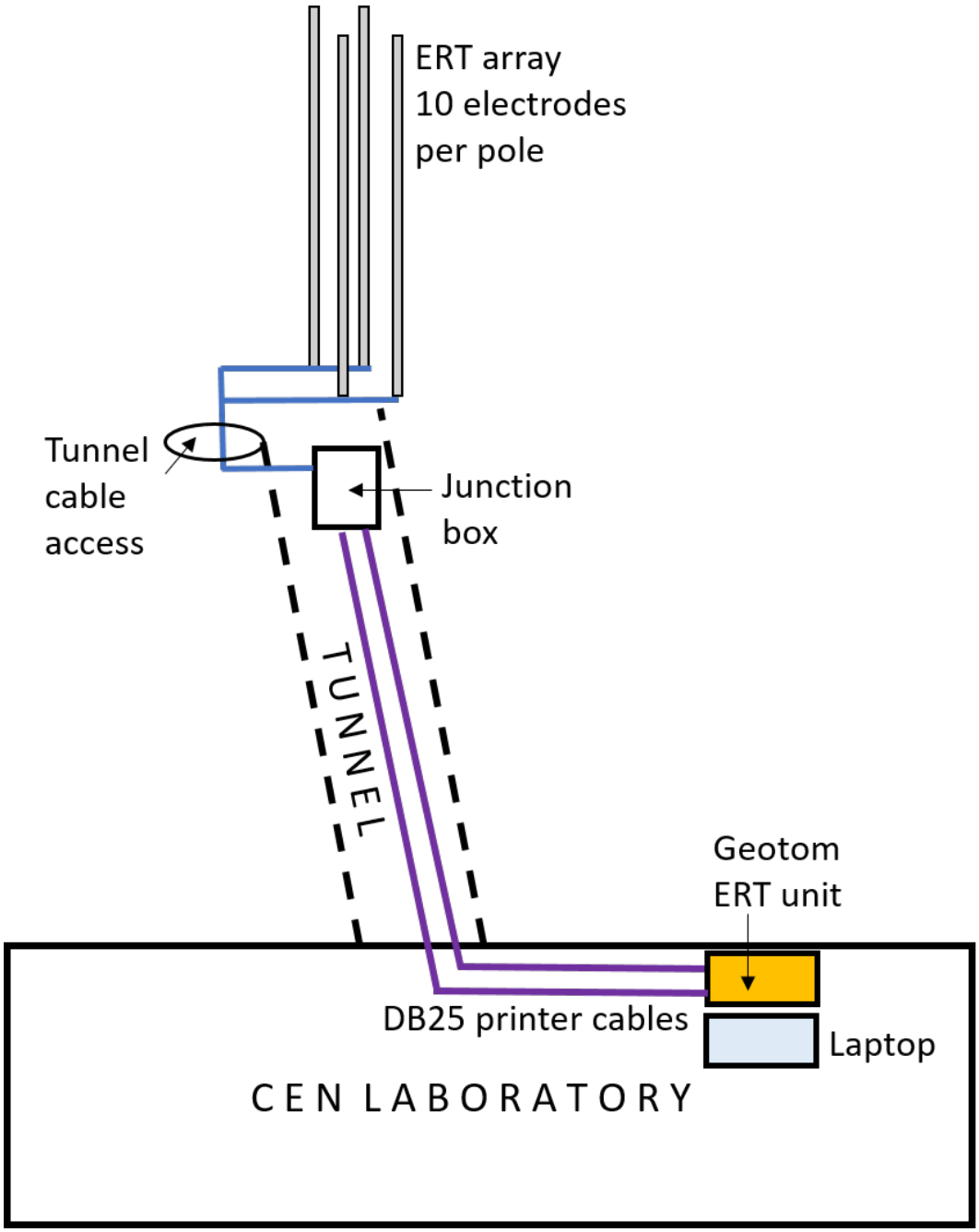


**Figure 3.7:** Layout of ERT system relative to laboratory building showing cabling through tunnel and location of Geotom control system

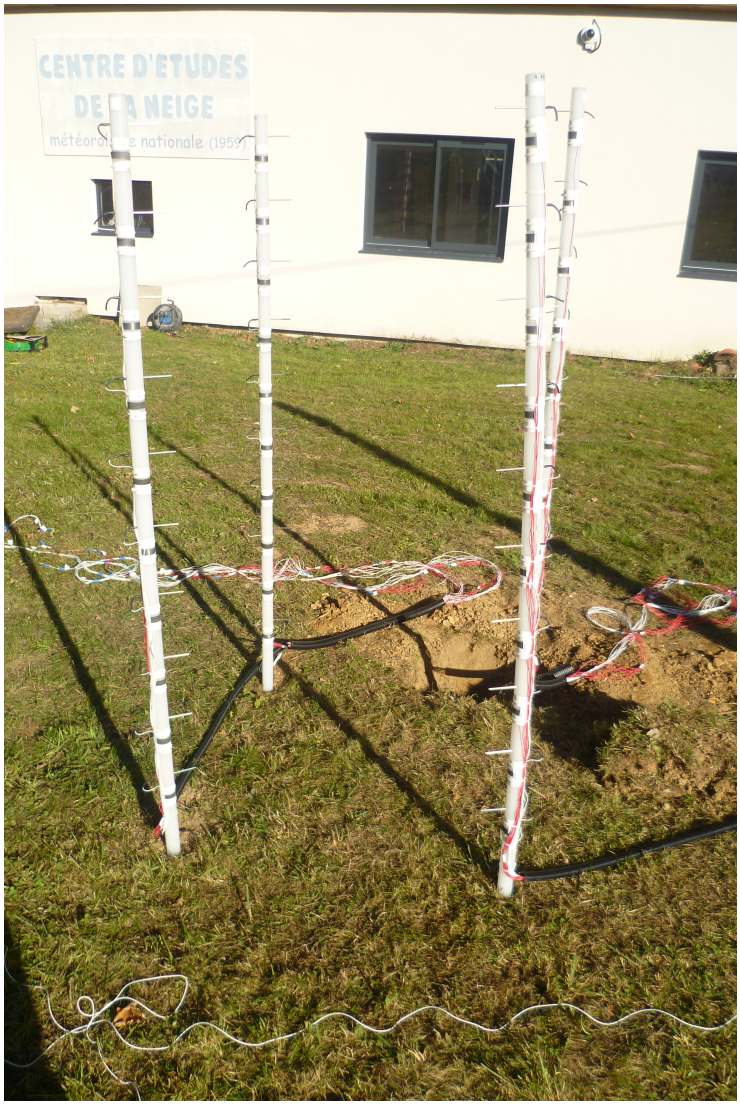


**Figure 3.8:** Installation of system in snow-free conditions in October 2018, showing location of tunnel access behind poles, and adjacent laboratory building.

sprinkler attachment. The snowpack within this area was then excavated to the ground after three hours allowing the dye percolation to be observed in the snow pit wall. Daily webcam images provided by Meteo France were available to help monitor the system state and snow cover.

To aid the SP modelling, measurements of meltwater electrical conductivity (EC) and pH were made using the runoff from an old lysimeter outlet which ran into the tunnel next to the logger systems. Unfortunately, continuous monitoring of the EC and pH was not possible with the equipment available, but daily readings were made during the week of manual measurements in March 2019.

## 3.9 First season performance

### 3.9.1 SP

The SP system performed fairly well during the first season (winter 2018-2019). There were some issues with the connections to the reference electrodes at first but these were rectified before the main melt events in March and April. There were some gaps in the data due to power outages but the system worked without gaps through the main melt periods in March and April 2019 (Figure 4.2). The remote control of the logger and retrieval of data over the internet worked well.

### 3.9.2 ERT

The ERT system performed poorly throughout the season. It was not clear why, but it was thought to be due to a combination of battery charging problems and the connection between the laptop and Geotom control unit timing out. When this happened it required a hard reset which was not possible remotely. The system was rebooted and did operate briefly during a field visit in March 2019, but the data were very poor, with extremely poor electrical contact which seemed to trip the system midway through its measurement sequence. It appeared that the remote control problems had been fixed after the visit in March 2019, but upon returning to Edinburgh it was not possible to connect to the machine. Despite manual resets being carried out by Meteo France staff at Col de Porte the system would not operate. This meant that after the first season there was no usable ERT data.

**Figure 3.9:** Close-up photograph of mesh ERT electrode during installation in November 2019

## 3.10 Improved design for winter 2019-20

After the successful operation of the SP system in the first season, it was left as it was. Clearly though, the ERT system needed to be adjusted significantly to improve the chances of getting some data.

The power and charging set up was modified significantly. Staff at BGS installed a timer switch which rebooted the device completely after each measurement sequence was made. This was intended to prevent the system from losing connection to the laptop during or after each measurement. The charging set up was also changed, employing a trickle charger to a large external battery. This larger external battery was then connected into the system to power it. By running the system on an effectively isolated power source, it was hoped that any power issues caused by mains power affecting the potential measurements would be removed.

To improve the electrical contact between the electrodes and the snow, the electrodes were completely redesigned. Instead of stainless steel rods, high-grade steel mesh shaped into a half-cylinder shape was used (see Figure 3.9). These mesh electrodes were designed to maximise the surface area of metal that would be in contact with the snow.

In addition to the improved electrodes on the poles, a line of ground electrodes was also installed. The electrodes were 200 mm long, 10 mm diameter steel rods soldered onto lengths of instrument cable. The intention of these was to use the ERT system in a more traditional (and hopefully reliable) way, with good electrical contact. It was intended that the ground measurements would be able to detect when snow melt started to percolate into the soil. This ground line was installed adjacent to the pole array.

As well as the ground ERT measurements, two ECHO EC-5 dielectric soil moisture sensors were purchased and installed next to the array, buried approximately 10 cm below the surface. These were wired into the tunnel and into the CR1000 datalogger.

## 3.11 Second season performance

Unfortunately the second season (2019-2020) was a very low-snow year, so most of the electrodes remained above the snow surface throughout. In addition to this, in March 2020 the COVID-19 pandemic began, which meant that a planned field trip in that month had to be cancelled.

In the second season, the SP system performed well again, although readings were only available from the lowest electrodes due to the shallow snow cover. The EC-5 soil moisture sensors also performed well.

Unfortunately the ERT system's performance was poor for a second year. The pole electrodes were exposed for much of the season, so the mesh electrode design was never really tested. The system's power supply and rebooting issues persisted despite the attempted fixes. It would still have been possible to test the system manually in March 2020 when visiting, but this visit was cancelled due to COVID-19 and the Meteo France staff were only able to complete essential work according to operational priority. Due to the power issues, the ground electrodes were unable to make any measurements remotely, and manual measurements were not possible.

# Chapter 4

# Field results

## 4.1 Introduction

This chapter presents field measurements carried out in the 2018-19 and 2019-20 winters, including self potential, meteorological and hydrological data.

## 4.2 Prevailing meteorological conditions

### 4.2.1 Winter 2018-2019

In autumn 2018 there were some short-lived shallow snowfalls in October and November, then lasting snow fell in December. It was not of sufficient depth to cover the array until further snowfall during January and early February. Snow depth reached a maximum of around 165 cm during early February, which completely buried the poles. It then compacted and thawed through the rest of February with the exception of two small snowfalls. Some snowfall in the first half of March was followed by a prolonged period of melt. There was another snowfall in early April of around 40 cm which reburied the lower electrodes meaning SP measurements were possible for a longer proportion of the melt season (see Figure 4.1).

### 4.2.2 Winter 2019-2020

Winter 2019-2020 was less snowy than the previous year. There was a snowfall of about 30 cm in mid-November, which thawed before lasting snow arrived in December. Depth reached around 70 cm in mid-December but thawed to around 30 cm before the end of the month. Through January and February snow depth remained between 40-50 cm, before the last snowfall of the season increased the depth to around 70 cm. This then thawed through the rest of March, with the snow thawing completely in the first few days of April. This relatively low-snow winter meant that for much of the season very few electrodes on the array were buried. Figure 4.1 shows how the two seasons compare in the spring which is the main period for melting. It is clear from this figure that spring 2020 was one of the least snowy in the last few decades.

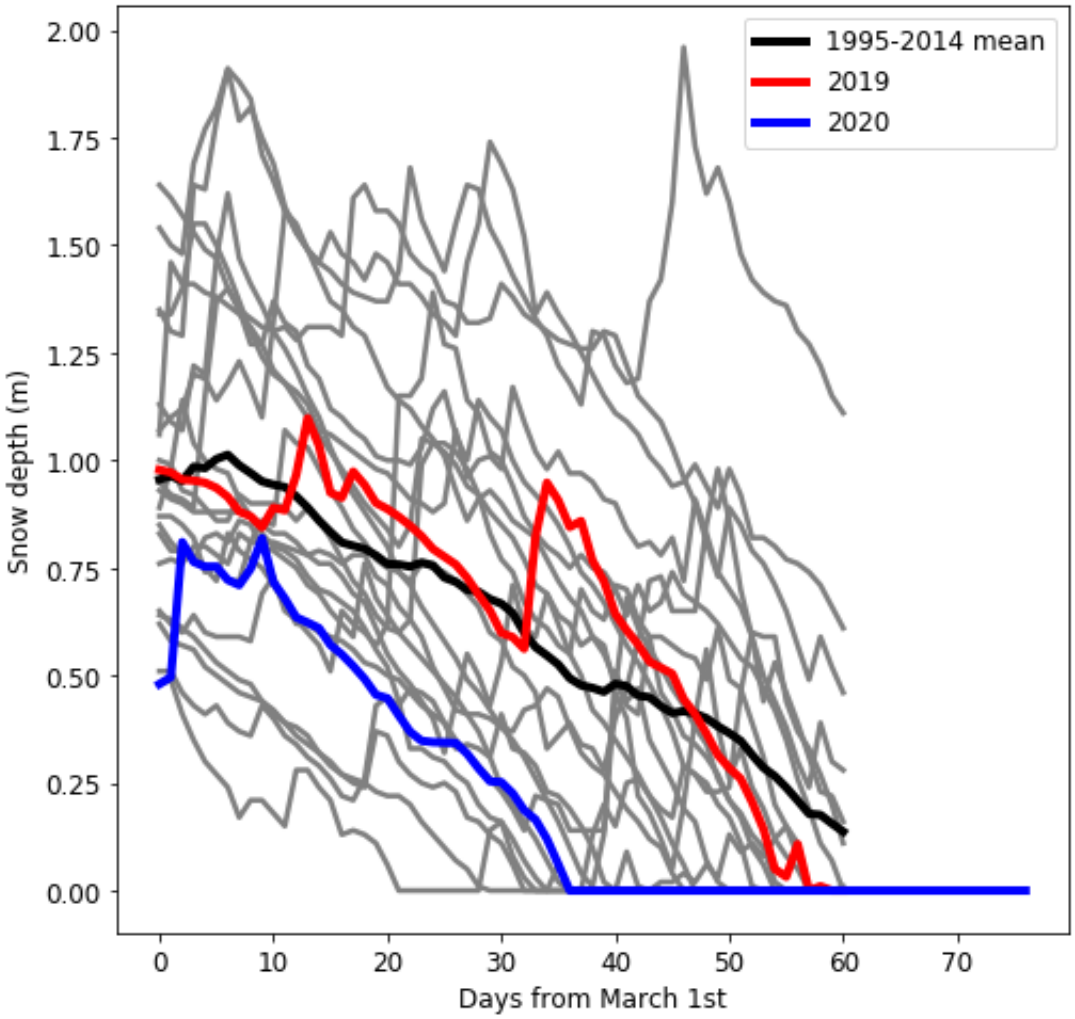


**Figure 4.1:** March and April 2019 and 2020 snow depth at Col de Porte plotted alongside 1995-2014 and long-term mean. Grey lines show individual years.

**Table 4.1:** Data availability at Col de Porte from 2018-2020.

| Month | Notes | SP | ERT | Manual data | PT100 | EC-5 |
|---|---|---|---|---|---|---|
| Oct 18 | Installation | | | | | |
| Nov 18 | | | | | | |
| Dec 18 | Lasting snow | | | | | |
| Jan 19 | | | | | | |
| Feb 19 | | | | | | |
| Mar 19 | | | | | | |
| Apr 19 | | | | | | |
| May 19 | Melt out | | | | | |
| | | | | | | |
| Oct 19 | | | | | | |
| Nov 19 | Installation | | | | | |
| Dec 19 | Lasting snow | | | | | |
| Jan 20 | | | | | | |
| Feb 20 | | | | | | |
| Mar 20 | COVID-19 | | | | | |
| Apr 20 | Melt out | | | | | |
| May 20 | | | | | | |
| | | | | | | |
| | **Key** | No data | Limited data | Good data | | |

## 4.3 Data availability

The availability of data from the field measurements is shown in Figure 4.1. The most useful data were from spring 2019, with a deep snowpack which was subjected to a lengthy spell of clear diurnal melting. There was also a rain-on-snow event in April 2019.

## 4.4 2018-2019 season results

### 4.4.1 Reference electrode data

One of the reference electrodes (reference 3) was subject to some problems, probably caused by wiring coming loose at the logger or multiplexer. This affected the readings until March 2019 when a site visit was possible to rewire the electrode. Measurements thereafter appeared to stabilise. Table 4.2 shows the reference electrode uncertainties during the main melt season after the wiring was fixed (late March and April 2019). Figure 4.2 shows the whole season's reference data, clearly showing the gaps early in the season and the issues with reference 3 from January to March where the variation was much larger and the baseline reading was a long way off 0 mV.

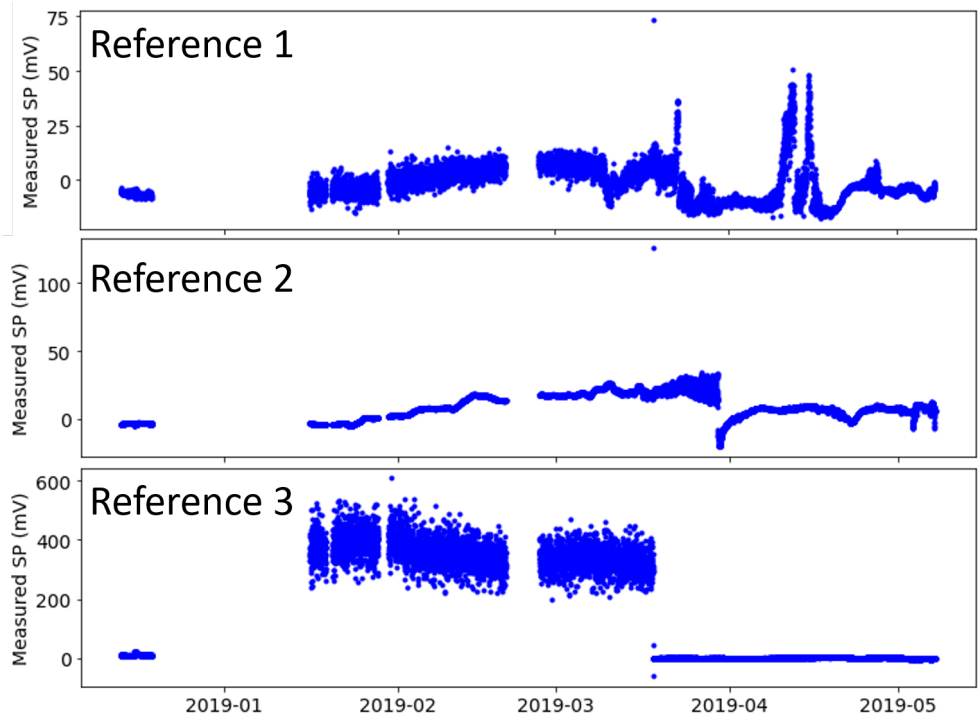


**Figure 4.2:** Full season reference electrode data.

### 4.4.2 Uncertainty and error quantification

#### Reference measurements, dry snow and free air measurements

After the wiring had been fixed (see section 4.4.1) reference measurements were generally stable, although some high frequency variations were present in the raw data. The reference readings had no notable diurnal (or other period) cycles apparent. Table 4.2 shows the mean and standard deviation of the reference electrode measurements. Reference 1 showed more variation than 2 and 3 with a standard deviation of 29.9 mV versus 10.8 mV and 4.8 mV respectively. Once the reference readings had been smoothed in the same way as the pole readings, the variation was negligible compared to the magnitude of the signals associated with meteorological and hydrological factors seen in the pole readings. Figure 4.8 shows the SP signals associated with electrodes melting out and being exposed above the snow surface. Once the electrodes are exposed a diurnal cycle is not visible.

Figure 4.3 shows the difference between SP signals measured within the snowpack and above the snow exposed in air. It is clear that the measurements in air are noisier due to their much larger error magnitude compared to the measurements in snow, and they do not exhibit cycles such as the clear diurnal cycle visible in the buried SP measurements. The standard error of the mean of the measurements in the snow is much smaller than the measurements in the air.

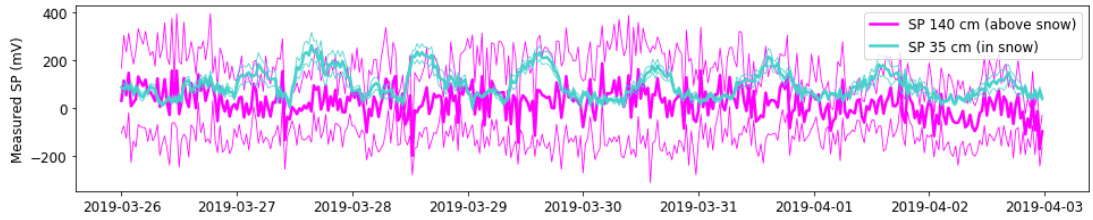


**Figure 4.3:** Example period from late March to early April 2019 showing difference between SP measurements in the snowpack and exposed in air above the snow. Standard error of the mean plotted in thin line style. Note the difference in error magnitude for electrodes buried vs. electrodes above the snow. Above snow mean error for this period is 146.2 mV compared with 20.6 mV when buried in snow.

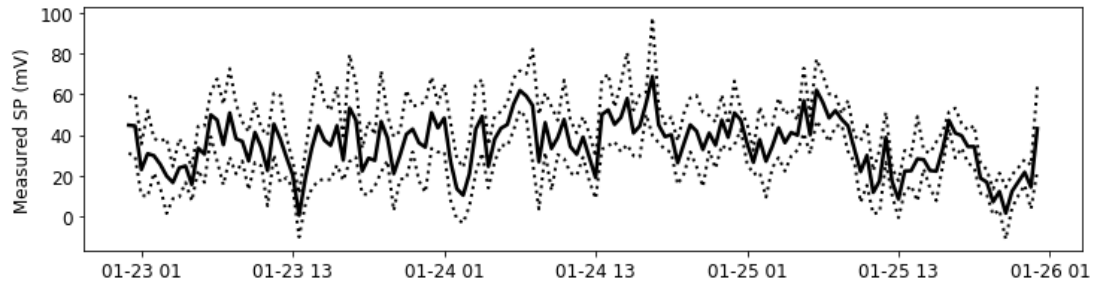


**Figure 4.4:** Example period from late January 2019 showing the signal from electrodes buried in dry cold snow, with standard error of the mean plotted with dotted line. Mean error over this period in dry snow was 13.2 mV.

**Table 4.2:** Mean reference voltage and standard deviation for 21 March - 14 April 2019

| Electrode pair | Mean differential voltage (mV) | Standard deviation (mV) |
|---|---|---|
| Reference 1 | -4.8 | 29.7 |
| Reference 2 | 10.8 | 10.8 |
| Reference 3 | 0.4 | 4.8 |

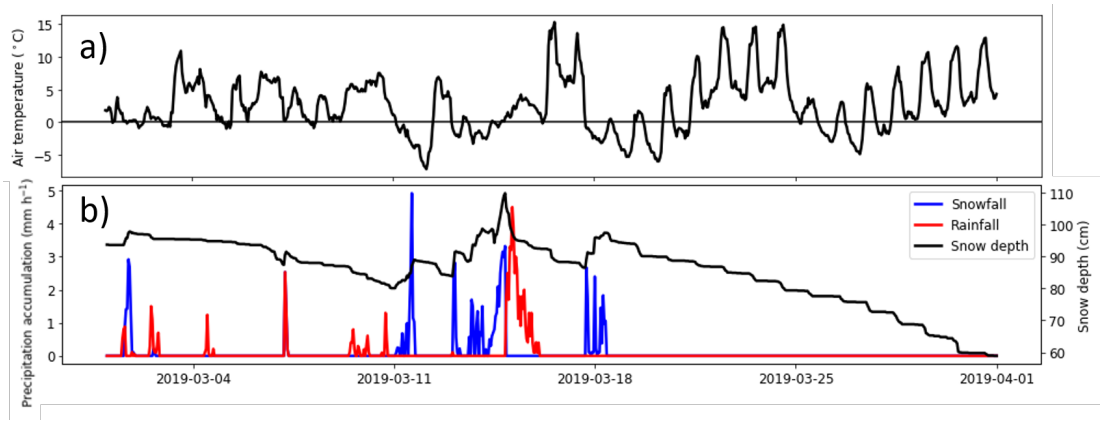


**Figure 4.5:** a) Observed air temperature at Col de Porte for March 2019. b) Observed precipitation and snow depth at Col de Porte.

Figure 4.4 shows measurements from electrodes buried in cold dry snow. There is still an SP signal being generated, but it does not exhibit a diurnal cycle as the snowpack was not experiencing any melting. The magnitude of the SP signal is around 30-50 mV which is lower than the magnitudes of variations observed when a clear meltwater signal was present in late March and mid April.

### Lateral and vertical variation in readings

As described above, it was hoped that lateral and vertical differences would be discernible in the measurements. Unfortunately, it was impossible to discern any coherent lateral differences between the 4 poles. Similarly, coherent vertical differences in timing were not visible in the data from electrodes at different heights within the snow, although it was possible to differentiate between those electrodes that were buried and those that were not (Figure 4.3). Because of this, the analysis that follows concentrates on mean measurements from the four electrodes at each height, and does not consider vertical or lateral changes in the signal.

### 4.4.3 Self-potential signals during diurnal melting in spring

#### Meteorological and snow cover conditions in March 2019

March 2019 gave mixed conditions with some periods of snowfall, some rainfall, but temperatures often above freezing (see Figure 4.5). Snow depth was around average for the time of year compared to previous years (Lejeune et al., 2019; Morin et al., 2012) (see Figure 4.1). During late March, there was a prolonged period of snowmelt following a clear diurnal cycle. This was caused by a period of anticyclonic atmospheric conditions giving warm sunny days with ablation driven by solar radiation, and cool or cold nights with conditions ideal for radiative cooling and overnight refreezing. Air temperatures in the middle of the day reached as high as 15°C, but snow-surface temperatures overnight fell to below minus 10°C on several nights (see Figure 4.6b). This period of marked diurnal melt/freeze cycling persisted into early April. During this period, snow depth was initially around 90 cm, falling to around 60 cm by the end of March. In Figure 4.5, this period of snow melt is clearly seen from around 21st March in the observed snow depth, accompanied with predominantly positive air temperatures. Thawing takes place every day from this date onwards. Figure 4.6b shows the snow-surface temperature reaching 0°C each day, indicating thawing is taking place. Within the snowpack, the temperature remained close to 0°C, which supports the assumption made earlier that thermoelectric potentials will be negligible within the snowpack. As the snow depth reduced, the PT100 sensor mounted 60 cm above the ground became exposed and recorded positive temperatures in the day time when exposed to solar radiation. Whilst thawing is occurring at the snow surface every day during this period, there is a slight lag before runoff starts being recorded in the lysimeters (Figure 4.6d). From around the 24th March onward, a daily peak of runoff is observed, increasing to a peak flow of about 2 kg $m^{-2}$ $h^{-1}$ by the end of March. This shows that the snowpack is able to support liquid water flow through its full depth from around 24th March onwards.

Dye tracing experiments carried out on the 19th and 20th March (Figure 4.7) show that most of the snowpack was able to support meltwater flow. In these qualitative experiments to investigate the meltwater percolation, several layers were visible, and vertical and horizontal flow and preferential flow fingers were observed. It was found that dye reached the lowest layers of the snowpack in 2-3 hours, but instead of continuing to percolate to the base of the snowpack, it then flowed horizontally down a slight gradient along a layer interface, marked in Figure 4.7. This layer interface was at around 15 cm above the ground so was below the lowest SP electrode on the pole but above the reference electrodes. Snow pit observations established that there were no ice layers or lenses at this depth in the snowpack, and that the interface that the dye flowed along marked a relatively small change in density, but with similar

size snow grains. The stratigraphic contrast was also observed in snow pit observations on 28th March, albeit with a smaller density contrast. This was around 5 days after the lysimeters started to record runoff, showing that despite the layer interface persisting, the snowpack could support water flow right to the base.

#### Measured self-potential signals during late March 2019

As discussed above, the snowpack was able to support liquid water flow during late March. Therefore, we expected to be able to measure self-potential signals generated by this fluid flow in the snowpack. Preferential melting had occurred around the poles so the snow depth covering the pole was lower than the measured snow depth elsewhere, by around 5 to 10 cm. With a snow depth of around 90 cm at the beginning of the period, the top 5 SP electrodes on each pole were exposed, and by the end of the period with a depth of 60 cm, only the lowest 3 electrodes were reliably buried by the snow. Therefore, the data from the top 7 electrodes on each pole were neglected. From Figure 3.5, it can be seen that the 3 lowest electrodes on each pole are at heights of 20 cm, 35 cm and 50 cm above the ground.

In Figure 4.6e a diurnal pattern is visible in the signals from the buried self-potential electrodes at the three lowest heights on the poles. Some days exhibit multiple peaks, and especially towards the end of the period, a clear daily signal is visible. The cycle peaks are generally during the afternoon, with the minima overnight. This supports the assumption that the SP peaks are caused by diurnal melt flow. The peaks of each diurnal cycle increase in magnitude from around 24th March, which is when the lysimeter started recording runoff. However, the fact that there is still a diurnal peak before then supports the assumption that early in the period the SP signals are being generated by internal melt flow which is not reaching the base of the snowpack.

### 4.4.4 Self-potential signals during a rain-on-snow (RoS) event

#### Meteorological and snow cover conditions in mid-April 2019

After the period of prolonged melt in late March, heavy snowfall occurred early in April which increased the snow depth to around 110 cm. Further periods of thaw and some further snowfall occurred through to mid-April. Late on the 9th April, there was a small rain-on-snow event, then on the afternoon of the 10th April there was another, larger rain-on-snow event. There was no snowfall during this period. Figure 4.8b shows the air temperature remaining above freezing during and after these rainfall events. Snow surface temperature remained at 0°C until the night of the 12th April, so thawing can be assumed to have been taking place until then, with refreezing taking place that night followed by melting again the following day. Snow depth was initially around 70 cm on the 9th, falling to about 52 cm by the morning of the 13th. The temperature measured at 30 cm above ground remained around 0°C throughout,

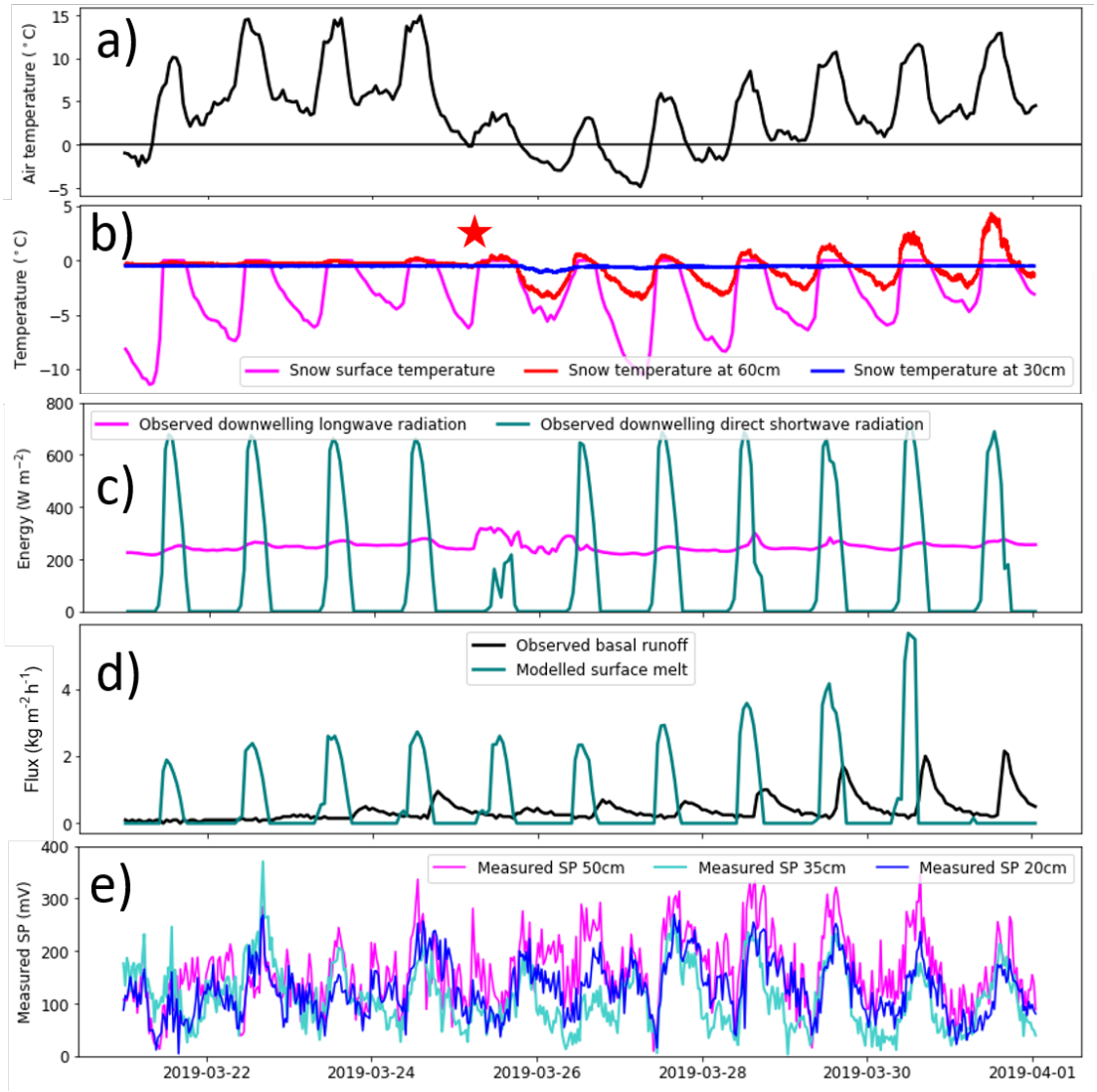


**Figure 4.6:** Meteorological, hydrological, and SP measurements for late March 2019. a) Observed air temperature. b) Observed snow surface temperature, and temperatures measured using PT100 thermistors at 30 cm and 60 cm above ground level for late March 2019. The red star indicates the approximate time from which the 60 cm thermistor was exposed (see cavities in picture in Figure 4.9). c) Observed downward longwave and shortwave radiation. d) Observed basal runoff from Meteo France lysimeter, and modelled FSM surface melt. e) Mean self-potential from the 4 electrodes at each height buried in the snow. The mean standard error of the mean over this period was 39.9 mV at 50 cm, 21.4 mV at 35 cm and 23.5 mV at 20 cm.

**Figure 4.7:** Dye tracing experiment carried out on 20th March 2019. The density contrast, along which horizontal flow occurred, is marked.

indicating that electrodes below that height would be buried. However, the PT100 at 60 cm recorded positive temperatures on each day, so it is assumed that electrodes around this height were not completely buried by the snow. Figure 4.9 shows a snapshot from the Meteo France webcam on 12th April. Cavities around the poles are visible, which explains why the electrodes and upper PT100 were not buried despite the observed snow depth nearby being sufficient earlier in the period.

Figure 4.8e shows the observed rainfall, along with measured basal runoff and modelled surface melt. A clear peak in runoff is visible after each rainfall event. These peaks do not occur during the mid-afternoon as would be the case from diurnal melting. Before the first peak (runoff 1) there is a peak in modelled surface melt which will have supplied some liquid in addition to the rainfall at Rain 1. The second peak (runoff 2) follows rain peak 2, and in this case there is no surface melt input. For runoff peaks 3 and 4, the runoff reverts to a diurnal cycle driven by solar radiation, which can be seen from the shortwave radiation and air and snow temperature peaks, although this is not reproduced by the model. Both the lower PT100 measurements and the Meteo France snow profiles carried out nearby show an isothermal snowpack at 0°C which could therefore support meltwater percolation to its base.

#### Measured self-potential signals during mid April 2019

As discussed above, by mid-April the snow depth was not sufficient to cover many electrodes, with the preferential melting that occurred around the poles reducing the buried electrodes to those at 20 and 35 cm. Unfortunately, the measurements from the lowest level (at 20 cm) had shown evidence of longer-term changes in the self-potential signal by this stage of the season. I was unable to relate these changes to the observational data available. The electrodes at 35 cm appeared to give plausible readings, so the discussion of the rain-on-snow event and its self-potential signatures refer to measurements made at this level. The data from the electrode at 50 cm were left on Figure 4.8 to show the response as it melts out and becomes uncovered.

In Figure 4.8f a small peak (SP 1) in SP is visible on the evening of the 9th which occurred during the first period of rainfall. The associated peak in runoff (Runoff 1) is slightly delayed from the peak in rainfall (Rain 1), reflecting the time required for the water to percolate to the base of the snowpack. On the 10th, two SP peaks are visible. The first (SP 2) is smaller and occurs around noon. This is due to surface melting taking place. The air temperature was above freezing along with a peak in incoming shortwave radiation, and the snow surface was at 0°C. The second much larger peak (SP 3) occurs at the same time as the second rainfall event (Rain 2), which was heavier than the first with hourly accumulation of over 6 kg $m^{-2}$ compared to around 2 kg $m^{-2}$ for rainfall 1. The peak in runoff (Runoff 2) begins to occur before the rainfall, so it was probably registering runoff from surface melt first, and then percolation of rainwater. A further small peak (SP 4) is registered in the SP signal during the evening of the 11th, and it is not clear why this did not occur earlier when more melting

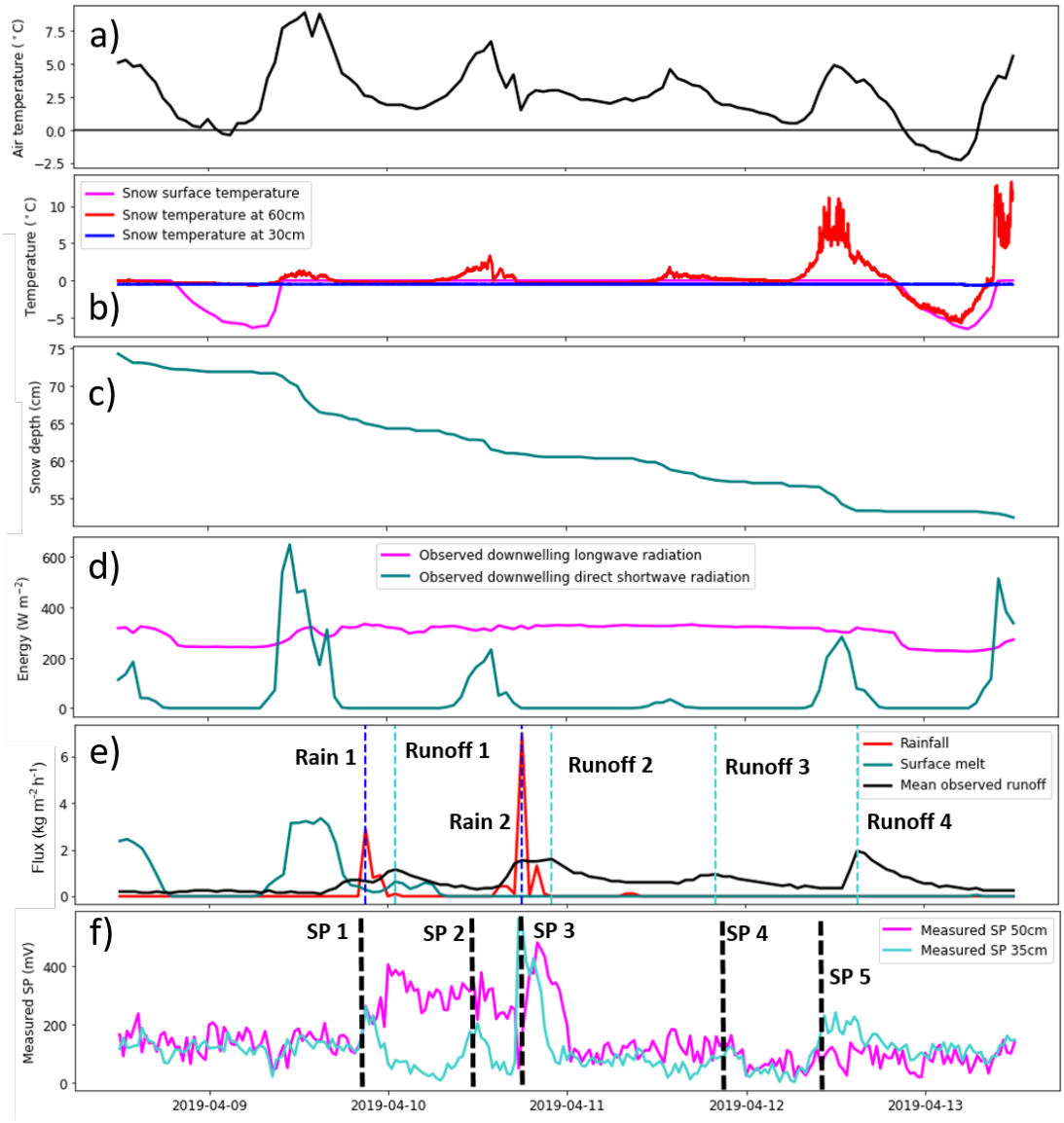


**Figure 4.8:** Meteorological, hydrological, and SP measurements for April 2019. a) Observed air temperature. b) Observed snow surface temperature, and PT100 temperature on poles at 30 cm and 60 cm. c) Observed snow depth. d) Observed incoming long- and shortwave radiation. e) Observed rainfall, modelled surface melt (using FSM2 - see section 5.2) and observed basal runoff. f) Mean observed SP signal from all electrodes at 35 and 50 cm. Mean standard error of the mean for this period was 55.5 mV at 35 cm and 32.6 mV at 50 cm.

**Figure 4.9:** Meteo France webcam image from midday on 12th April showing preferential melting has created cavities around the poles, exposing more electrodes than might be expected from the observed snow depth.

will have been taking place. The runoff follows a similar pattern however, with a small peak (Runoff 3) on the evening of the 11th too. Then, on the 12th, surface melting drives a broad peak in the SP signal (SP 5), which occurs just before a large peak (Runoff 4) is recorded in the runoff. From the 13th onwards, it is not clear if the electrodes were sufficiently buried in the snow to make sensible measurements.

## 4.5 2019-2020 season results

Due to the smaller amount of snow present during winter 2019-2020, and the COVID-19 pandemic disrupting fieldwork, there are fewer data available to analyse for this season. The snowpack was only deep enough to bury the lower SP electrodes for relatively short periods, and logger failures took place during some of this time. Figure 4.10 shows the temperature on the array plotted alongside snow depth. The upper thermometer (at 60 cm) shows large variations in temperature, showing it was above the snow surface for most of the season. The 30 cm thermometer is at or below 0°C for most of the season meaning it was below the snow surface. This means that for a large proportion of the season, the only SP electrode which was definitely buried was the lowest, at 20cm.

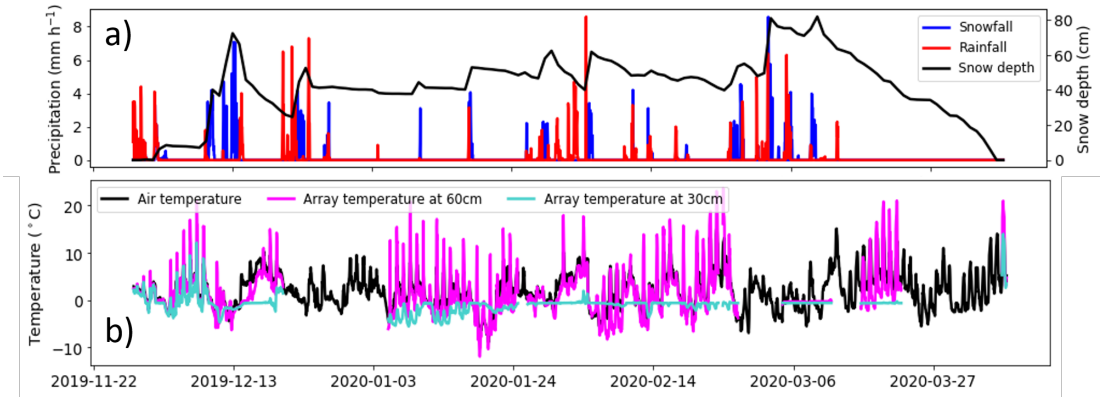


**Figure 4.10:** Winter 2019 - 2020 at Col de Porte: a) Observed precipitation and snowdepth. b) Observed air temperature and array temperature at 30 cm and 60 cm.

**Table 4.3:** Mean reference voltage and standard deviation for whole 2019 to 2020 season.

| Electrode pair | Mean differential voltage (mV) | Standard deviation (mV) |
|---|---|---|
| Reference 1 | 2.6 | 17.8 |
| Reference 2 | -6.4 | 21.2 |
| Reference 3 | 4.5 | 5.5 |

### 4.5.1 Reference electrode data

Figure 4.11 shows the whole season's reference data. Some gaps are visible where the power supply failed to the logger system, but there were no large jumps in the data as seen on some of the data in 2018-19. There was some drift in the measurements during December and January. Later in the season in February and March the measurements became stable with little variation, although the readings were interrupted by logger outages.

Table 4.3 shows the reference electrode uncertainties for the whole season. The uncertainties were similar to those measured in spring 2019.

### 4.5.2 Two periods of snow melt in spring 2020

Due to the limited data available in the 2019-2020 season, two short periods of melting have been selected when SP data were available and snow depth was enough to cover the lower two levels of electrodes on the array.

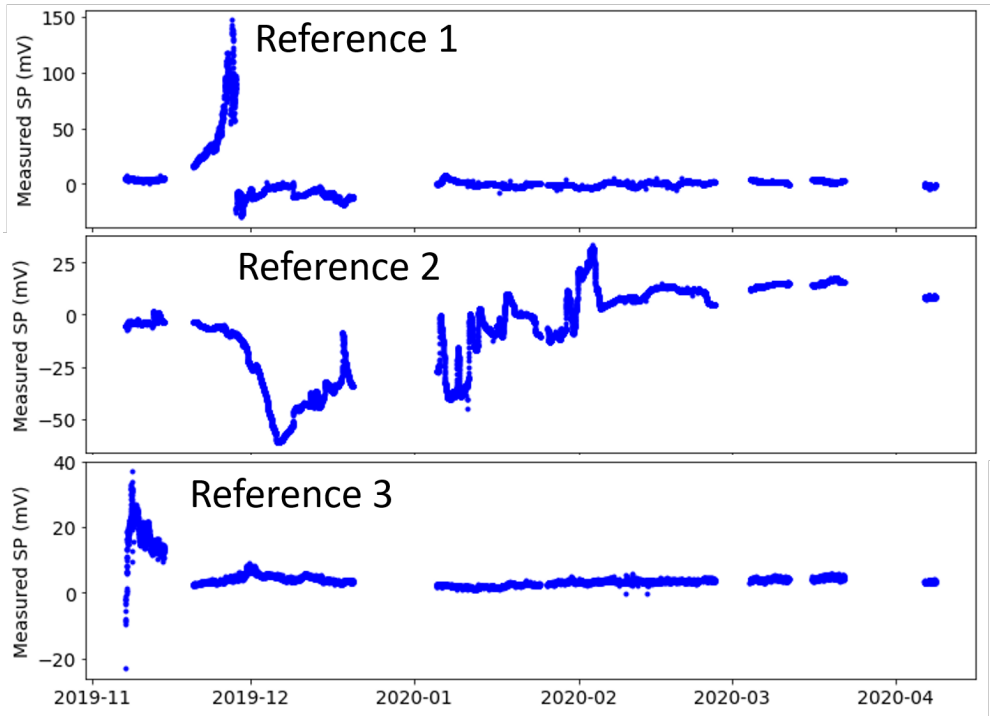


**Figure 4.11:** Full season reference electrode data 2019-2020.

#### Rain-on-snow 10th-11th March 2020

The first period is a small rain-on-snow event which occurred on the 10th-11th March. Figure 4.12 shows the measurements made during this period. The signal due to the rain is not strong because the rain event was only around 1 mm spread over several hours overnight from 10th to 11th March. The rainfall was accompanied with a rise in air temperature as shown on Figure 4.12c. The snow was deep enough to bury the lowest two electrodes which can be confirmed by noting that the array temperatures at 30 cm and 60 cm remained at zero (Figure 4.12c). The measured basal runoff and soil moisture content (4.12b and d respectively) show an increase corresponding to the rainfall and rising temperatures. It is not clear why the two soil moisture sensors gave such different readings as they were located close to one another, but water flow in snow and soil can be very heterogeneous which could account for the difference. They both show an increase in moisture content, which is especially clear in sensor 2 (in red). Data from the two lowest levels of SP sensors are shown on Figure 4.12f. A small peak in the SP reading can be seen during daylight hours on the 10th, corresponding to the increase in temperature and initiation of surface melting. This is followed by a broader peak corresponding to the rainfall duration. This occurs before the runoff is registered in the lysimeter and before the soil beneath the snow begins to get wetter, indicating that water movement within the snowpack is being registered before it reaches the base.

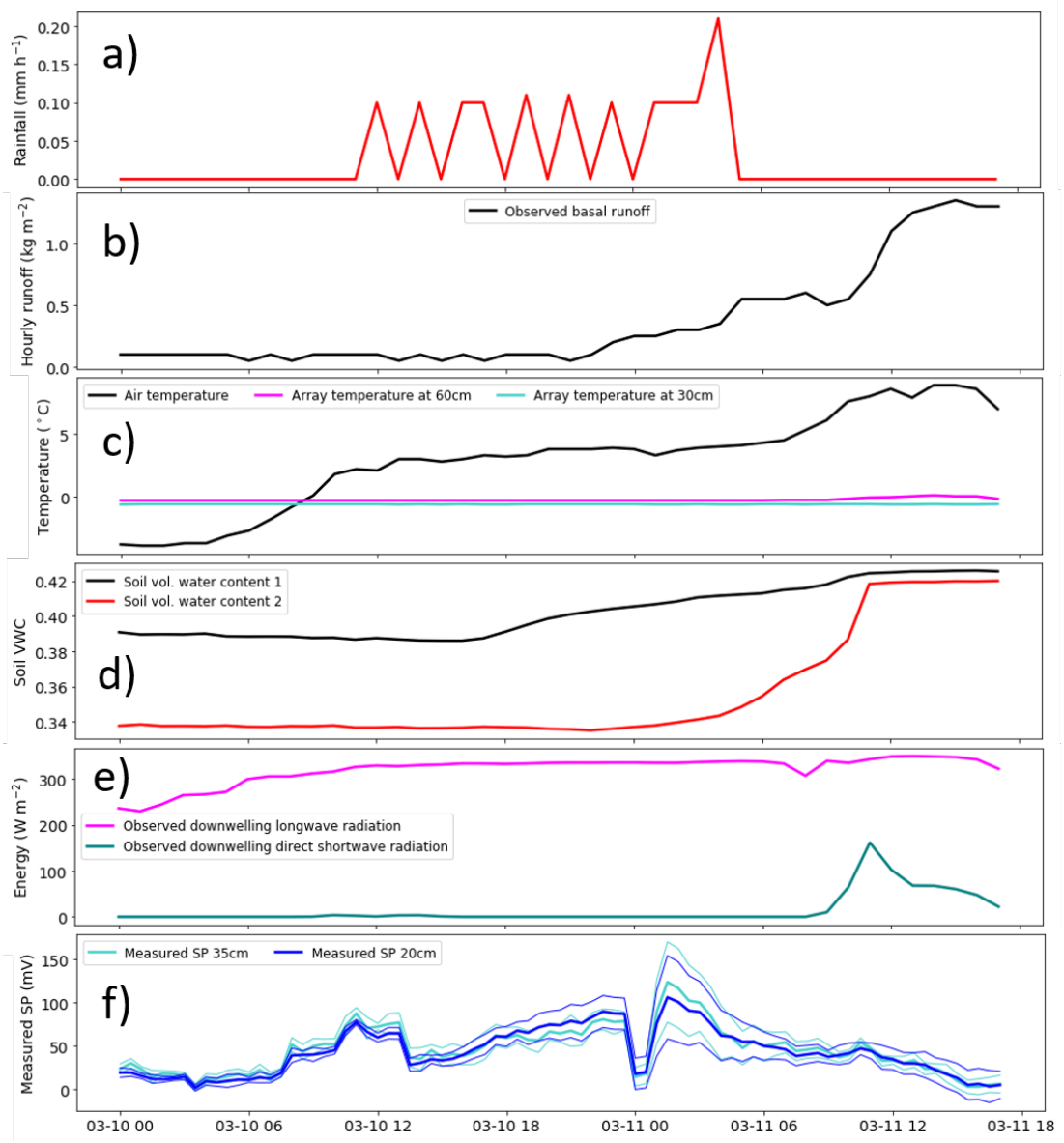


**Figure 4.12:** Rain on snow event in March 2020.

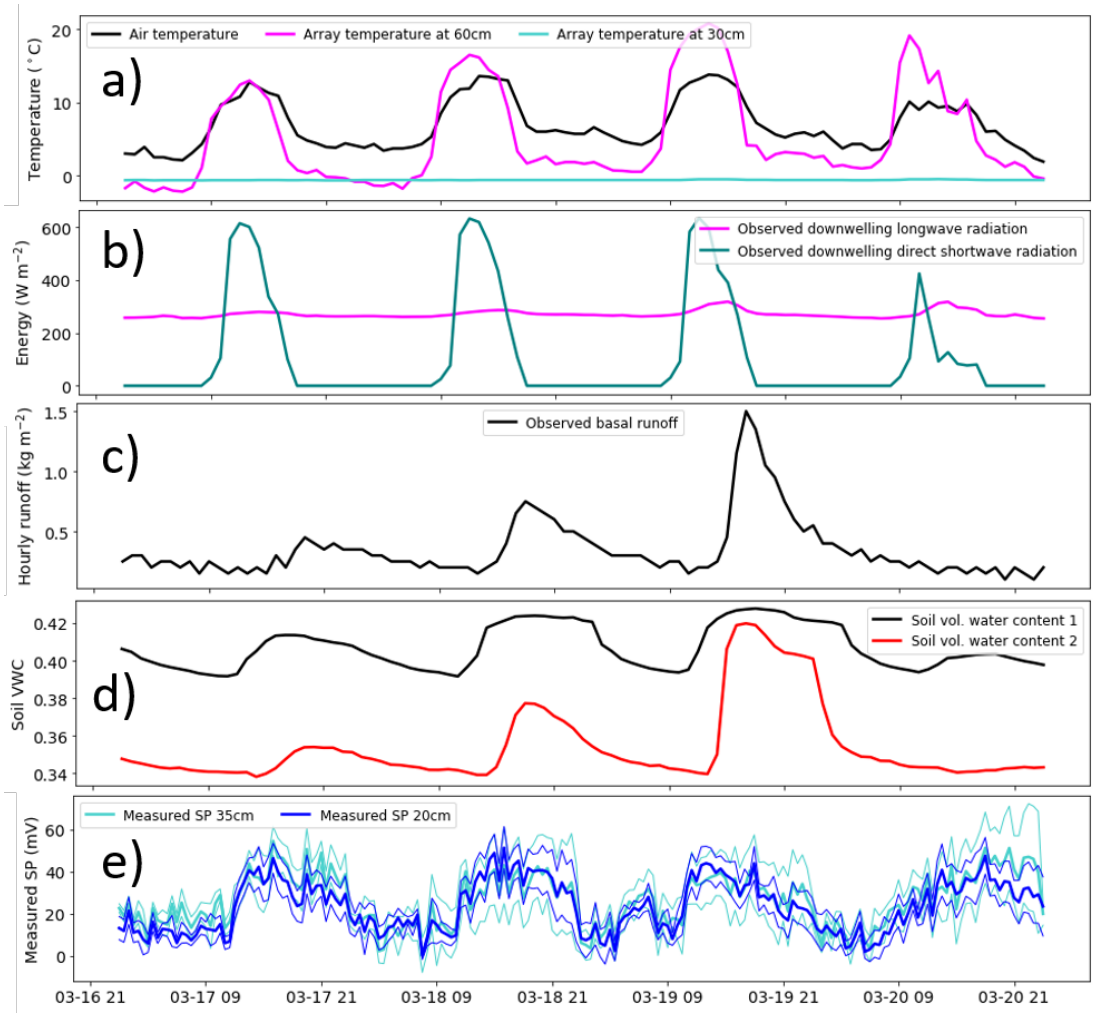


**Figure 4.13:** Diurnal melting in March 2020.

### Diurnal melting 17th-21st March 2020

Later on in March there was a period of clear diurnal melting which coincided with good data availability and a snowpack deep enough to bury some electrodes. Figure 4.13 shows meteorological, hydrological and geophysical data from 17-21st March during this melting period. It is clear from the temperatures (Figure 4.13a) that there is a strong diurnal signal in the air temperature and the temperature at 60 cm on the array. The lower PT100 thermistor at 30 cm remains buried in the snow throughout as it is isothermal at 0°C. The observed shortwave downwelling radiation (Figure 4.13b) shows a clear daily peak due to the prevailing sunny conditions. This clear diurnal signal can also be seen in the observed runoff, soil moisture and SP signal (Figures 4.13c, d and e). The basal runoff produced increases each day as the snowpack becomes more ripe and is able to support greater amounts of water flow. Similarly, the peak soil moisture registered on both sensors increases day on day as the melting takes place. In the SP signal, the peaks are broadly the same size throughout,

and occur before the runoff and soil moisture peaks, but after the peak in SW radiation and temperature. This indicates that the SP system is registering liquid water flow in the snowpack before it reaches the base. The signal measured at 35 cm is subject to greater errors later in the period. On the last daily peak (20th March) the standard error of the mean is around double that at 20 cm. This due to the electrode at 35 cm becoming exposed as the snow melts. It is likely that cavities around the poles develop through preferential melting (similar to what happened in 2019). This means that the 35 cm height electrodes may have become exposed when the measured snow depth was in fact greater than 35 cm.

## 4.6 Results summary

The electrical self potential results above from the 2018-19 and 2019-20 seasons show the utility of the SP method as a snow hydrology sensor. The key findings are:

- SP signals measured using lead electrodes can be related to meteorological and hydrological observations, showing they respond to meltwater movement in the snow.
- The timing of peaks in runoff corresponds closely to when meteorological data indicates the most melting will occur, but the magnitude of the peaks in SP signal cannot be explained with just the meteorological observations.
- The timing of peaks in SP signal caused by meltwater flux generally precede peaks in runoff measured using conventional basal runoff lysimeters, showing that SP measurements are sensitive to internal water flux.

The limitations with the equipment used have been highlighted, particularly regarding snow contact with the electrodes, and susceptibility to noise. The design did not allow differences in the SP signal either horizontally or vertically to be related to heterogeneities in the runoff, and the magnitude of the signal was difficult to relate to the magnitude of melting and runoff.

# Chapter 5

# Snow hydrology modelling

## 5.1 Introduction

This chapter outlines the snow hydrology modelling part of this project. Firstly, the FSM2 model is introduced (5.2). Then, FSM2 is evaluated at a mid-elevation Alpine site over a long period in order to choose the parameterisations which gave the best model performance (5.3). Next, FSM2 was driven over the whole Chartreuse Alps using high resolution numerical weather prediction data. This made evaluating the performance of the snow model when forced with model data possible through comparisons with in situ data at Col de Porte but also using remotely-sensed data when available (5.4). Lastly, FSM2 was coupled to an electrical model to investigate the possibility of using self potential measurements to calibrate water flux dynamics within the snowpack i.e. before they reach the base to be measured in a lysimeter (5.5).

## 5.2 Flexible Snow Model (FSM2)

The snow modelling carried out in this project uses the open-source Flexible Snow Model (FSM2), which is the second version of the Factorial Snow Model (FSM) (Essery, 2015). FSM was developed to investigate how differing complexities of process representations affect model performance. Previous work presented an ensemble approach with 1701 model configurations (Essery et al., 2013). This found that whilst no model configuration gave the best simulation every winter, model configurations with prognostic representations of snow albedo, density and liquid water content gave the best overall performance. Following on from this, FSM was developed as more systematic way of investigating the effect of differing parametrisations. Five parametrisations can be switched on or off giving thirty two possible model configurations. These parametrisations are prognostic equations for albedo, density and snow liquid water content, and diagnostic equations for the dependence of snow thermal conductivity on density, and the dependence of turbulent fluxes on atmospheric stability. FSM2 extends FSM by adding additional physics and driving options. These include forest canopy processes (not discussed here) and extra density and liquid water storage representations.

FSM2 has been used in a variety of research, including investigating the effect of forest canopies on snow processes (Mazzotti et al., 2020), investigating snow dynamics in the Lebanese mountains (Alonso-González et al., 2021), and for looking at how snow cover changes affect montane biodiversity in the Scottish Highlands (Priestley and Ewing, 2022).

## 5.3 Evaluating FSM2 at Col de Porte

In order to evaluate FSM2's performance, the long series of driving and evaluation data available at Col de Porte were used. The ability to switch easily between parametrisations in FSM2 meant that investigating the effect of varying levels of process representation was possible. Given the importance of liquid water to self potential, the key parameter that was varied was the representation of water storage in the snowpack. FSM2 has three levels of representation: a simple free draining representation, a bucket model where each layer has a given water storage capacity, and a gravitational drainage model where the Richards equation (Richards, 1931) is solved numerically.

### 5.3.1 Comparative statistics

The Nash-Sutcliffe Efficiency (NSE) (Nash and Sutcliffe, 1970) is calculated as:

$$1 - \frac{\text{variance of observations}}{\text{variance of model}} \tag{5.1}$$

It is used to assess the predictive skill of hydrological models. A value of 0 means that the model has the same predictive skill as the mean of the observations. A value of close to 1 means the model has high predictive skill. Negative values of the NSE indicate that the model predictions have a higher variance than the observed value, and therefore the observed mean is a better predictor than the model.

The Kling-Gupta Efficiency (KGE) (Gupta et al., 2009) is an alternative measure of goodness of fit between model and observations. The KGE statistic has its optimum value at unity. KGE is calculated as:

$$KGE = 1 - \sqrt{(r-1)^2 + (\beta-1)^2 + (\alpha-1)^2} \tag{5.2}$$

$$\beta = \frac{\mu_s}{\mu_o} \tag{5.3}$$

$$\alpha = \frac{\sigma_s}{\sigma_o} \tag{5.4}$$

where $r$ is the coefficient of correlation, and $\mu_s$, $\mu_o$, $\sigma_s$ and $\sigma_o$ are the mean and standard deviation of the simulated and observed data respectively.

**Table 5.1:** Hourly data measured at Col de Porte used to drive FSM2.

| Variable | Description | Units |
|---|---|---|
| SW | Incoming shortwave radiation | W $m^{-2}$ |
| LW | Incoming longwave radiation | W $m^{-2}$ |
| Sf | Snowfall rate | kg $m^{-2}$ $s^{-1}$ |
| Rf | Rainfall rate | kg $m^{-2}$ $s^{-1}$ |
| Ta | Air temperature (1.5 m above snow surface) | K |
| RH | Relative humidity (1.5 m above snow surface) | % |
| Ua | Wind speed (10m) | m $s^{-1}$ |
| Ps | Surface air pressure | Pa |

### 5.3.2 Driving data

Meteorological datasets are produced at Col de Porte with the specific intention of driving and validating hydrological models. The data are available from 1993 to 2020 at hourly resolution, and has been quality controlled and validated against manual observations and companion measurements. The instrumentation and site set up is detailed in Lejeune et al. (2019). Table 5.1 shows the meteorological data collected at Col de Porte which were used to drive FSM2.

### 5.3.3 Evaluation data

In order to evaluate the performance of FSM2 at Col de Porte, observed data were available. The key variables required to evaluate the performance of FSM2 in hydrological applications are snow water equivalent (SWE) and snowmelt runoff. Long time series (2001 - 2015) of daily SWE and hourly runoff (1993 - 2017) are available at Col de Porte. Longer period SWE data are available in the approximately weekly manual snow pit data available from 1960 - 2017, but it is more difficult to systematically evaluate model performance with lower frequency data like this. The daily SWE data are measured using a cosmic ray detector operated by EDF Energy at the Col de Porte site (Kodama et al., 1979; Morin et al., 2012). It has been found to agree well with the manual weekly measurements carried out by Meteo France staff (see Figure 5.1) but is prone to over-reading at the beginning and end of the season, possibly due to moisture in the soil affecting the calibration in snow-free conditions (personal communication with Yves Lejeune).

The snowmelt runoff at Col de Porte is measured using two lysimeters located next to one another. They operate using the same basic principles (see 1.4.1) but have different diameter collecting surfaces: 1 $m^2$ and 5 $m^2$. More details of the lysimeters are available in Lejeune et al. (2019). As Figure 5.2 shows, in most years, there is good agreement between the two lysimeters and the annual precipitation. Some difference is expected. For example, preferential flow within the snow could mean the lysimeter is capturing a different amount of runoff than is being generated directly above it. Sublimation and wind transport contribute

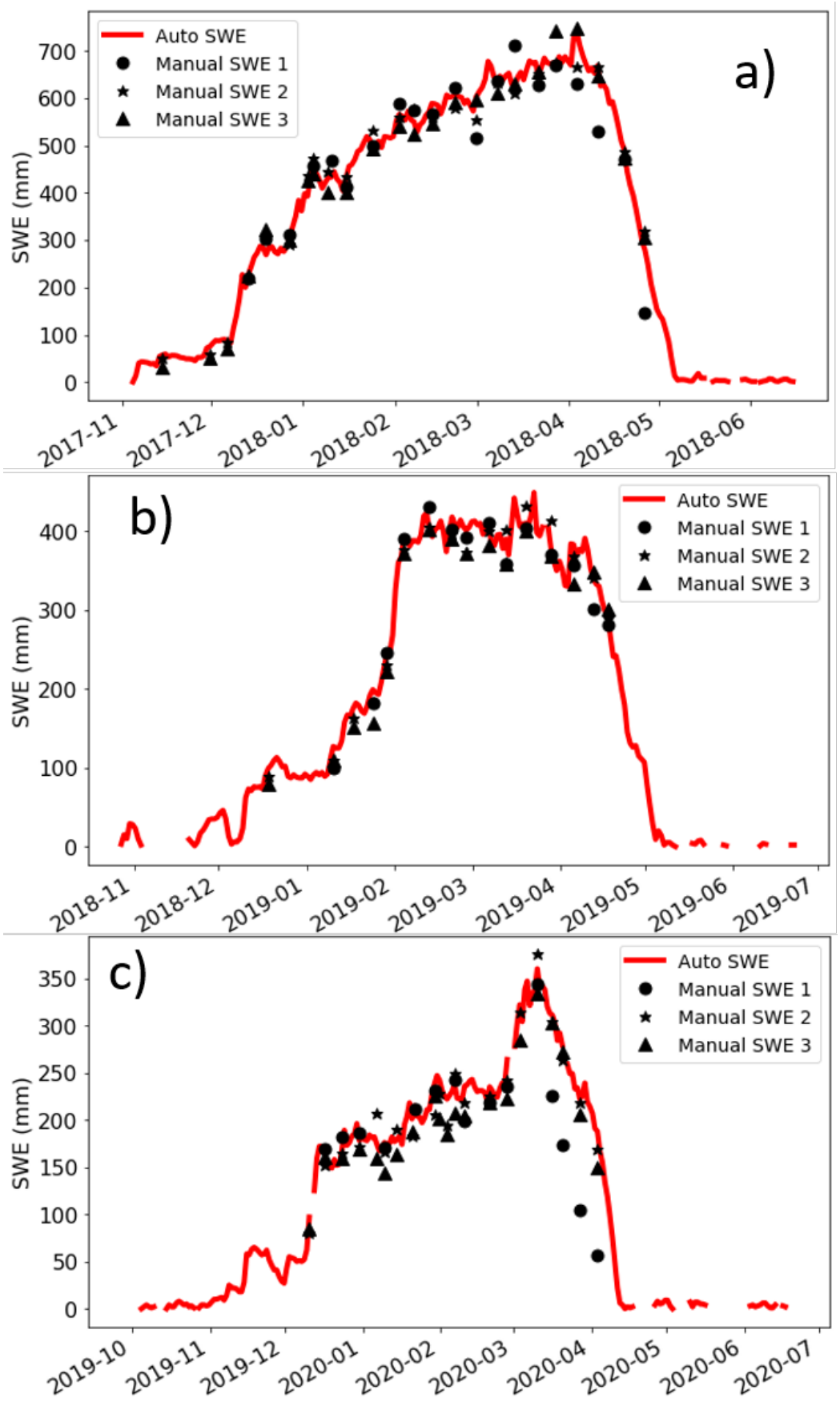


**Figure 5.1:** Comparison between three manual snow pit SWE measurements (SWE 1, 2 and 3), and daily automatic SWE from the EDF cosmic ray detector for a) 2017-18, b) 2018-19 and c) 2019-20.

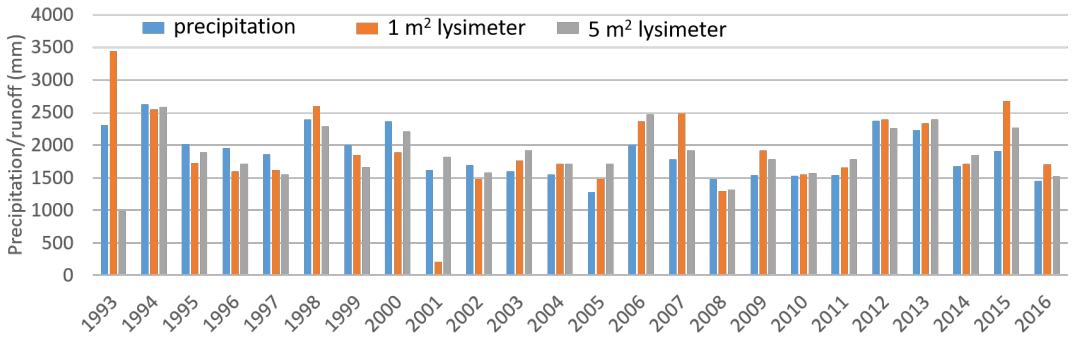


**Figure 5.2:** Annual precipitation and measured runoff at Col de Porte.

to differences between precipitation and runoff amount. In 1993, the 1 $m^2$ read much more than the precipitation, and the 5 $m^2$ much less. In 2001 the 1 $m^2$ lysimeter clearly suffered errors as the annual total is much lower than the precipitation and the 5 $m^2$ measurements. When evaluating the performance of FSM2, the runoff data from 1993 were not used, and in 2001 the data from the 1 $m^2$ device were removed from the analysis. To quantify how variable the runoff measurements were (both spatially across the site, and due to instrument differences), the 1 m $^2$ and 5 $m^2$ instruments were directly compared to one another. Figure 5.3 shows the two instrument datasets plotted against each other for accumulations at different timescales. As might be expected, the best agreement is over longer timescales. There is still some difference between the two instruments at this timescale though, with the $r^2$ value only at 0.837. The $r^2$ value for 6 hour accumulations is lower (0.825), and for hourly it is lower still at 0.782. This shows that the runoff measurements are subject to uncertainty caused by instrument variability, and by the heterogeneous nature of liquid water flux in snow. It also gives an upper bound for the performance of a snow hydrology model.

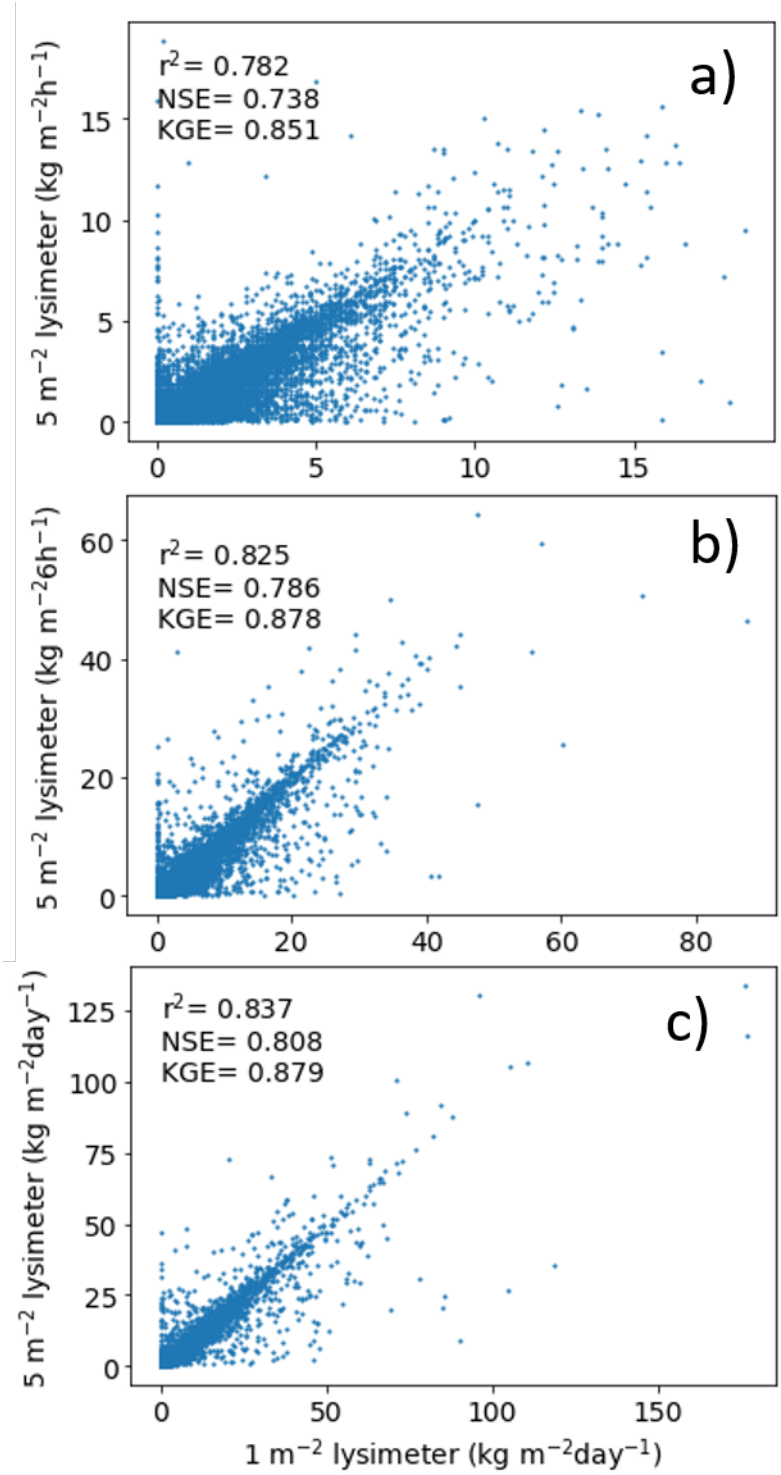


**Figure 5.3:** Comparative statistics for the 1 $m^2$ and 5 $m^2$ lysimeters at hourly, 6 hourly and daily timescales (a, b and c respectively).

### 5.3.4 FSM2 configurations

FSM2 was evaluated using three different hydrology and two different density configurations. Differing layering schemes were investigated too: the default three layer set-up, and a ten layer set-up which was the same as that used for self-potential modelling.

#### FSM2 density

FSM2 has three options for density. The first is to keep density constant, which was not tested here. Otherwise, the density changes according to a compaction rate function. The second option compacts snow as a function of snow age. The compaction rate function is based on that in the Canadian Land Surface Scheme (CLASS) model (Verseghy, 1991) and takes account of different prescribed maximum densities for snow that is subzero temperature or melting. The third option calculates the compaction rate as a function of overburden i.e. the weight of the snow above the layer in question, and thermal metamorphism. This follows the scheme used in the French land surface model ISBA-ES (Interaction Sol-Biosphère-Atmosphère - Explicit Snow) (Boone and Etchevers, 2001).

#### FSM2 hydrology

FSM2 has three options for modelling liquid water in the snowpack. The first option tested was the free draining option. In this very simple representation, rain or meltwater at the snow surface is drained immediately to the base of the snowpack, and the model snow is incapable of retaining any liquid water in the snow layers. The second hydrology option is a 'bucket' storage scheme. Each model layer of snow has a maximum liquid water capacity at 0°C, $W_{max}$, based on the porosity and the layer depth, which is given by (**?**):

$$W_{max} = \rho_w \phi_{layer} \Delta h W_{irr} \tag{5.5}$$

where $\rho_w$ is the density of water, $\phi_{layer}$ is the layer porosity, $\Delta h$ is the layer depth and $W_{irr}$ is the irreducible water mass. Water in excess of this capacity drains to the layer below. Water in a layer below 0°C will freeze, releasing latent heat, until the layer is brought to 0°C. The third option is a gravitational drainage scheme. This solves the Richards equation numerically for vertical flux of water in the snow. It also takes account of water freezing in subzero layers. Downward water flux due to gravitational drainage, $Q_w$, is parameterised as (Clark et al., 2017):

$$Q_w = k_{sat} \left( \frac{\theta_w - \theta_r}{\phi - \theta_r} \right)^3 \tag{5.6}$$

where $\theta_w$ is volumetric liquid water content, $\phi$ is porosity and irreducible water content is the irreducible water saturation multiplied by the porosity ( $\theta_r = S_w^{irr} \phi$).

The saturated hydraulic conductivity, $k_{sat}$, is parameterised as (Shimizu, 1970):

$$k_{sat} = 0.31 \frac{\rho_w g r^2}{\mu_w} \exp\left(-7.8 \frac{\rho_s}{\rho_w}\right) \tag{5.7}$$

where $g$ is the acceleration due to gravity, $\mu_w$ is the dynamic viscosity of water, and $r$ and $\rho_s$ are snow grain radius and snow density respectively. Internal phase changes and compaction are adjusted for, then liquid water content and flux are related by the balance equation:

$$\frac{\partial \theta_w}{\partial t} = -\frac{\partial Q_w}{\partial z}. \tag{5.8}$$

This is solved by discretising using an implicit upwind scheme, then the layer liquid water contents are found using the Newton-Raphson method. The full equations are in appendix B.

### 5.3.5 FSM2 results

#### Long period evaluation

As detailed above, FSM2 was run at Col de Porte using driving data available from 1993 - 2020. The results were compared to observed SWE data in the period from 2001 - 2015, and to observed runoff from 1994 - 2017. The model performance was evaluated using the correlation coefficient, the Nash-Sutcliffe Efficiency and the Kling-Gupta Efficiency. Tables 5.2 and 5.3 show the performance evaluation results for a three layer and ten layer model configuration.

Daily SWE at Col de Porte is predicted well by all configurations of FSM2 that were tested (see Tables 5.2,5.3 and Figure 5.4). The worst predictions are made by the free draining configuration with density as a function of overburden, but the correlation is still above 0.88 for both the three layer and ten layer models using this configuration. Using age to parameterise density in combination with gravitational drainage gives the best performance for SWE, with a correlation of >0.95 for the ten layer model. It is not unexpected that SWE is modelled well: SWE changes comparatively slowly over the snow season, especially compared to other variables such as runoff.

FSM2 has better predictive skill for daily runoff than for shorter runoff timescales. For both the three layer and ten layer model runs, parametrising density as a function of age produces better results than using overburden. Tables 5.2 and 5.3 show results for both the three and ten layer models. The free draining hydrology model performs worst for both density parametrisations at hourly timescales. There is a smaller difference in performance at 6 hourly timescales and at daily timescales there is very little difference between the hydrology parametrisations. The free draining hydrology gives almost identical results in the three layer and ten layer configurations, because the water drains straight to the base of the snowpack regardless of the number of layers. Slight differences in the performance between the three layer and ten

**Table 5.2:** Comparative statistics for six different configurations of FSM2 using a three layer representation of the snowpack (two density options and three hydrology options) evaluated against daily SWE and hourly, six-hourly and daily runoff measurements.)

| | | Density function of age | | | Density function of overburden | | |
|---|---|---|---|---|---|---|---|
| variable | **Hydrology** | $r^2$ | **NSE** | **KGE** | $r^2$ | **NSE** | **KGE** |
| SWE | free draining | 0.928 | 0.789 | 0.584 | 0.898 | 0.732 | 0.539 |
| | bucket | 0.951 | 0.901 | 0.769 | 0.926 | 0.835 | 0.668 |
| | gravitational | 0.95 | 0.903 | 0.781 | 0.927 | 0.84 | 0.679 |
| 1h runoff | free draining | 0.326 | -0.079 | 0.519 | 0.318 | -0.092 | 0.515 |
| | bucket | 0.326 | -0.119 | 0.506 | 0.326 | -0.096 | 0.514 |
| | gravitational | 0.353 | 0.002 | 0.549 | 0.368 | 0.044 | 0.565 |
| 6h runoff | free draining | 0.499 | 0.328 | 0.68 | 0.491 | 0.323 | 0.678 |
| | bucket | 0.484 | 0.263 | 0.651 | 0.496 | 0.306 | 0.67 |
| | gravitational | 0.486 | 0.289 | 0.663 | 0.523 | 0.367 | 0.67 |
| 24h runoff | free draining | 0.64 | 0.602 | 0.795 | 0.637 | 0.602 | 0.793 |
| | bucket | 0.599 | 0.529 | 0.767 | 0.639 | 0.594 | 0.794 |
| | gravitational | 0.585 | 0.509 | 0.757 | 0.636 | 0.592 | 0.793 |

**Table 5.3:** Comparative statistics for six different configurations of FSM2 using a ten layer representation of the snowpack (two density options and three hydrology options) evaluated against daily SWE and hourly, six-hourly and daily runoff measurements.)

| | | Density function of age | | | Density function of overburden | | |
|---|---|---|---|---|---|---|---|
| variable | **Hydrology** | $r^2$ | **NSE** | **KGE** | $r^2$ | **NSE** | **KGE** |
| SWE | free draining | 0.923 | 0.765 | 0.554 | 0.889 | 0.704 | 0.511 |
| | bucket | 0.956 | 0.901 | 0.748 | 0.914 | 0.799 | 0.622 |
| | gravitational | 0.956 | 0.907 | 0.767 | 0.915 | 0.805 | 0.632 |
| 1h runoff | free draining | 0.324 | -0.08 | 0.519 | 0.315 | -0.094 | 0.514 |
| | bucket | 0.491 | -0.11 | 0.509 | 0.324 | -0.092 | 0.515 |
| | gravitational | 0.357 | 0.005 | 0.55 | 0.363 | 0.034 | 0.561 |
| 6h runoff | free draining | 0.5 | 0.335 | 0.683 | 0.487 | 0.32 | 0.677 |
| | bucket | 0.491 | 0.28 | 0.658 | 0.497 | 0.316 | 0.674 |
| | gravitational | 0.494 | 0.303 | 0.668 | 0.523 | 0.37 | 0.697 |
| 24h runoff | free draining | 0.644 | 0.609 | 0.797 | 0.634 | 0.599 | 0.79 |
| | bucket | 0.611 | 0.55 | 0.776 | 0.644 | 0.605 | 0.797 |
| | gravitational | 0.594 | 0.526 | 0.764 | 0.641 | 0.602 | 0.796 |

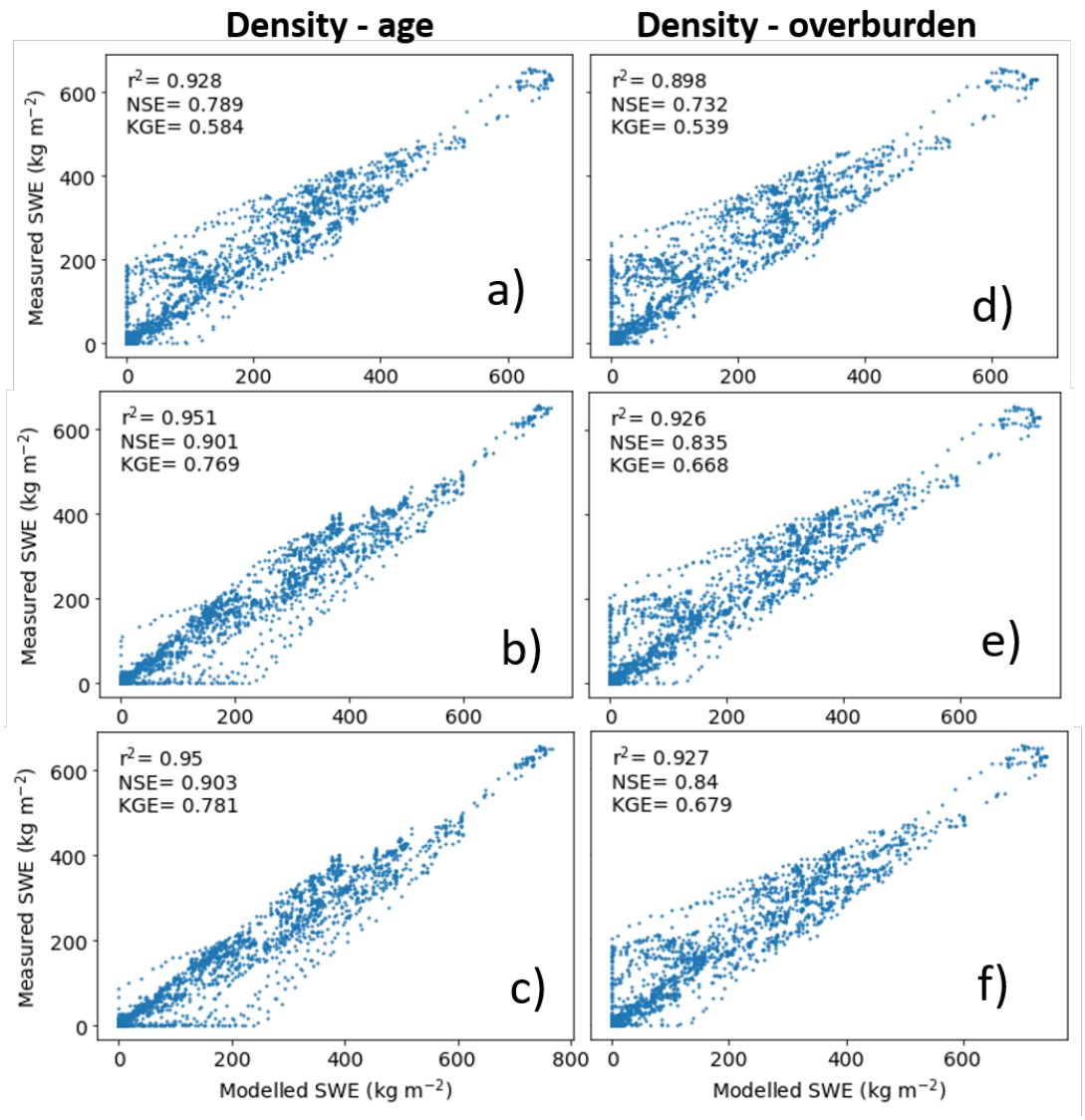


**Figure 5.4:** Modelled daily SWE plotted against measured daily SWE for different model hydrology and density parameterisations. a, b and c show results for free draining, bucket model and gravitational drainage hydrology respectively for density as a function of age. d, e and f show free draining, bucket model and gravitational drainage hydrology respectively for density as a function of overburden.

layer models are due to numerical errors in the discretisation of the model timesteps. Figures 5.5 and 5.6 show the contrasts in performance between the hourly and daily timescales, with a larger difference in performance between the hydrology parameterisations at hourly timescales.

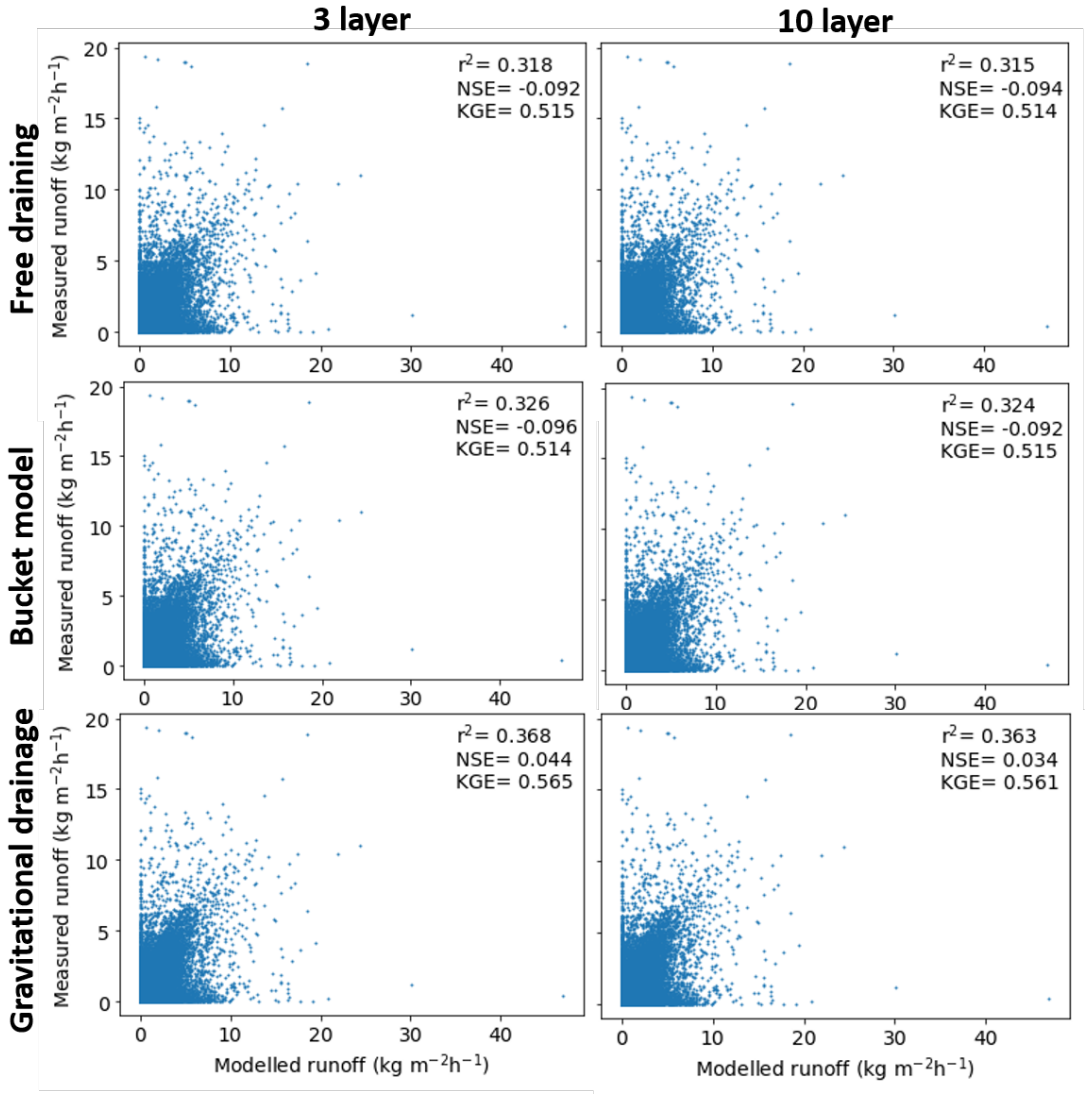


**Figure 5.5:** Modelled hourly runoff plotted against measured hourly runoff for different model hydrologies and layer configurations. These model runs parameterise density as a function of overburden.

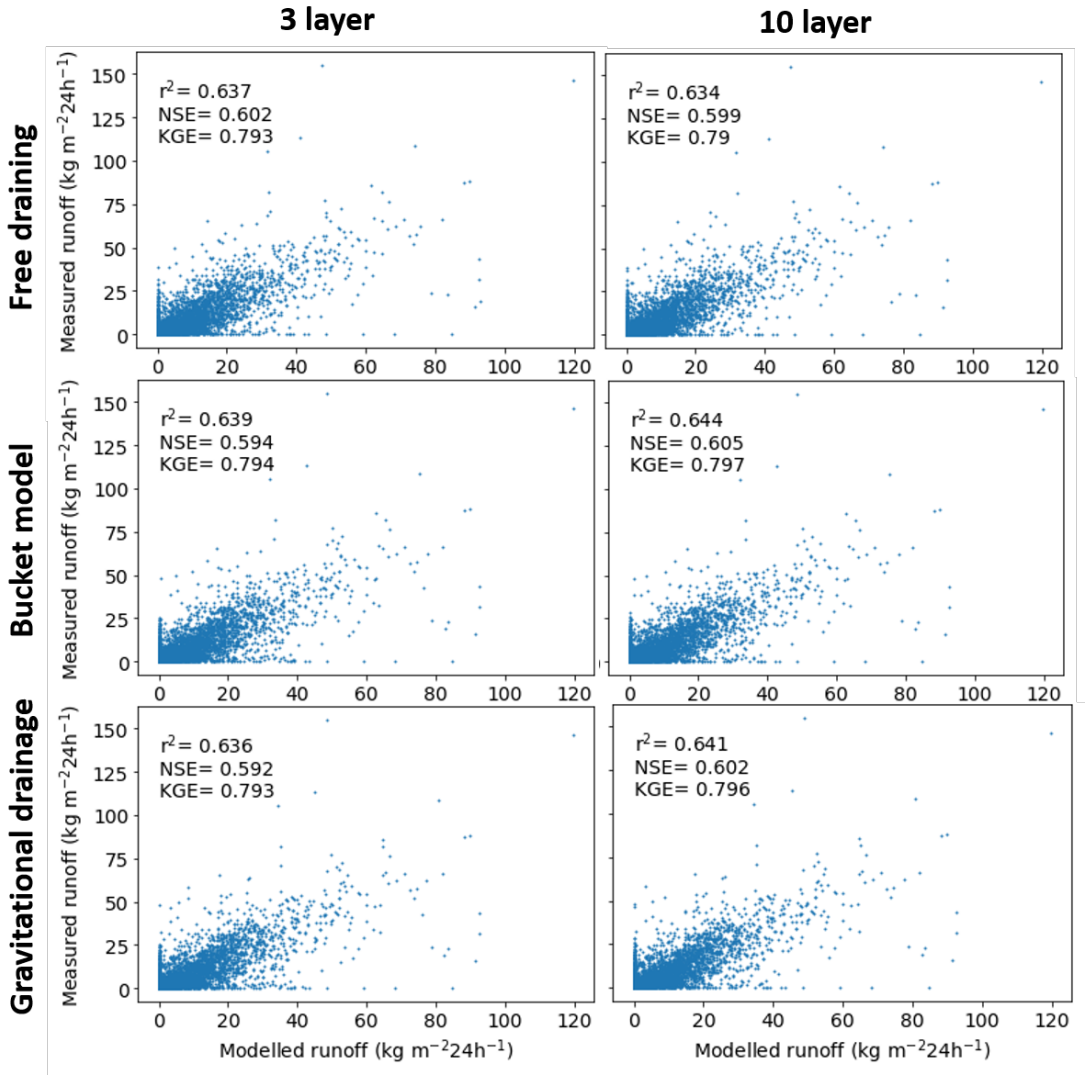


**Figure 5.6:** Modelled daily runoff plotted against measured daily runoff for different model hydrologies and layer configurations. These model runs parameterise density as a function of overburden.

### Short period hydrology evaluation

As well as evaluating FSM2 over many seasons, it was evaluated qualitatively at shorter timescales too, using data for a period of strong diurnal melting in late March 2019. It is clear when evaluating over shorter timescales how markedly the three model hydrologies differ, for both density formulations. Figures 5.7 and 5.8 show that all three models move runoff to the base of the snowpack too soon compared to the observations. This is most apparent at the beginning of the period shown as the snowpack was less ripe at that point. As it ripens, the mismatch between modelled and measured runoff peaks lessens. In terms of magnitude, the free draining and bucket models overestimates the runoff peak magnitudes most, but all three models do overestimate to some extent. In terms of shape of the runoff curve, both the free draining and bucket models have too narrow a peak, and the peak is symmetrical. The gravitational drainage model peak shapes resemble the observations better, with a sharp rise and a slower 'tail', although it still tails off too quickly when compared to observations. Switching between density formulations changes the results most for the gravitational model - density as a function of age fits the runoff peaks extremely well in terms of magnitude. The shape has the same issues described above in both formulations.

When modelled cumulative runoff is compared to measured cumulative runoff (bearing in mind the limitations in the observational data highlighted above) it is clear that over a whole winter season, FSM2 can predict cumulative runoff well. Figures 5.9 and 5.10 show the cumulative runoff for the three model hydrology and two density parametrisations compared with observed runoff, and Figure 5.11 shows measured and modelled snowdepth over the same period. Looking at runoff with density as a function of overburden, the free draining model compares well with the observations in the early part of the season, and is the closest model to the observations until mid-February. From this point onwards the free draining model produces more runoff sooner than the observations, and there is a mismatch for the rest of the season. The bucket and gravitational models produce less runoff than observations throughout, with the largest gap existing just before the onset of spring melting at the end of February. The gap then narrows but the runoff produced stays lower than the observed values. The bucket and gravitational models are very similar to one another, but by the main melting period the bucket model produces runoff slightly earlier than the gravitational model. With density as a function of age (in Figure 5.9) the free draining model performs best, and the bucket and gravitational drainage models perform worse than with density as a function of overburden.

It can be seen from Figures 5.11 and 5.12 that all three hydrology models with both density configurations predict the snowdepth well through the first half of the season, although at the peak snowdepth in early February all configurations overdo the maximum by about 20 cm. Through the second half of the season, there is more variability in the model performance. With density as a function of age, the three hydrology models track the observed snow

well until mid-March, then they start to diverge. The free draining model performs best and follows observations well, and the bucket model and gravitational model both diverge from observations. This results in the bucket and gravitational models prolonging snow cover into May, when the observed snow off date was in late April. With density modelled as a function of overburden, the free draining model initially performs best. As the main melting period begins in March, snow is removed too quickly by the free draining model compared to observations and the other two models. This means that the snow-off date in the free draining model is about a week early. The bucket and gravitational models match the observed snowdepth better through March and April, with the snow-off date in both models matching observations very well.

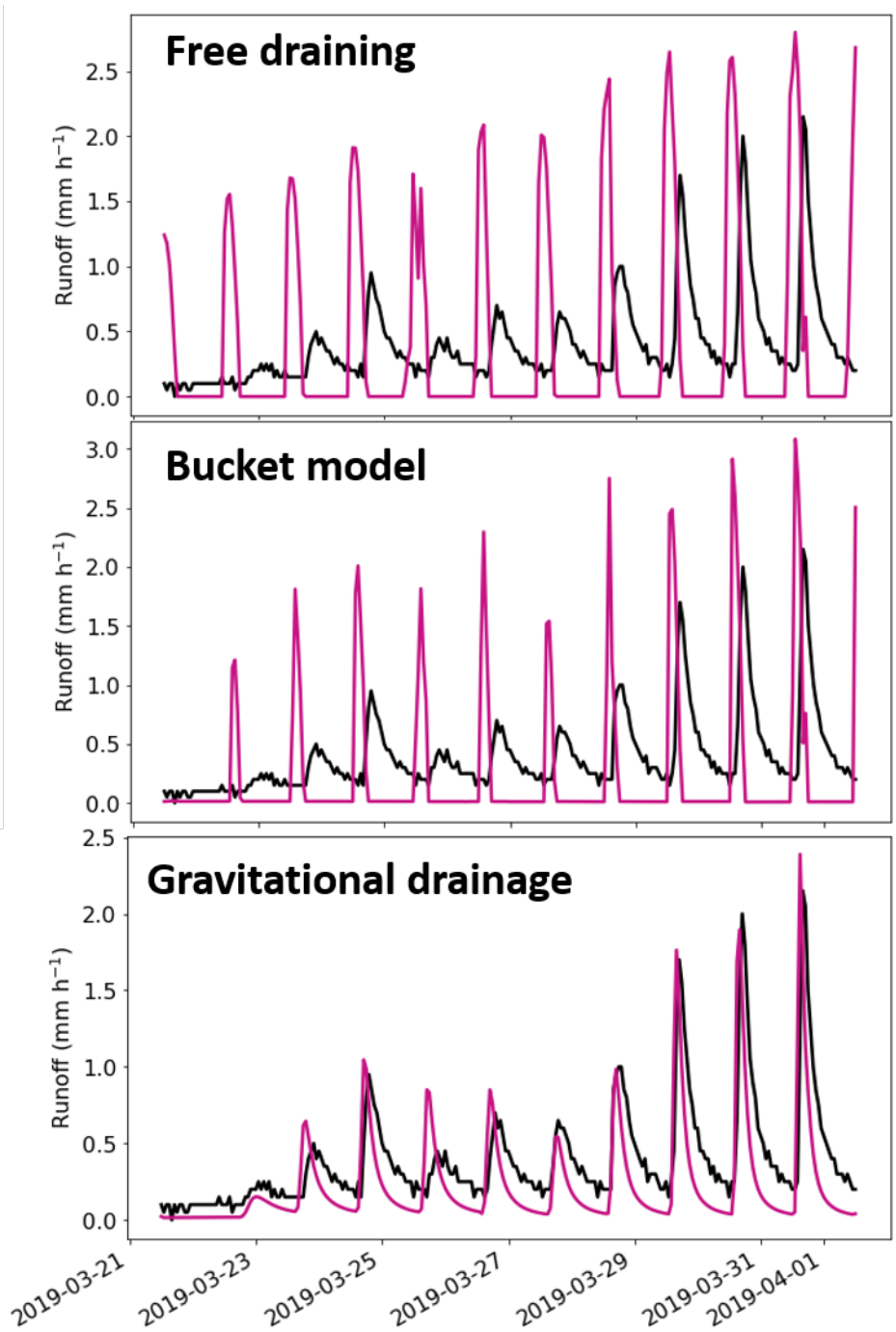


**Figure 5.7:** Modelled hourly runoff plotted against measured hourly runoff for different model hydrologies in late March 2019. These model runs parameterise density as a function of age. Pink is modelled runoff and black is observed runoff.

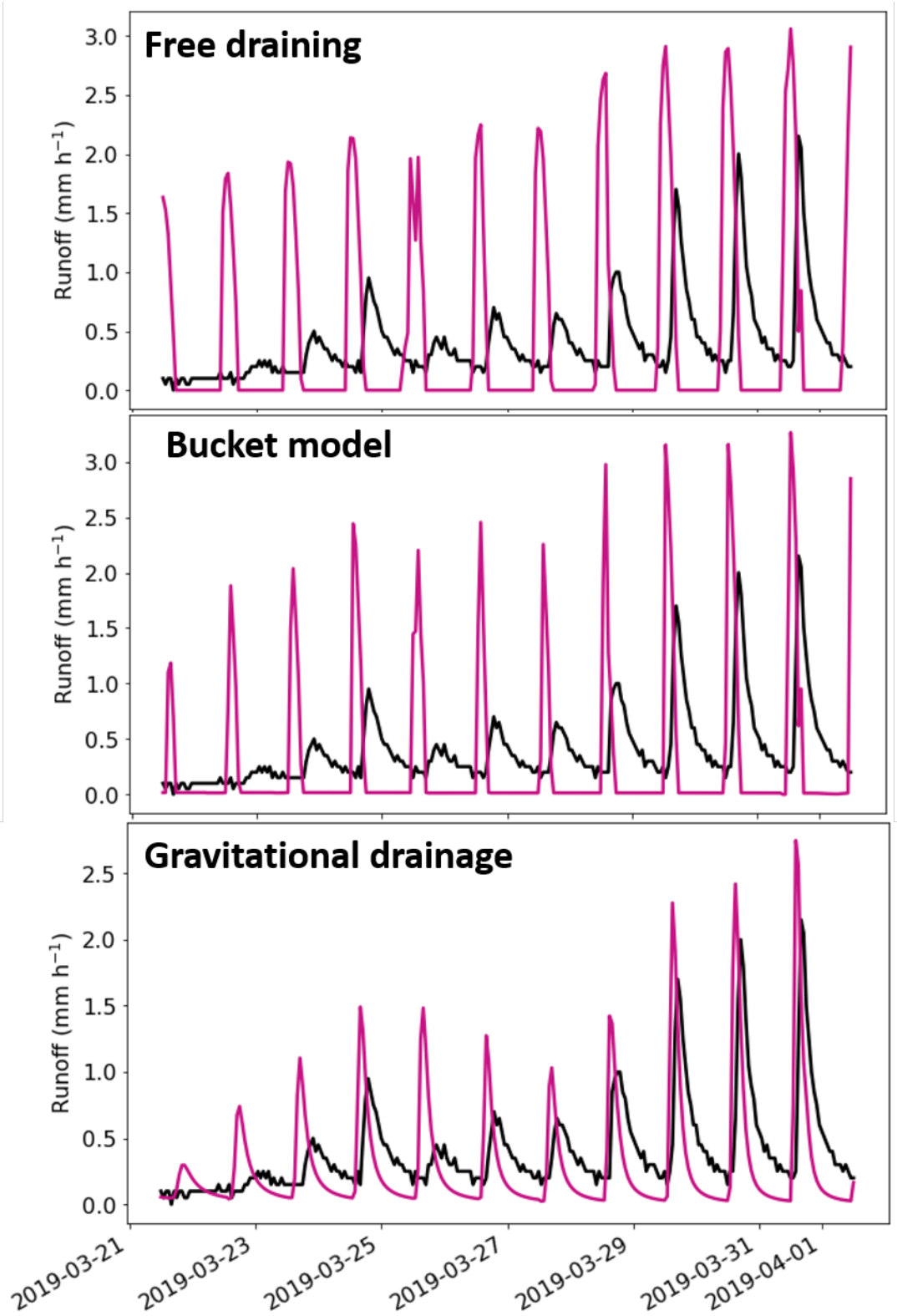


**Figure 5.8:** Modelled hourly runoff plotted against measured hourly runoff for different model hydrologies in late March 2019. Pink is modelled runoff and black is observed runoff. These model runs parameterise density as a function of overburden.

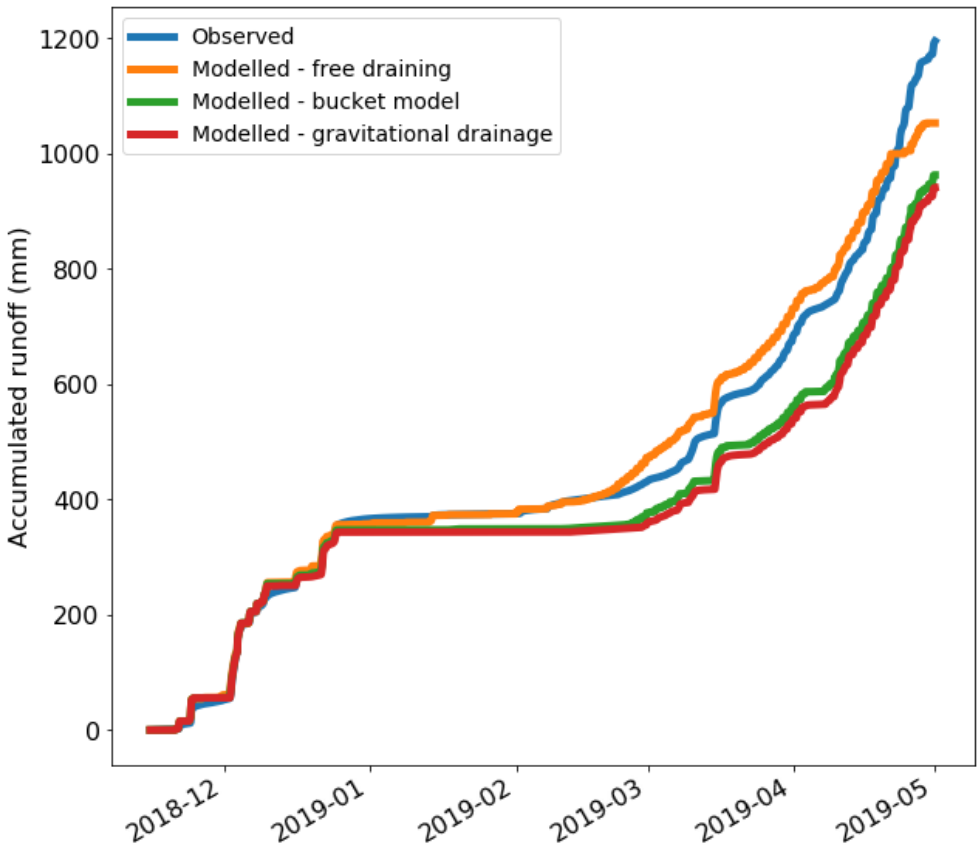


**Figure 5.9:** Measured and modelled cumulative runoff for the winter 2018-2019 season, parameterising density as a function of age.

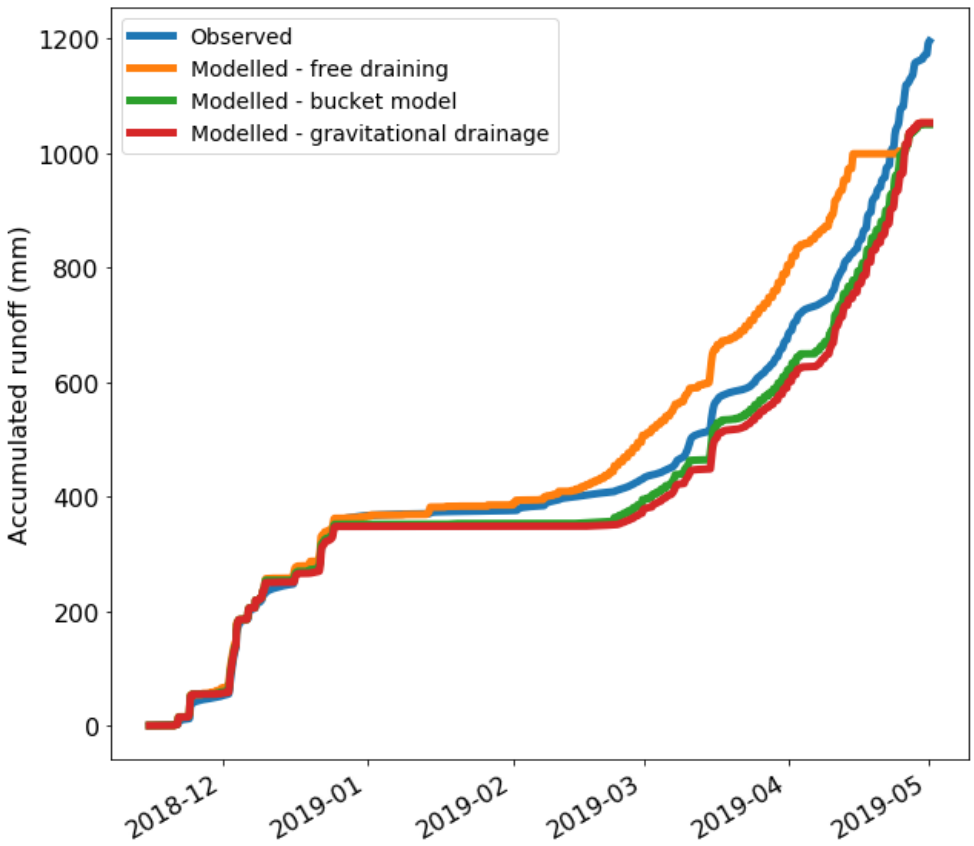


**Figure 5.10:** Measured and modelled cumulative runoff for the winter 2018-2019 season, parameterising density as a function of overburden.

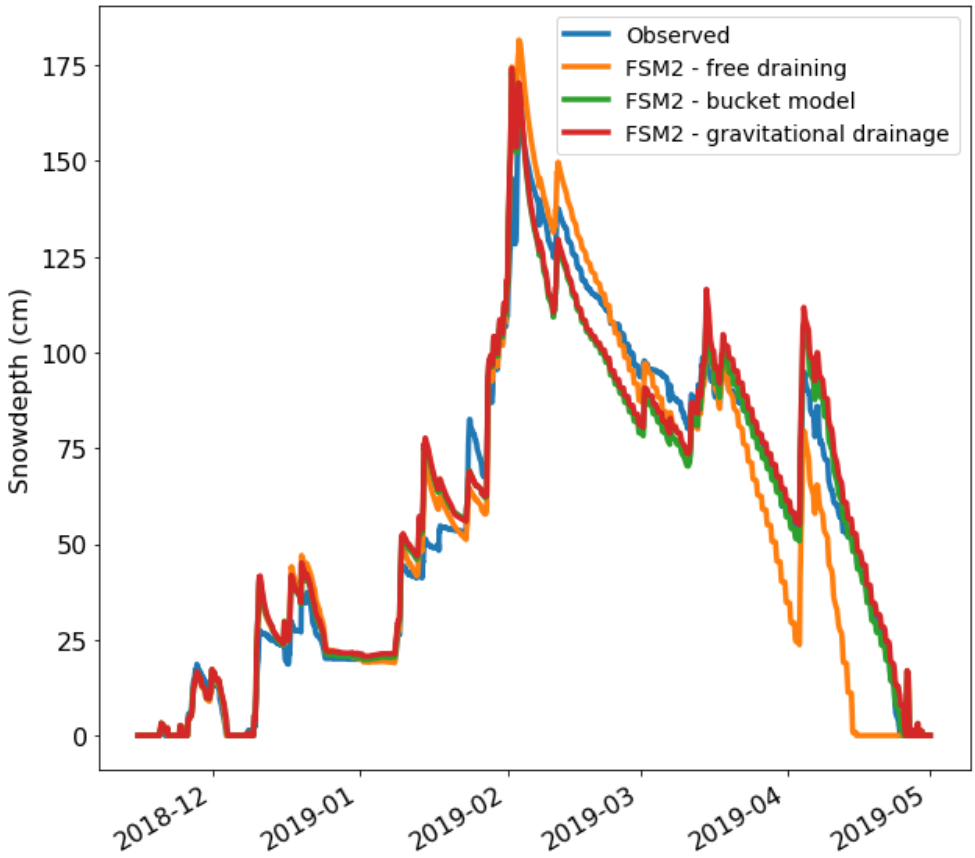


**Figure 5.11:** Measured and modelled snowdepth for the winter 2018-2019 season using three hydrology parametrisations, and density parametrised as a function of overburden.

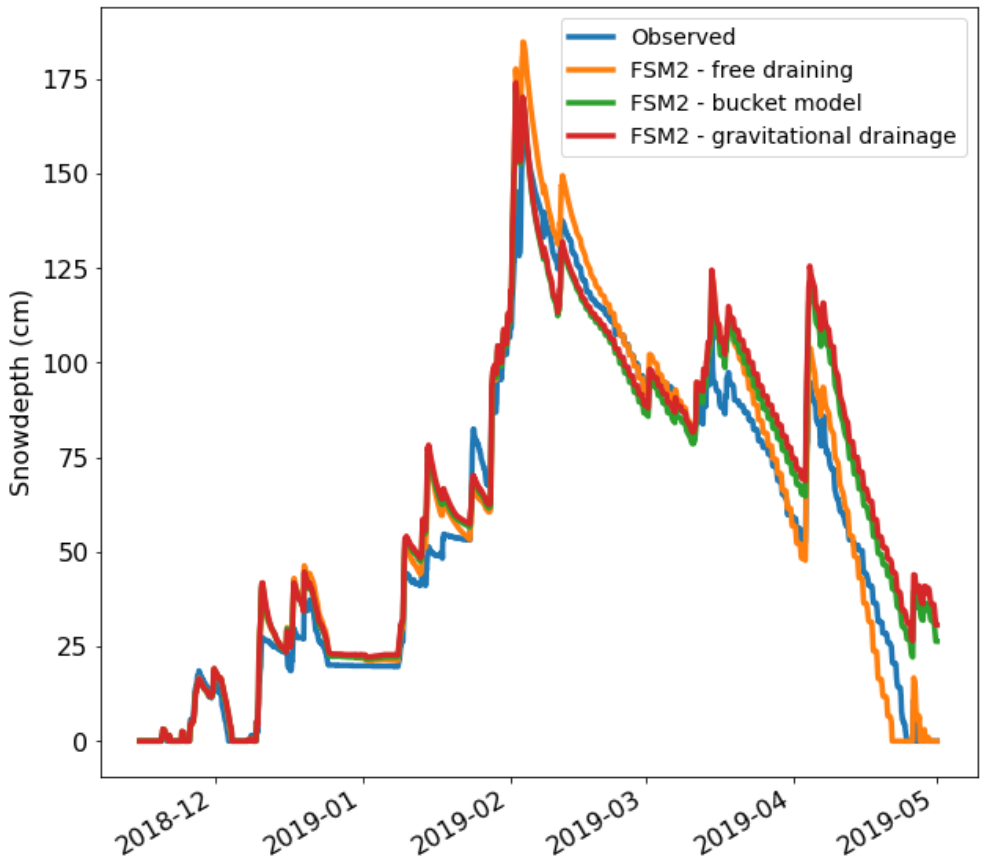


**Figure 5.12:** Measured and modelled snowdepth for the winter 2018-2019 season using three hydrology parametrisations, and density parametrised as a function of age.

### Parameter adjustment - irreducible water saturation

As noted above, the gravitational drainage model performed well when modelling both SWE and runoff, but runoff peaks were too narrow when compared to observations. To investigate whether some parameter adjustments improved FSM2's performance, the irreducible water saturation, $S_w$, was varied from its default model value of 0.03. Model performance statistics were calculated using the same evaluation data as above. The model was run with gravitational drainage hydrology, for both density parametrisations. $S_{ir}$ was varied from 0 to 0.07. Laboratory studies have found it most likely to lie between 0.02 - 0.07 (see section 1.3). When evaluated over long periods, density as a function of age performed better than density as a function of overburden for SWE simulations. This was true for all values of $S_{ir}$. The opposite was true for runoff predictions - density as a function of overburden performed best. Figures 5.13 and 5.14 show how the model performance varies with $S_{ir}$. SWE performance is best with $S_{ir} = 0.03$, whilst runoff performance is best when $S_{ir} = 0$. This is non-physical. This analysis confirms that the default choice of $S_{ir} = 0.03$ is a good compromise on performance and physical consistency.

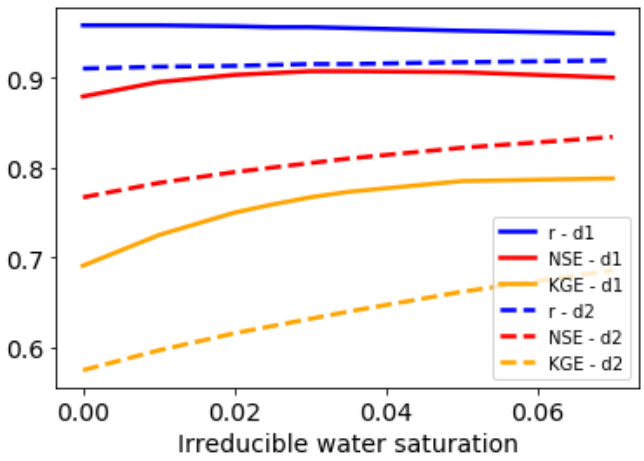


**Figure 5.13:** Model statistics for predicted SWE with varying $S_{ir}$. d1 = density function of age, d2 = function of overburden.

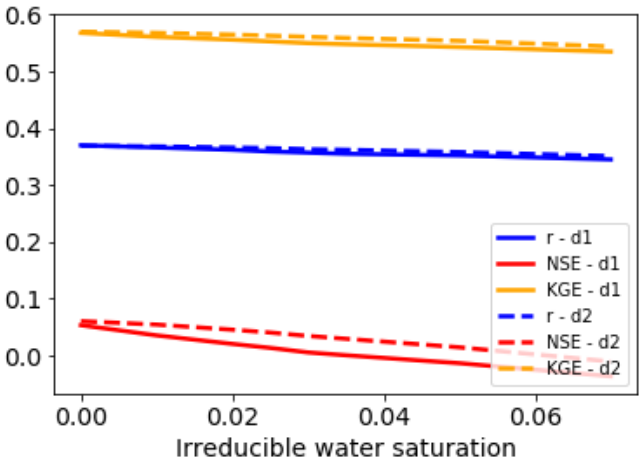


**Figure 5.14:** Model statistics for predicted runoff with varying $S_{ir}$. d1 = density function of age, d2 = function of overburden.

The performance of the model over shorter time periods with varying irreducible water saturation was also investigated, using two periods in spring 2019. This was carried out qualitatively, with the shape of the observed runoff curve compared to the modelled runoff to see which value of $S_{ir}$ and density parametrisation reproduced the shape best. Contrary to the model statistics outlined above, runoff was simulated best with density as a function of age when these short periods of runoff were compared. It can be seen in Figures 5.15 and 5.16 that the overburden model produced peaks that were too high, and the peaks began slightly earlier than the age model. However, it is clear that while the age density model reproduces the curves better, it still has peaks that are too narrow, and start too early when compared to observations. For much of the periods investigated for both density parametrisations there is not much variation between the shape of the curves with varying $S_{ir}$. However, when the runoff is small, which occurs on the 23rd March, and 7th and 8th April, there is a noticeable difference. With $S_{ir}$ set at 0.07, no runoff at all is generated at these times. With it set as 0.01, too much runoff is generated with both density parametrisations.

In conclusion, it appears from both the long period analysis of SWE and runoff, and the shorter period of qualitative analysis of runoff, that FSM2 performs best by taking a compromise value of $S_{ir} = 0.03$, which is the default value.

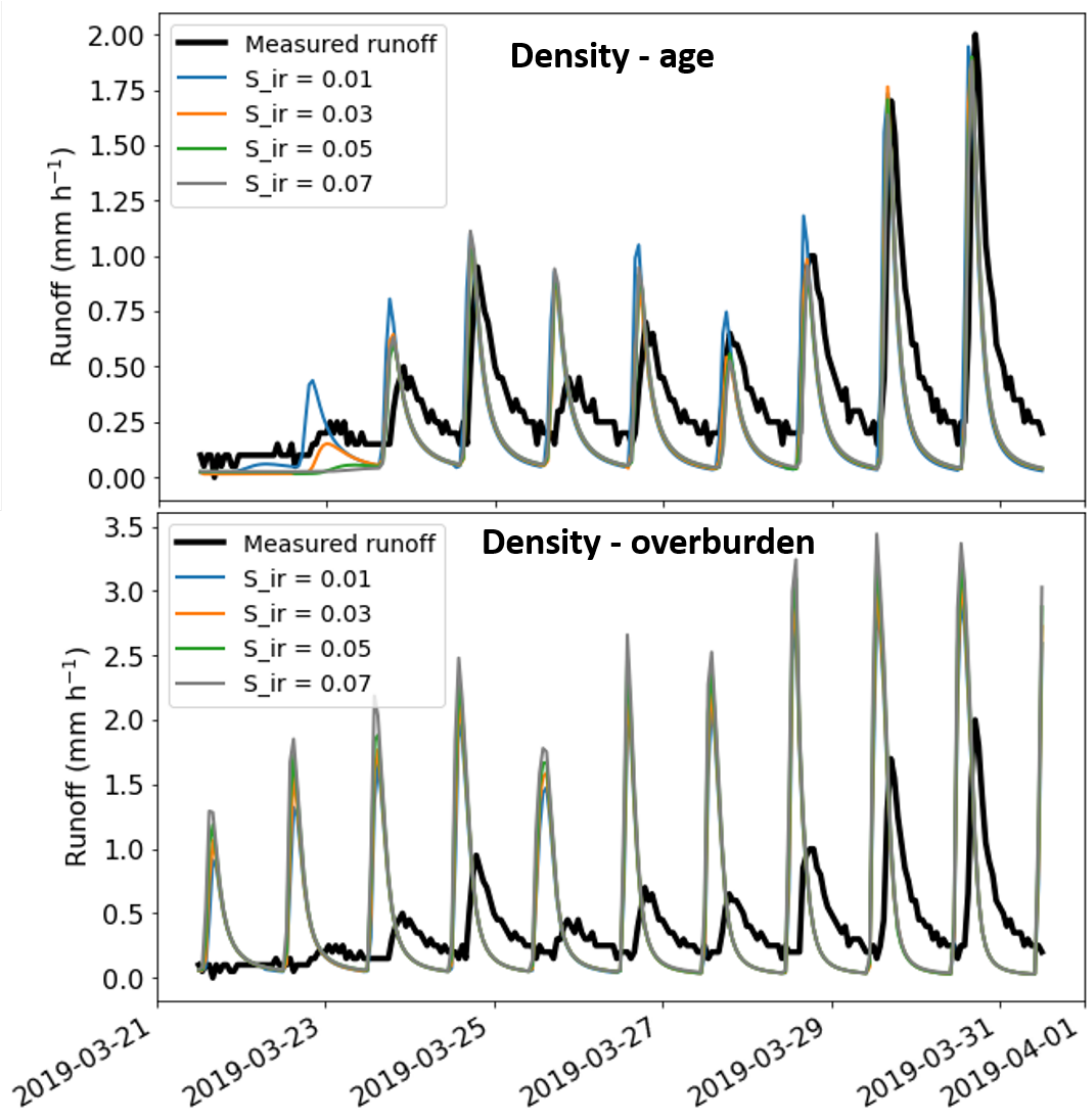


**Figure 5.15:** Modelled runoff for both density parametrisations and varying $S_{ir}$ for a period of diurnal melt in March 2019.

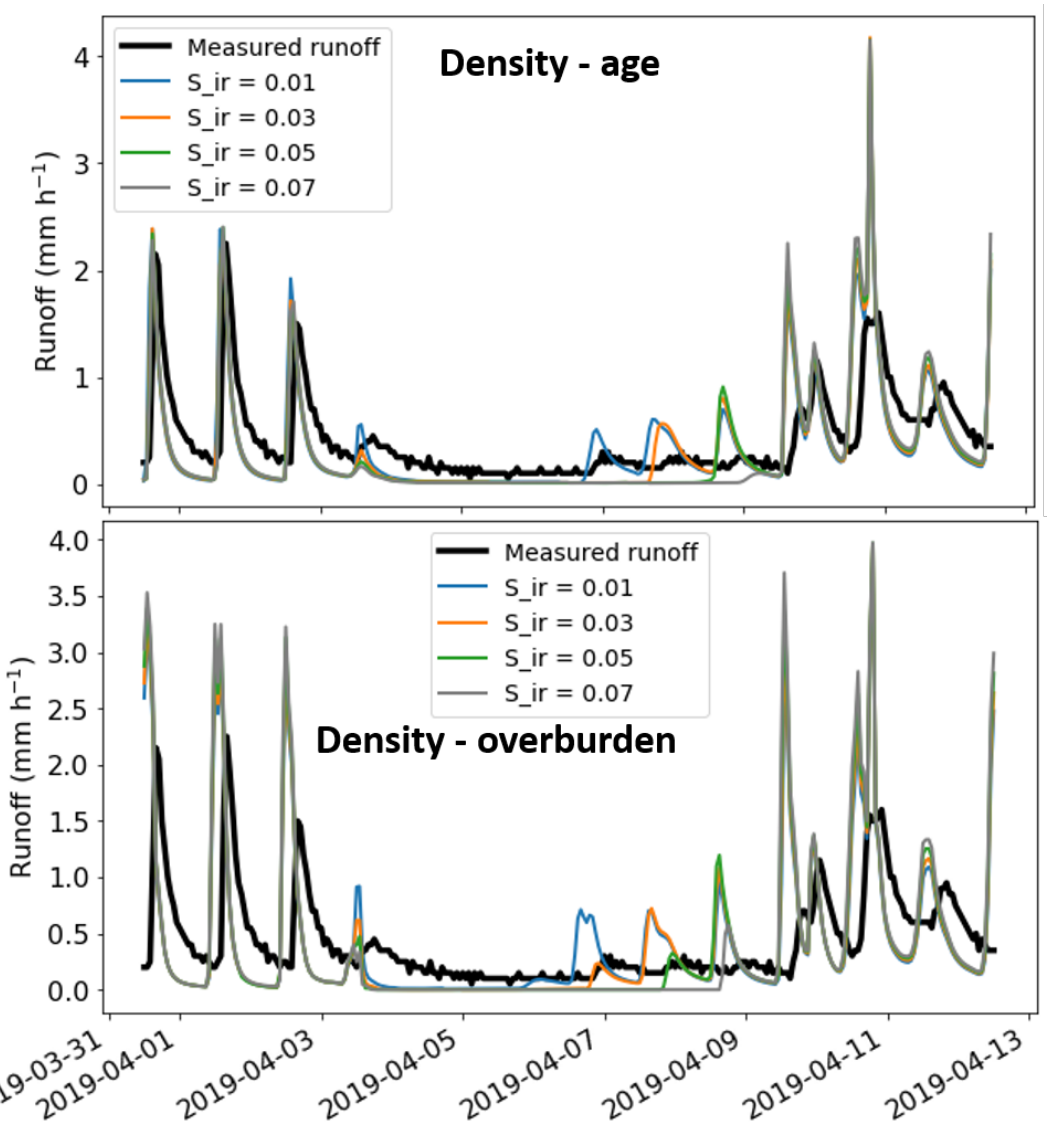


**Figure 5.16:** Modelled runoff for both density parametrisations and varying $S_{ir}$ for a period of including a rain-on-snow event in April 2019.

### Parameter adjustment - saturated hydraulic conductivity

Similarly to $S_{ir}$, the saturated hydraulic conductivity $k_{sat}$ was adjusted from the value parametrised in Equation 5.7 by multiplying by a factor. This was only relevant in the gravitational drainage model, and these adjustments were carried out for both density formulations. The aim of this adjustment was to improve the shape of the runoff curve by lengthening its 'tail'. By reducing the hydraulic conductivity of the snow, the speed of the water transport through the snow is reduced.

A long period statistical analysis was carried out, calculating model performance statistics over many years (the same as in section 5.3.5). This found that the differences in performance were tiny. The greatest change noted was two thousandths change in the correlation and Kling-Gupta Efficiency when halving the saturated hydraulic conductivity, so the full results are not displayed here for brevity.

As well as this long period analysis, a shorter period analysis was carried out (similar to 5.3.5), looking at the period of clear diurnal melting in March 2019. As might be expected from the tiny changes in model performance noted above, there were generally only small changes in the shape of the runoff curve. Because the changes were so small, looking over a number of days made the differences difficult to see, so Figures 5.17 and 5.18 are provided for just one 24 hour period. It can be seen that, as expected, reducing hydraulic conductivity does delay the runoff. The delay is small, and even halving the hydraulic conductivity to 0.5 of its default parametrised value still resulted in a runoff curve which tailed off too quickly, but there is an improvement in the shape.

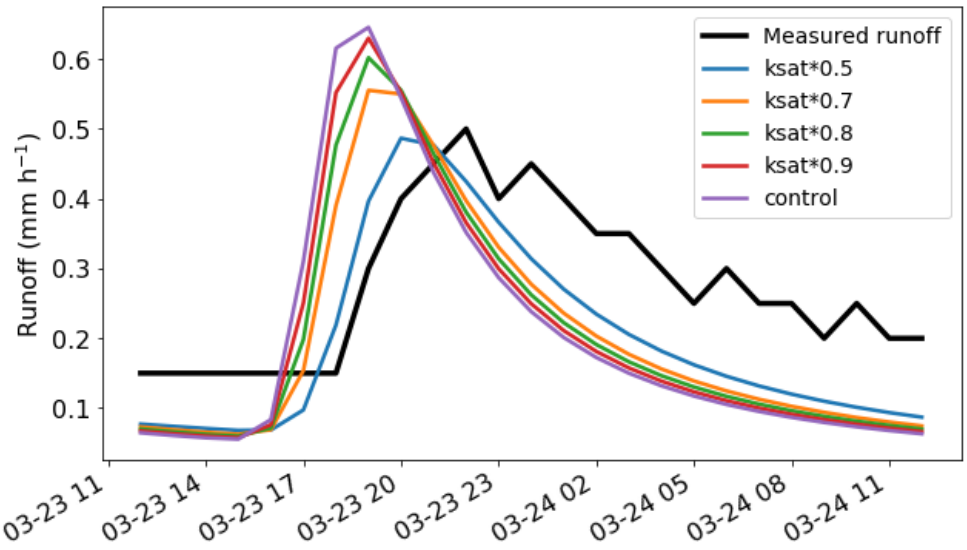


**Figure 5.17:** Modelled runoff with density as a function of age and varying saturated hydraulic conductivity ($k_{sat}$) for a 24 h period in March 2019.

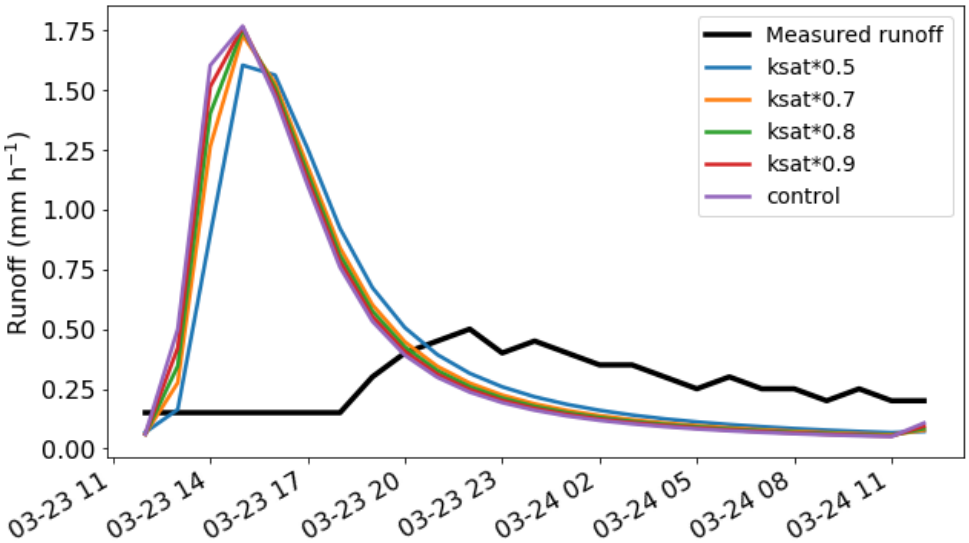


**Figure 5.18:** Modelled runoff with density as a function of overburden and varying saturated hydraulic conductivity ($k_{sat}$) for a 24 h period in March 2019.

## 5.4 Distributed modelling

### 5.4.1 Introduction

As well as evaluating the performance of the snow hydrology model at a point location, it is useful to assess how well it can perform over a larger area such as a river catchment or mountain range. Many operational uses for snow models require information over an area, such as flood or avalanche hazard prediction. As such, FSM2 was used to model snow cover over the area of the Alps in which Col de Porte is situated.

### 5.4.2 Driving data

FSM2 was driven with numerical weather prediction data from the French operational high resolution weather forecast model AROME (**A**pplication of **R**esearch to **O**perations at **ME**soscale). It provides forecast meteorological data at hourly temporal resolution, on a 1.3 km grid over continental France. A subset of the full dataset which covered the Chartreuse mountains (the location of Col de Porte) was used for the three winters beginning in 2017, 2018 and 2019.

### 5.4.3 Ancillary data

To run the model, information about the land surface is required. This was taken from the ECOCLIMAP 1 km global database of surface parameters (Masson et al., 2003). This provides forest fraction, snow-free albedo and monthly vegetation area index (VAI).

### 5.4.4 Evaluation data

To evaluate the performance of FSM2 as a distributed model, two strategies were employed. Firstly, the model was evaluated at Col de Porte, then the model was evaluated over the Chartreuse Alps domain.

To evaluate at Col de Porte, output driven with AROME for the model grid point closest to Col de Porte was extracted. This was compared to Col de Porte observations, FSM2 run with observed in situ data, and FSM2 driven with the SAFRAN dataset. SAFRAN (Système d'Analyse Fournissant des Renseignements Adaptés à la Nivologie) (Durand et al., 1993) is a reanalysis tool used operationally to create snow model driving data to drive the French operational avalanche forecasting models. It divides the domain of interest into climatologically relatively homogeneous areas, taking account of elevation, slope and aspect. It uses all available manual and automatic meteorological observations in the given area and complements them with numerical weather prediction data from AROME to create a driving dataset.

To evaluate over the Chartreuse domain, remotely sensed snow cover fraction from European Space Agency using the MODIS Terra satellite (Nagler et al., 2021) was used to evaluate the performance over the whole model domain covering the Chartreuse Alps.

### 5.4.5 Meteorological data uncertainty

As found by Günther et al. (2019), forcing data is the largest source of hydrological model uncertainty. This means that a large factor in the success (or otherwise) of FSM2 running over the Chartreuse Alps will be due to uncertainty in the AROME forcing data. A full evaluation of the meteorological data over the whole model domain is beyond the scope of this work, but by comparing FSM2 run using in situ and AROME data the uncertainty will be evaluated at Col de Porte.

### 5.4.6 FSM2 distributed configurations

Running FSM2 in a distributed framework allows the same flexibility with model parameters as afforded for single-site runs. Therefore it was possible to run and evaluate FSM2 for the three hydrology and the two density parametrisations. The model was used with its default three layer set up, and physical parameters set as their default values. In addition to the density and hydrology parametrisations, when modelling over a large area, the effect of snow cover

fraction becomes more important. FSM2 has two snow fraction options. Option 1 is snow cover fraction as a linear function of snow depth:

$$fsnow = \min\left(\frac{snd}{hfsn}, 1\right) \tag{5.9}$$

where $snd$ is the snow depth, and $hfsn$ is the snow cover fraction depth scale (0.1 m). Option 2 is snow cover as an asymptotic function of snow depth:

$$fsnow = \frac{snd}{snd + hfsn} \tag{5.10}$$

### 5.4.7 Col de Porte results

#### Driving data evaluation at Col de Porte

Before running the model, the two meteorological datasets (SAFRAN and AROME) were compared with observations. The SAFRAN gridpoint was at 1325 m, with an aspect of 10 degrees (from North), and a slope of 0 i.e. it is flat. The AROME dataset does not take account of aspect or slope. The altitude of the centre of the nearest gridbox is 1342 m, 600 m horizontally away from Col de Porte observatory.

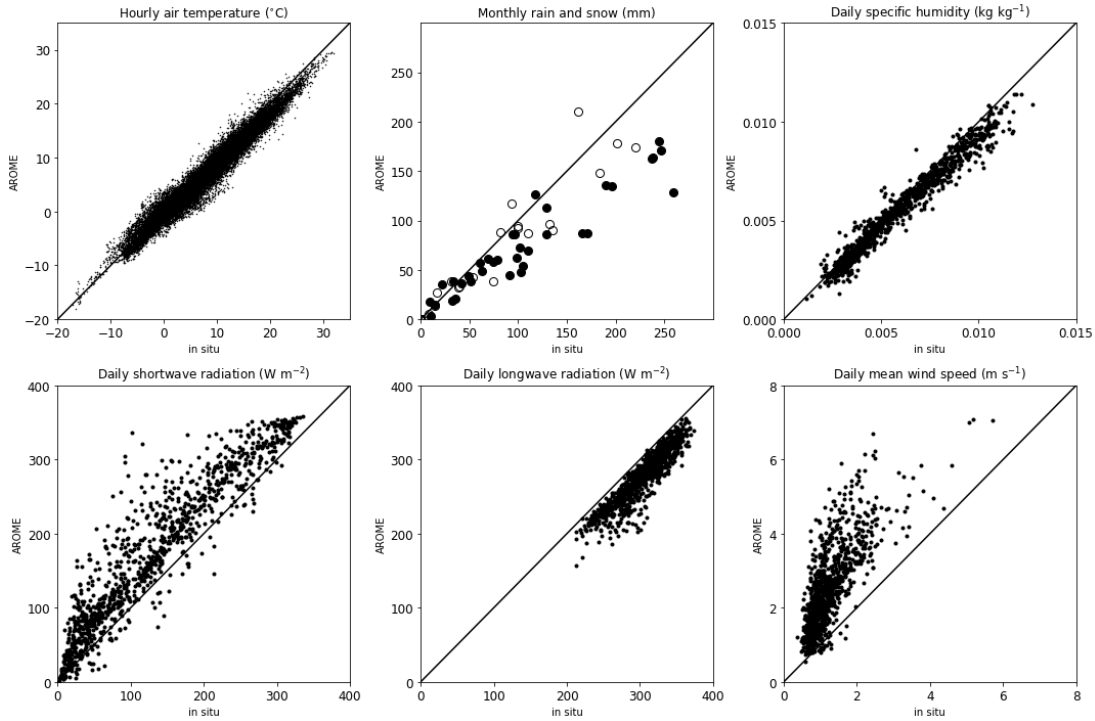


**Figure 5.19:** Scatterplots of AROME meteorological data against in situ observations for 2017 - 2020. In precipitation figure, closed circles represent rain, and open circles snow.

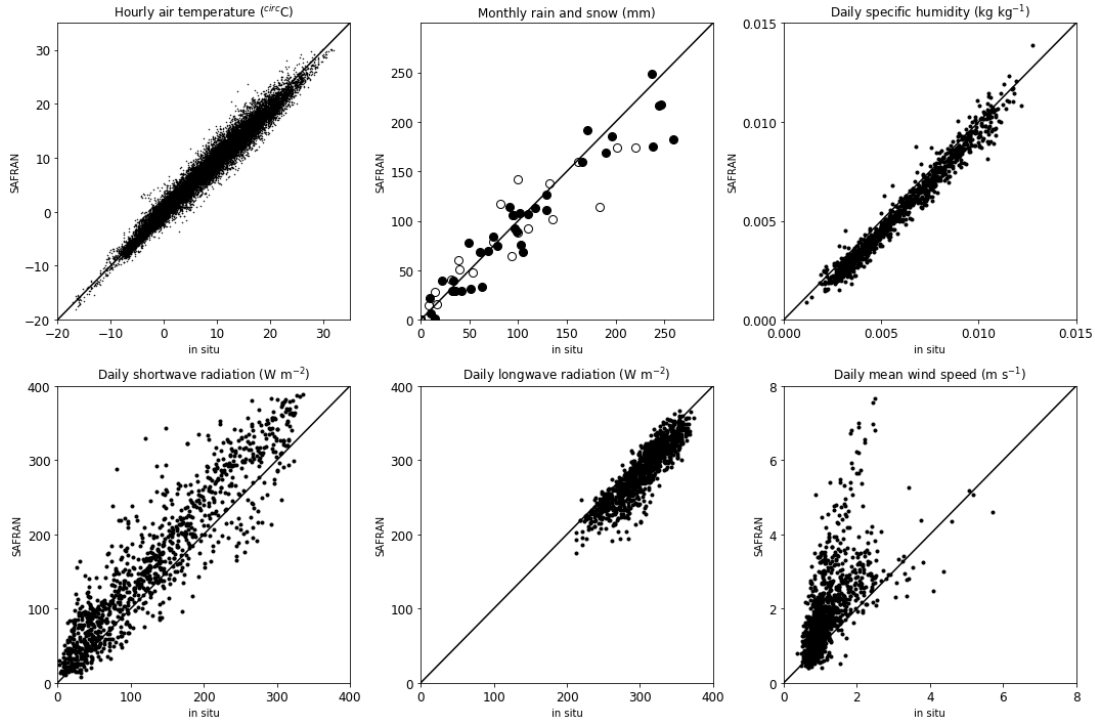


**Figure 5.20:** Scatterplots of SAFRAN meteorological data against in situ observations for 2017 - 2020. In precipitation figure, closed circles represent rain, and open circles snow.

Looking at Figures 5.19 and 5.20 it is clear that for most variables, there is generally excellent agreement between observations and the two driving datasets. Some variables show some bias though. Both datasets underestimate precipitation to an extent, especially for months with higher precipitation, suggesting the modelled data do not capture extremes well. AROME underestimates by a larger amount in general, especially for snowfall.

AROME and SAFRAN both overestimate total shortwave radiation, and both underestimate longwave radiation. Wind speeds are overestimated to a similar degree by both SAFRAN and AROME.

Looking at precipitation accumulations over the three year period from 2017 - 2020 (Figure 5.21), it is clear that both SAFRAN and AROME underestimate the precipitation totals. The differences between observations are smaller for snow, while the largest difference is between observations and AROME rainfall.

Looking at weekly maximum and minimum temperatures, on average there is very little bias for minimum temperatures, although clearly for both SAFRAN and AROME this masks a lot of variation. For maximum temperatures, both AROME and SAFRAN show a positive bias i.e. they are both too warm. On average, AROME is about 2°C too warm, and SAFRAN is about 1°C too warm, although there is of course variation masked by the averaging.

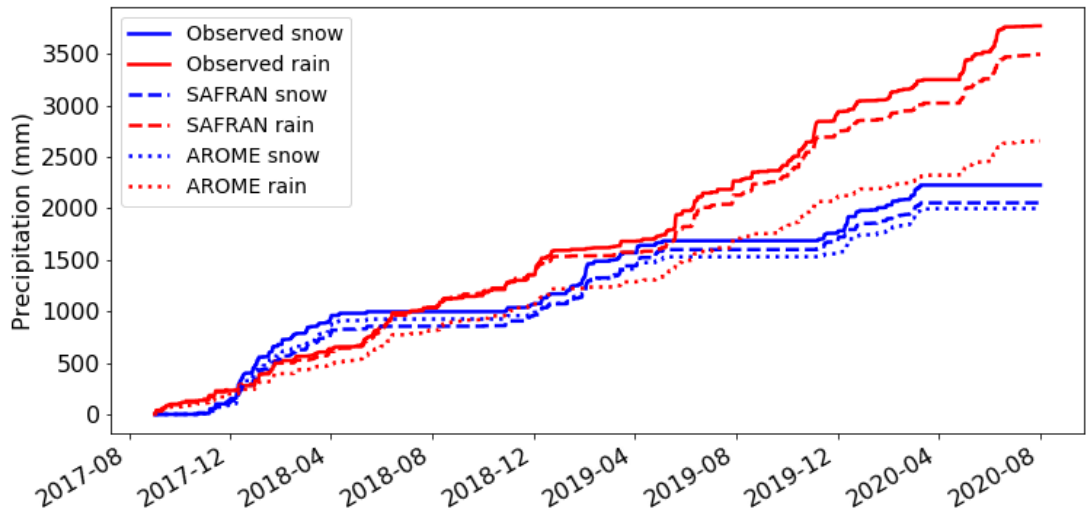


**Figure 5.21:** Accumulated snow (blue) and rain (red) for in situ, SAFRAN and AROME datasets.

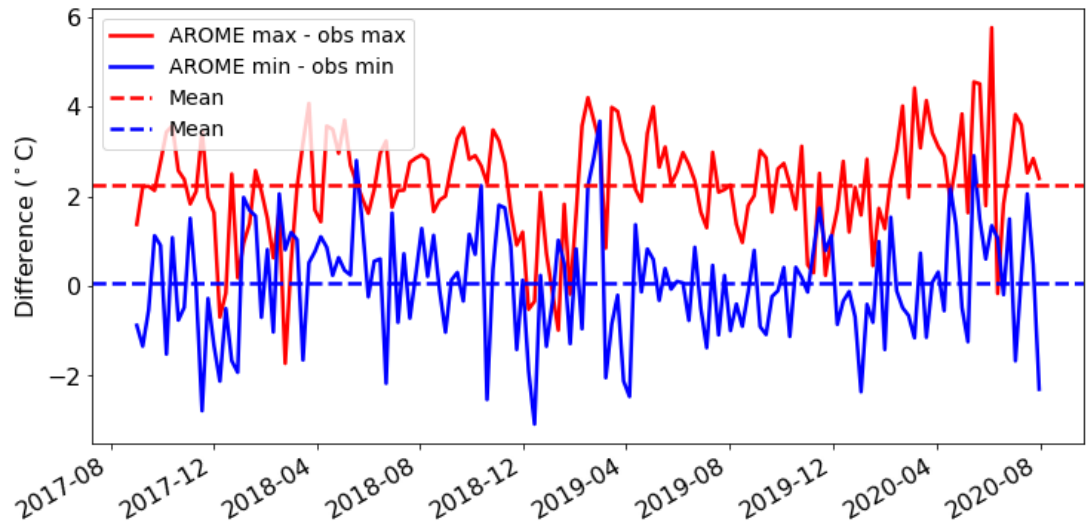


**Figure 5.22:** 2017 - 2020 differences between weekly maximum and minimum observed and AROME air temperature, and mean difference for maximum and minimum as horizontal dashed lines.

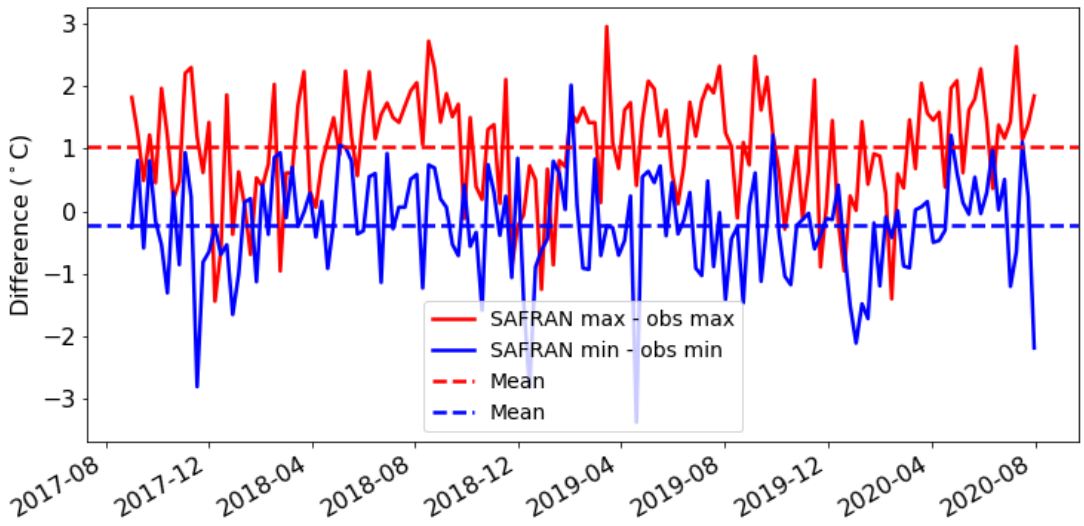


**Figure 5.23:** 2017 - 2020 differences between weekly maximum and minimum observed and SAFRAN air temperature, and mean difference for maximum and minimum as horizontal dashed lines.

### Runoff

Since FSM2 generally performed best with the hydrology modelled as gravitational drainage, this setting was used to investigate the runoff performance of the three different model driving datasets at Col de Porte. Two density parametrisations were evaluated: as a function of age (d1) and as a function of overburden (d2). First, daily observed runoff totals were compared with modelled totals derived from the three driving datasets. Figure 5.24 shows scatter plots of this comparison. It is difficult to differentiate between the two density parametrisations.

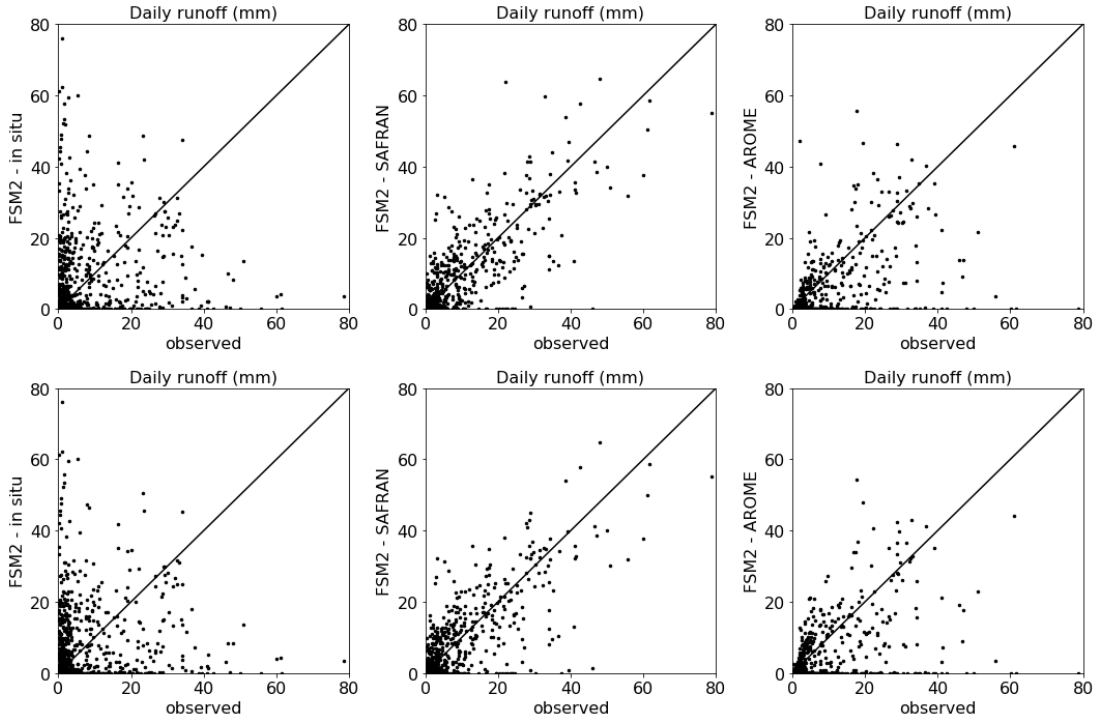


**Figure 5.24:** Observed daily runoff plotted against FSM2 forced with in situ, SAFRAN and AROME data. The top row uses density as a function of age (d1), the bottom row uses density as a function of overburden (d2).

Figure 5.25 shows the difference between the modelled and observed runoff for the three datasets. The difference in model performance between the two density parametrisations is very small. Differences between the three driving datasets are apparent though. For both density formulations, the in situ observations have the lowest mean error, but somewhat surprisingly have the highest standard deviation. The purely numerical weather prediction based AROME dataset has the highest mean error, but a standard deviation lower than the in situ observations. The SAFRAN dataset lies between the two, showing the value of a blend of numerical weather prediction and observed data.

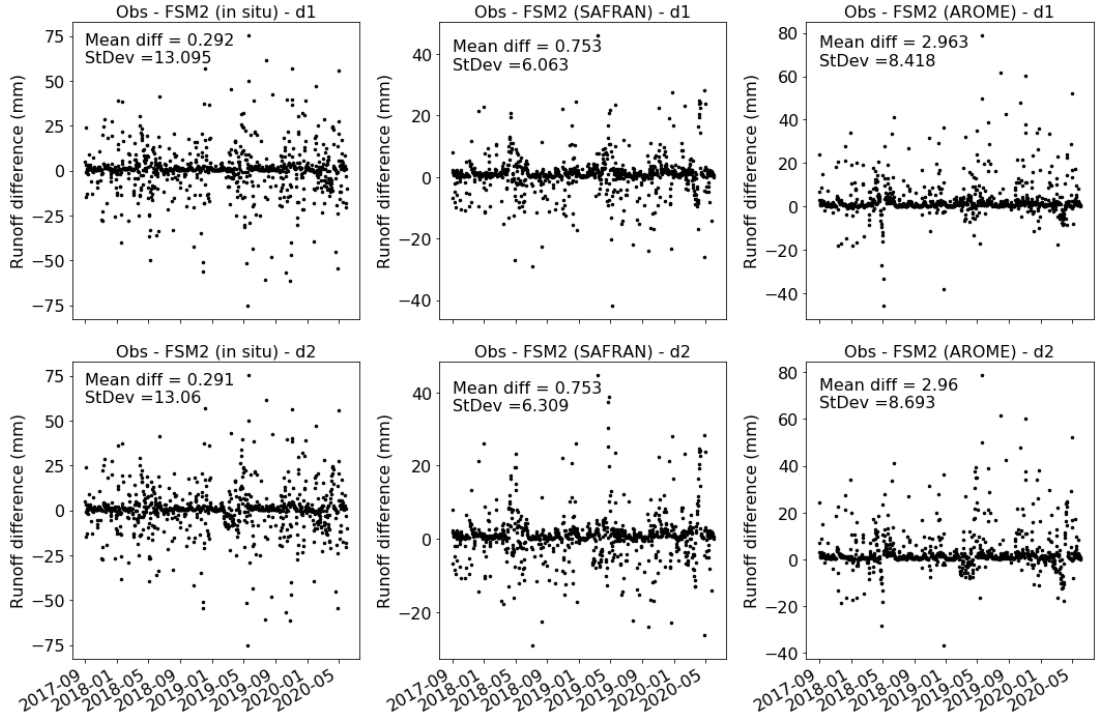


**Figure 5.25:** Observed daily runoff - modelled runoff. Mean and standard deviation are shown for each plot. The top row uses density as a function of age (d1), the bottom row uses density as a function of overburden (d2).

To see whether errors grow through the snow season, cumulative modelled runoff was plotted alongside cumulative observed runoff. Figure 5.26 shows this with density as a function of age (Figure A.6 in appendix A shows the same plot with density as a function of overburden). FSM2 driven with SAFRAN and in situ data follows the observations most closely. The difference between SAFRAN and observations is slightly larger than with in situ. AROME consistently underestimates runoff, resulting in a large difference by the end of the period. This makes sense given that AROME underestimates precipitation (see Figure 5.21), especially rainfall.

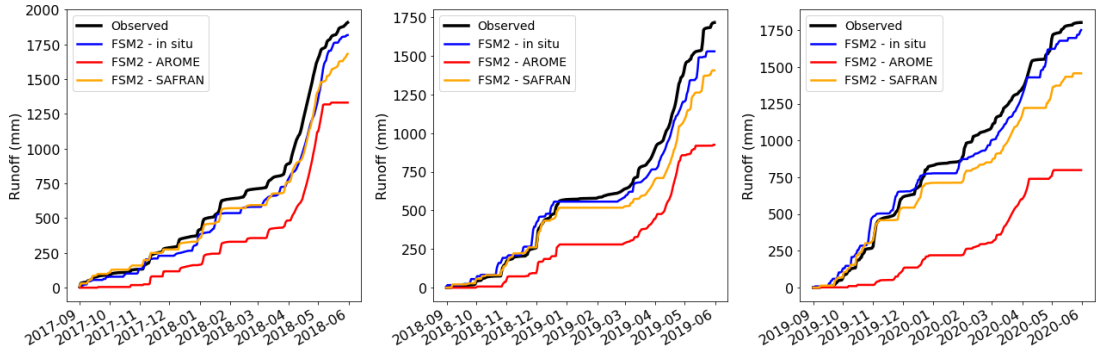


**Figure 5.26:** Cumulative runoff for 2017 - 2020 at Col de Porte with density modelled as a function of snow age.

### SWE

To evaluate the model driving dataset performance at predicting SWE, modelled SWE was compared to observed daily SWE from cosmic ray sensors located at Col de Porte.

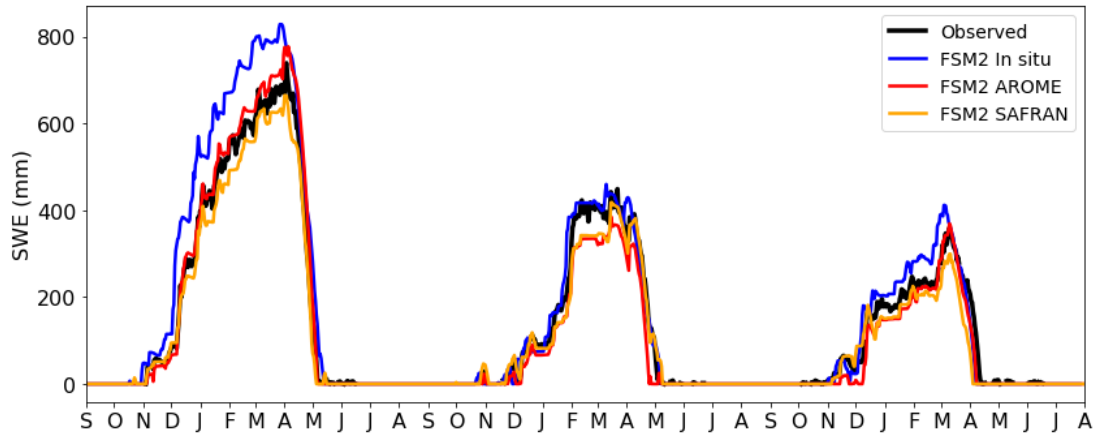


**Figure 5.27:** Observed and modelled SWE for 2017 - 2020 at Col de Porte with density modelled as a function of snow age.

In the model evaluations earlier in this chapter, it was found that SWE was predicted better using density modelled as a function of age than as a function of overburden. This is still true when using these different model driving datasets to an extent, although there is variation in which driving dataset performs best each year, as can be seen in Figures 5.27 and 5.28.

To more clearly see the difference between each model's performance, and between the two density parametrisations, the differences are plotted in Figures 5.29 and 5.30. Generally, the differences are smaller with density as a function of age as expected, although the variation from year to year is clear as before.

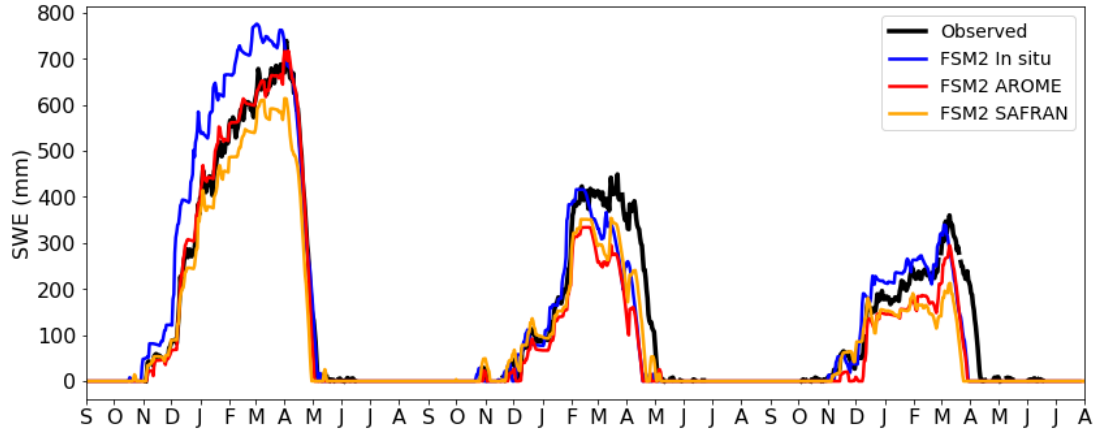


**Figure 5.28:** Observed and modelled SWE for 2017 - 2020 at Col de Porte with density modelled as a function of snow overburden.

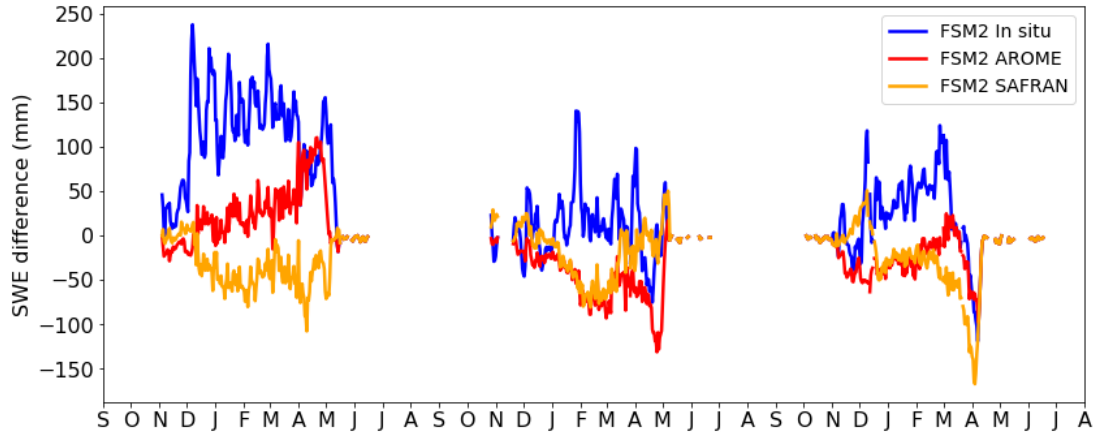


**Figure 5.29:** Difference between modelled and observed SWE for 2017 - 2020 at Col de Porte with density modelled as a function of snow age.

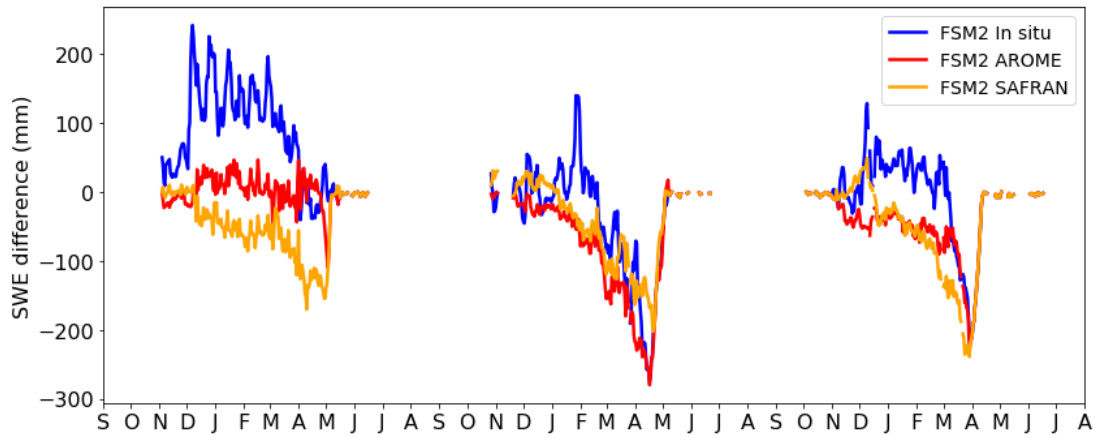


**Figure 5.30:** Difference between modelled and observed SWE for 2017 - 2020 at Col de Porte with density modelled as a function of snow overburden.

### 5.4.8 Chartreuse snow cover results

To evaluate FSM2's performance over the Chartreuse area, mean snow-covered fraction was calculated over the model domain, and compared with the remotely-sensed mean snow cover fraction measured by the ESA snow cover remotely-sensed data. This is only available for days when there was little or no cloud cover, so it is not possible to compare throughout the entire period. FSM2 was run over the domain with density modelled as either a function of overburden, and a function of age. Snow-covered fraction of the grid box was diagnosed as either a linear function of snowdepth, or as an asymptotic function of snowdepth.

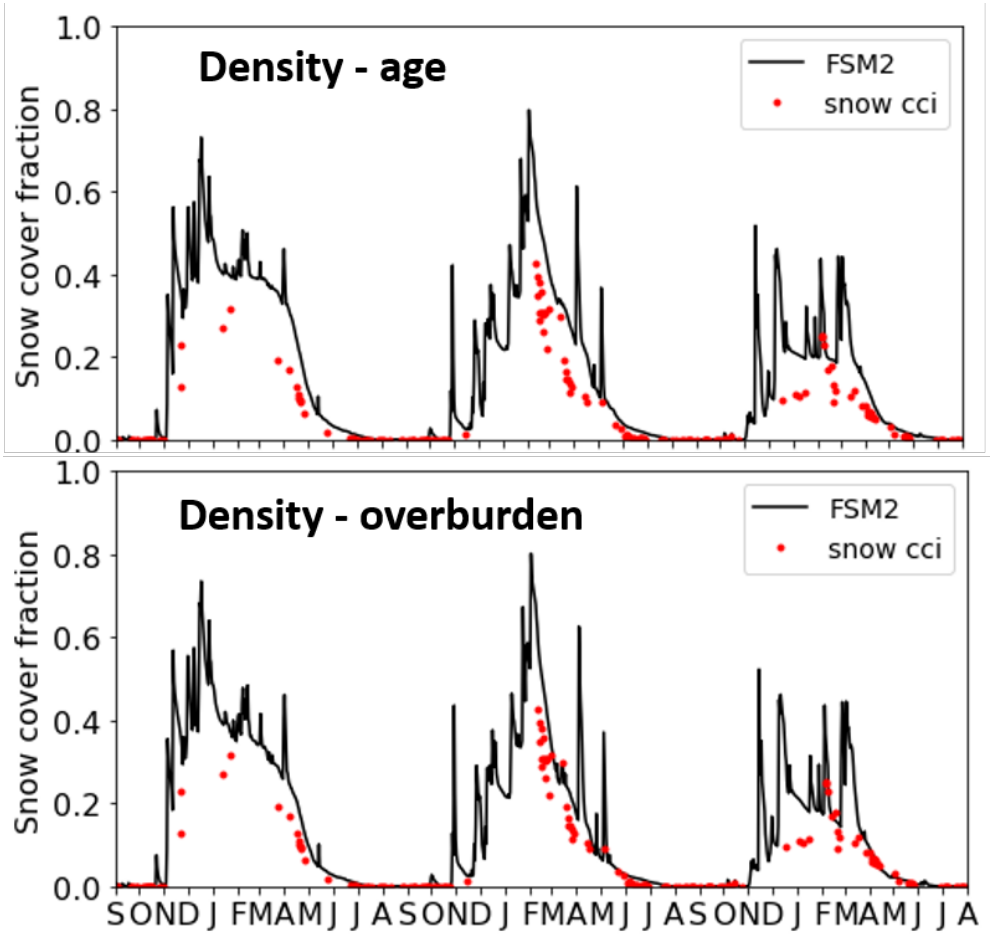


**Figure 5.31:** Mean snow cover fraction over the Chartreuse domain FSM2 driven with AROME for 2017 - 2020, compared with ESA cci data when cloud cover permits. Snow cover fraction parametrised as a linear function of snow depth.

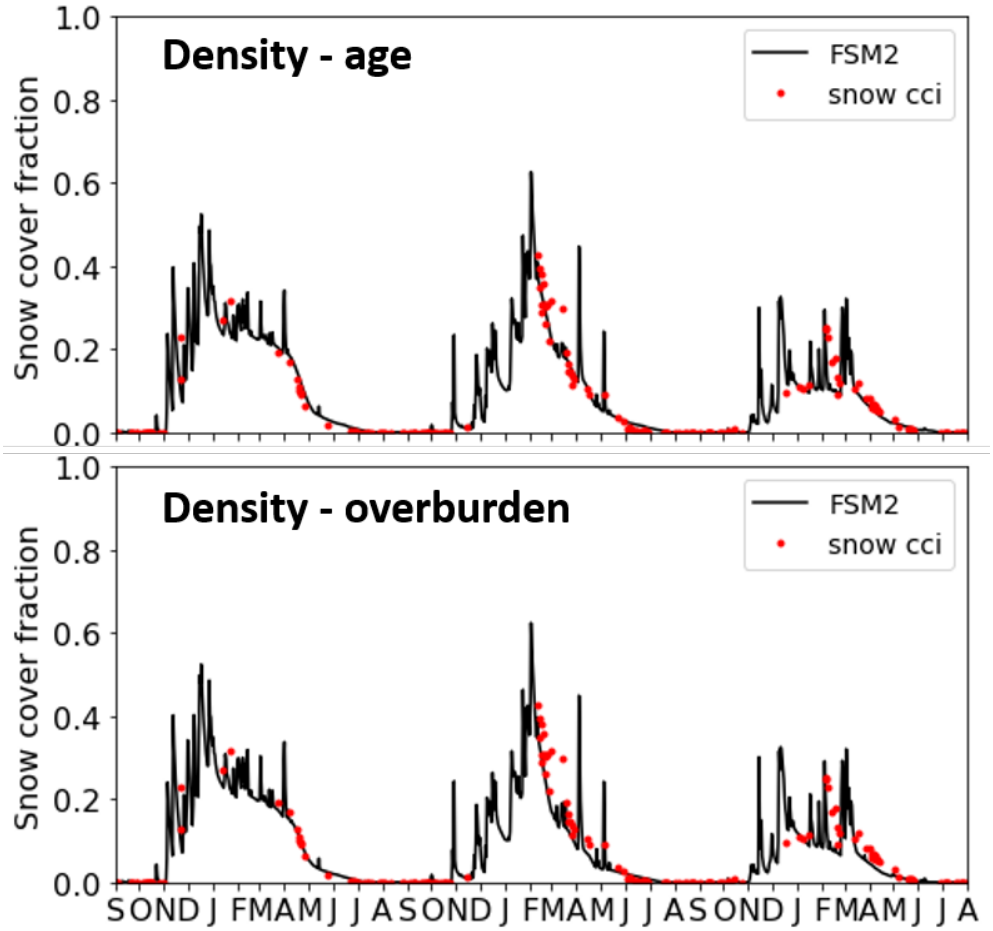


**Figure 5.32:** Mean snow cover fraction over the Chartreuse domain FSM2 driven with AROME for 2017 - 2020, compared with ESA cci data when cloud cover permits. Snow cover fraction parametrised as an asymptotic function of snow depth.

It can be seen in Figures 5.31 and 5.32 that the different density parametrisations have a fairly small effect when verifying with the remotely sensed data. There is a slightly clearer change when snow fraction is parametrised as a linear function of snow depth, especially in 2017 and 2018. There is a larger difference between the two snow fraction parametrisations. Snow fraction as an asymptotic function of snow depth verifies best against the remotely sensed data.

As well as evaluating the average model performance over the domain for the three winters, the model was evaluated on some individual days when a clear satellite image was available. The best performing model configuration from above was chosen as a ‘reference’ model, from which other model configurations were subtracted to produce difference plots. The reference configuration chosen was: density as a function of age, gravitational drainage hydrology, and snow cover fraction as an asymptotic function of snow depth. The model domain topography is shown in Figure 5.33 to help interpret the snow cover maps.

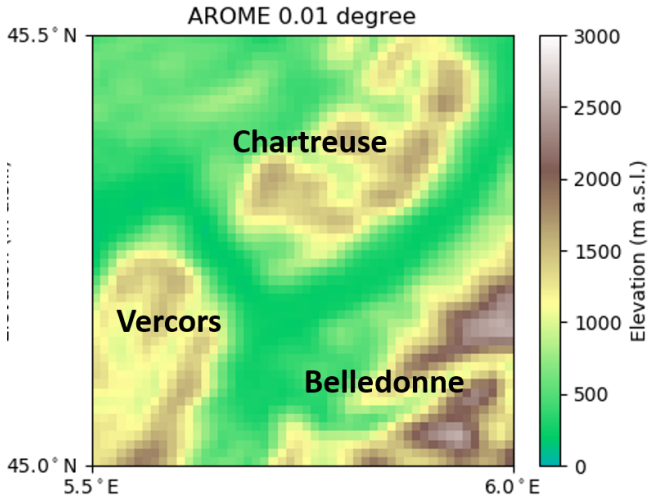


**Figure 5.33:** Model domain topography.

Figure 5.34 shows this reference run plotted on 15th February 2019, a day with a clear view and a lot of snow cover. Over most of the mountainous ground, FSM2 verifies well compared to the satellite data. Areas of difference are chiefly on steep and forested terrain, although there is an area of clear snow cover missed on the high ground to the north of the main Chartreuse range at about 45.4°N. FSM2 also underdoes a reasonably large area of snow cover in the Vercors range at about 45.1°N 5.6°E. Another cloud-free day is available in appendix C.

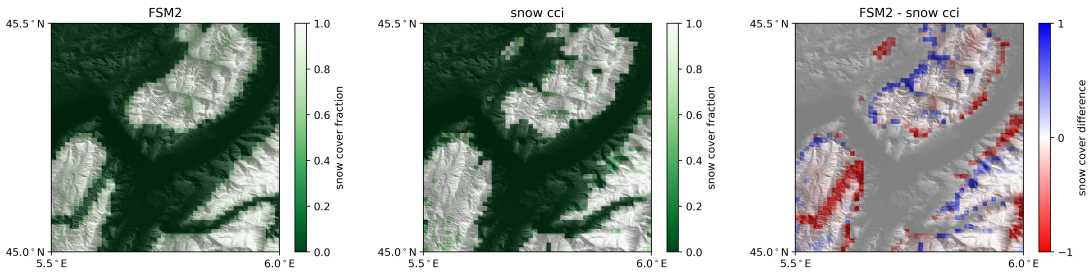


**Figure 5.34:** 'Reference' FSM2 modelled, observed and model-observation difference in snow cover fraction on 15th February 2019 over Chartreuse domain.

To evaluate other model configurations, differences between alternative configurations and the 'reference' model were calculated and plotted for the same day as above (15th February 2019) (Figures 5.35 and 5.37). Figures from another day are available in appendix C.

There is very little difference between the bucket model snow cover fraction and the reference model. The free draining model has more snow cover than the reference model around some of the steeper but lower altitude slopes on most aspects in all three main ranges in the domain, and also some of the central parts of the Vercors plateau. A similar pattern is visible on 24th January 2018 (appendix C).

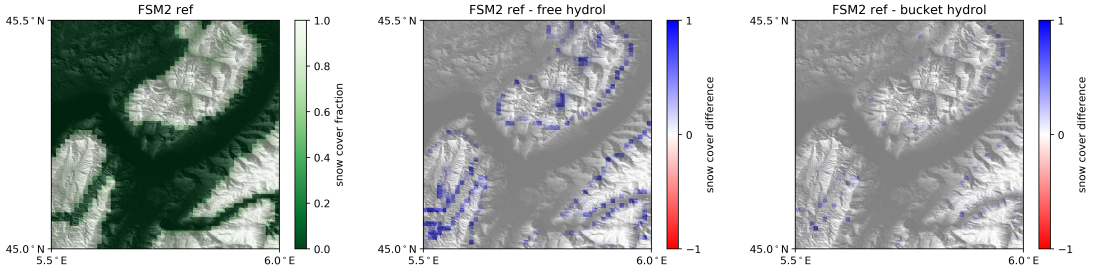


**Figure 5.35:** 'Reference' FSM2 compared with free draining and bucket hydrology models on 15th February 2019 over Chartreuse domain.

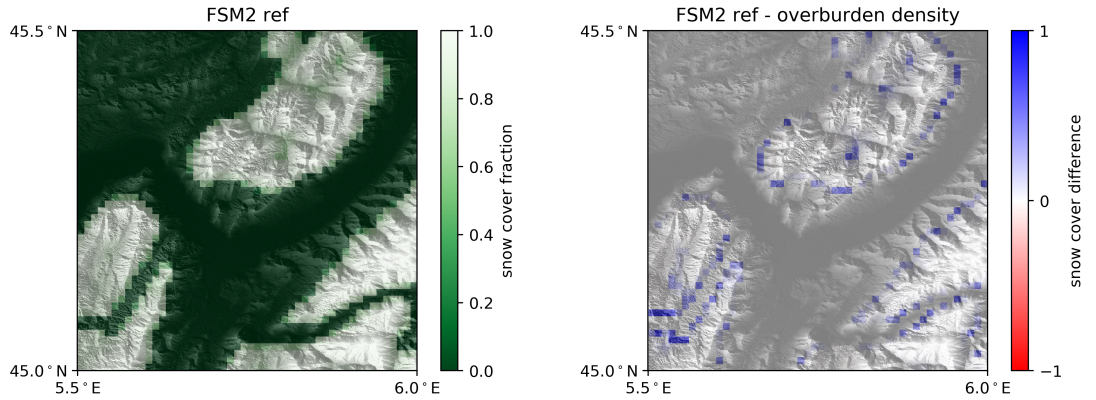


**Figure 5.36:** 'Reference' FSM2 compared with density as a function of overburden model on 15th February 2019 over Chartreuse domain.

The difference in modelled snow cover between the two density models is fairly small. The main differences are that the overburden model produces more snow cover around some of the lower and steeper slopes, and also in the central Vercors. There is less difference in January 2018 (appendix C).

The difference between the reference model run and modelling snow cover fraction of each grid box as a linear function of snow depth is larger than any of the other parameters compared. The linear function has less snow than the reference model over most of the lower slopes of the three mountain ranges in the domain, and also some of the central Vercors plateau. In January 2018 the pattern is similar, but not as marked as there is less snow cover in general (C).

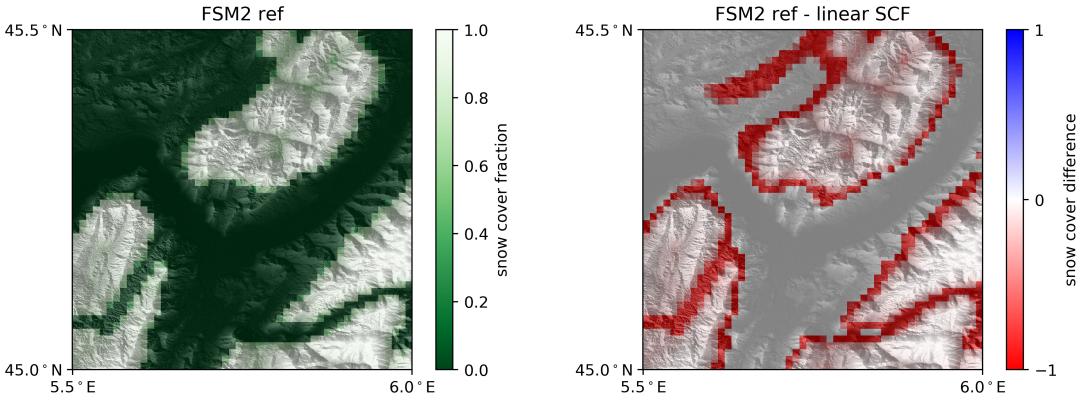


**Figure 5.37:** 'Reference' FSM2 compared with snow cover fraction as a linear function of snow depth on 15th February 2019 over Chartreuse domain.

### 5.4.9 Distributed modelling summary

In summary, running FSM2 as a distributed model over the whole Chartreuse Alps using high resolution numerical weather prediction (NWP) data verify well with both available satellite products, and in situ measurements at one mid-elevation site. It appears that most of the model uncertainty stems from driving data uncertainties, as when the model is evaluated at a site with in situ data the errors are small compared to the model run with NWP driving data. The best model configuration, based on the partial evaluation carried above, is similar to the best performing model for site specific uses found earlier in this thesis: gravitational drainage and density as a function of age perform well. For the site specific simulation at Col de Porte, the snow cover fraction option did not make much difference, but when evaluated over the whole domain, snow cover as an asymptotic function of snow depth performed best.

## 5.5 Modelling electrical processes in snow

In order to evaluate the possibility of using geophysical measurements to improve modelling of liquid water in the snowpack, it was necessary to develop a coupled electrical-snow model.

### 5.5.1 Theory of electrical self potential in snow

The magnitude of the self-potential signal is related to several properties of the snow itself, and of the meltwater percolating through it. This is described in detail in Kulessa et al. (2012) and Thompson et al. (2016). The flux of meltwater is the most intuitive influence on the SP, but the snow grain size, meltwater chemistry, liquid water content and snow density all have an effect on the size of signal to be measured.

For this model case, thermal contrasts are assumed to be small, because if the snowpack is able to support the movement of liquid water, it must be isothermal at 0°C. Similarly, chemical differences are assumed to be relatively small due to the snowpack being mature with preferential elution of ions having already taken place. This means that changes in the conductivity and pH of the snowpack will have already occurred, and these properties can be assumed to be approximately constant over the time covered by the model experiments. Therefore, the dominant source of potentials in the snow will be streaming potentials caused by the movement of meltwater through the snow. These modelled potentials were expected to be of the order of 10s to 100s of millivolts, as measured in Thompson et al. (2016) and Clayton (2021), and in chapter 4.

### 5.5.2 Self potential model

The bulk electrical conductivity of a porous material, $\sigma$, is given by:

$$\sigma = \frac{1}{F} S_w^n \sigma_w \tag{5.11}$$

where $F$ is the (intrinsic) formation factor, $\sigma_w$ is the electrical conductivity of the pore water, $S_w$ is the relative saturation and $n$ is the effective saturation exponent. Without direct evidence, $n \approx 3.3$ was used as in Albert and Krajeski (1998).

The source current density is related to the relative saturation $S_w$ and to the excess of charge, $\bar{Q}_v$ (in C m$^{-3}$) existing in the water, by (Revil et al., 2007):

$$\mathbf{j_s} = \frac{\bar{\mathbf{Q}}_\mathbf{v}}{\mathbf{S_w}} \mathbf{u} \tag{5.12}$$

where $\mathbf{u} = \mathbf{QA^{-1}}$ is the Darcy velocity (in m s$^{-1}$), $Q$ is discharge (m$^3$ s$^{-1}$) and $A$ is cross-sectional area (m$^2$).

The Poisson equation relates the electrical field $\psi$ to the source current density (j$_s$, in A m$^{-2}$) in a partially or fully saturated snowpack:

$$\nabla \cdot (\sigma \nabla \psi) = \nabla \cdot \mathbf{j_s} \tag{5.13}$$

where $\sigma$ is the electrical conductivity of the snow (in S m$^{-1}$ ). Equation 5.13 only applies in the low-frequency limit of Maxwell's equations if there is no external injection or removal of charge, or charge storage in the snowpack. This therefore applies to our passive monitoring case as no current is injected.

Equation 5.13 can be solved using the Helmholtz-Smoluchowski theory for unsaturated flow, by adapting Guichet et al. (2003) to get a 1-dimensional solution:

$$\psi_m - \psi_0 = -\frac{\varepsilon\zeta}{\eta\sigma_W} S_W (H_m - H_0) \tag{5.14}$$

where $\psi_m$ and $H_m$ are the electrical and hydraulic potentials at the measurement electrode, $\psi_0$ and $H_0$ are the corresponding potentials at the reference electrode, $\zeta$ is the zeta potential (V), and $\varepsilon$, $\eta$, $\sigma_w$ and $S_w$ are the dielectric permittivity (F $m^{-1}$), dynamic viscosity (Pa s), electrical conductivity (S $m^{-1}$ ) and relative saturation (dimensionless) of the meltwater in the snow's pore space. The zeta potential ($\zeta$) is the voltage across the electrical double layer at the boundary between the snow crystal matrix and the liquid meltwater in the pore space.

To couple the snow hydrology model to an electrical model to predict the electrical signals that are expected to be measured, equation 5.14 was reformulated, combining equations 5.11, 5.13, and 5.12 (Kulessa et al., 2012).

In their laboratory snow experiment, Kulessa et al. (2012) recognised that $\psi_0 = H_0 \approx 0$ and removed the reference field by subtracting successive measurements. With several months of SP data at Col de Porte (sections 4.4.1 and 4.5.1), it is clear that the reference field varies very little and is a negligible component of the overall SP field measured in this case. Recognising that the total local SP field $\Psi_l = \psi_m + \psi_0$ , and assuming that $\psi_0 \approx 0$ , the resulting reformulated equation 5.14 for SP at the measurement electrode is:

$$\psi_m = \frac{\varepsilon\zeta}{\sigma_W} \frac{S_W}{S_e^n} \frac{L}{kA} Q \tag{5.15}$$

where $Q$ ($m^3$ $s^{-1}$) is bulk discharge in the snow through cross-sectional area $A$ ($m^2$), k is permeability, L is the electrode separation, $S_e$ is effective saturation and $n \approx 3.3$ is the effective saturation exponent. It is possible either to calculate with the snow hydrology model, or estimate using well-established empirical relationships, all of the terms in equation 5.15, and thus calculate a model SP. In addition to calculating snow properties with the model, some variables were measured directly at Col de Porte during March 2019. Bulk discharge (Q) was available from the two Meteo France lysimeters, and cross sectional area (A) of the sensor array was simple to calculate (electrode spacing $\times$ snow depth). Meltwater electrical conductivity $(\sigma_w)$ was measured from the outlet of an old lysimeter adjacent to the SP array during March 2019. The dielectric permittivity of pore meltwater $\varepsilon = \varepsilon_r\varepsilon_0$ = 7.8 $\times$ $10^{-9}$Fm$^{-1}$ , where $\varepsilon_r$=88 for water at 0 degrees C, and $\varepsilon_0$=8.85 $\times$ $10^{-12}$Fm$^{-1}$ is the dielectric permittivity of a vacuum. Permeability ($k$) can be derived from snow density ($\rho_s$) and grain size ($d$) measurements or model outputs using the empirical relationship by Shimizu (1970):

$$k = 0.077 d^2 e^{-0.0078\rho_s}, \tag{5.16}$$

where $k$ is in $m^2$, $d$ is in m and $\rho_s$ is in kg $m^{-3}$. This empirical relationship was verified by Jordan et al. (1999) to apply to grain size diameters of 0.33 mm to greater than 2 mm, which are what is expected to be encountered in the field. Therefore equation 5.16 is expected to be robust for the purposes of this study. The effective saturation ($S_e$) and relative saturation ($S_w$) are related thus:

$$S_e = \frac{S_w - S_w^{ir}}{1 - S_w^{ir}} \tag{5.17}$$

The value of $S_w^{ir} = 0.03$ was taken, as in Kulessa et al. (2012). This leaves all the variables in equation 5.15 with either measured, modelled or suitable empirically derived values, with one exception. The zeta potential ($\zeta$) is unknown here, and is generally poorly constrained. The zeta potential is principally a function of pH and electrical conductivity. The electrochemical properties of the electrical double layer at the snow grain surface will change as the snowpack evolves from fresh snow, due to the effects of melting, recrystallisation and preferential elution of ions. In laboratory experiments using fresh snow, pH and electrical conductivity were observed to increase and decrease respectively, following an expected sequence as elution of ions took place (Kulessa et al., 2012). At the end of these experiments, pH and EC were found to vary little once the snow was mature. Zeta potential can be related to pH, electrical conductivity ($\sigma_w$) and meltwater pH at the point of zero charge ($pH_w(pzc)$):

$$\zeta(\sigma_w, pH) = [\alpha + \beta \log_{10} \sigma_w] \left( \sin \frac{\pi}{12} [pH_w - pH_w(pzc)] \right) \tag{5.18}$$

As in Kulessa et al. (2012) and previous laboratory studies, $pH_w(pzc)$ was taken to be 3.6 in the absence of suitable measurements. The zeta potential in this instance was calculated to have changed from $\sim -7.5 \times 10^{-2}$ V at the start of the experiment when the snow was fresh, to $\sim$ +1.5 $\times$ $10^{-2}$ V at the end, when the zeta potential was fairly constant. The values of pH and EC calculated by Kulessa et al. (2012) were found to be similar to those measured in supraglacial snow in Switzerland by Thompson et al. (2016). The pH values measured in March 2019 at Col de Porte were similar to both these previous studies ( 6.2-6.7), but the electrical conductivity was different ( 6.5 $\times$ $10^{-3}$ S $m^{-1}$).

Previous work has focused on relating SP measurements to bulk snowpack quantities such as bulk runoff, and mean liquid water content. With layered snowpack models, and SP measurements in an array, it is possible to investigate how SP signals vary through the depth of the snowpack. To calculate the SP we expect to measure in the snow, we need to be able to estimate or calculate the variables in equations 5.15, 5.16 and 5.17 (see table 5.4).

All of the modelled variables except $S_w$ are outputted by FSM2 directly. To calculate $S_w$ from model output, porosity ($\phi$) and volumetric water content ($\theta_w$) are required, plus snow liquid water fraction and snow ice fraction. $S_w$ is given by:

$$S_w = \frac{\theta_w}{\phi} \tag{5.19}$$

**Table 5.4:** Data (measured or modelled) required to calculate expected self potential in snow.

| **Modelled variable** | **Units** |
|---|---|
| Liquid water flux (Q) | $m^{-3}$ $s^{-1}$ |
| Relative water saturation ($S_w$) | - |
| Snow density ($\rho_s$) | kg $m^{-3}$ |
| Snow grain diameter (d) | m |
| **Measured/estimated variable** | **Units** |
| Porewater electrical conductivity ($\sigma_w$) | S $m^{-1}$ |
| Zeta potential ($\zeta$) | V |

Porosity $\phi$ is given by:

$$\phi = 1 - \frac{S_{ice}}{\rho_{ice}\Delta z} \tag{5.20}$$

where $S_{ice}$ is the ice mass of a snow layer (kg $m^{-2}$) , $\rho_{ice}$ is the density of ice (917kg $m^{-3}$), and $\Delta z$ is the thickness of the layer of snow. $\theta_w$ is given by:

$$\theta_w = \frac{S_{liq}}{\rho_w \Delta z} \tag{5.21}$$

where $S_{liq}$ is liquid water mass in the snow layer (kg $m^{-2}$) and $\rho_w$ is the density of water (1000 kg $m^{-3}$). FSM2 only gives outputs for $S_{liq}$ and bulk snow water equivalent (*SWE*), so to get $S_{ice}$ the relationship $SWE = S_{liq} + S_{ice}$ is used.

### 5.5.3 Electrical model sensitivity

Analysis was carried out to understand how sensitive the modelled self potential is to changes in the modelled parameters, as small changes in them could result in large differences in the modelled SP. To understand the effect of changes in the modelled parameters, each parameter was varied whilst keeping the other parameters constant at plausible values for a thawing snowpack. The effect on the modelled SP is shown in Figure 5.38. It is clear that sensitivity to variations in snow properties varies widely. The variables which have most effect on the modelled self potential are relative water saturation and snow grain radius. The effect of changing relative water saturation is particularly large (note the Figure is plotted with a log scale y-axis). As $S_w$ tends towards the irreducible water saturation, 0.03, the modelled self potential tends to infinity, with tiny changes in $S_w$ resulting in changes of several orders of magnitude in the modelled self potential. Changes in the zeta potential have a large effect on the modelled SP. This could have a significant impact since the zeta potential is impossible to measure directly. The modelled self potential is less sensitive to changes in density, and to electrical conductivity in the range of the measurements made in Switzerland by Thompson et al. (2016).

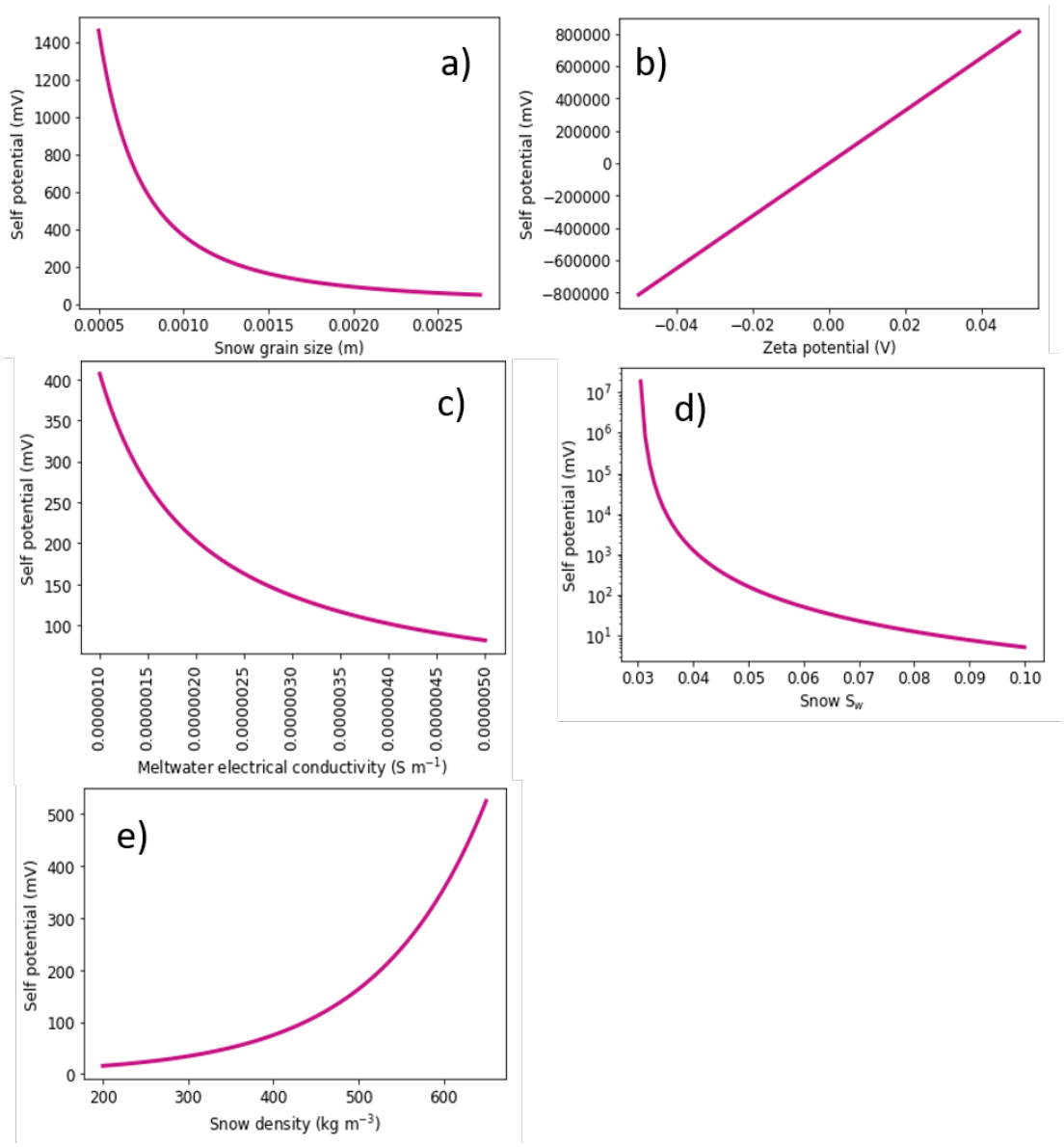


**Figure 5.38:** Modelled self potential in mV given snow grain size of 1.5 mm, meltwater electrical conductivity of 2.5 $\mu$S m$^{-1}$, $S_w$ of 0.05, snow density of 500 kg m$^{-3}$ and a bulk meltwater runoff rate of 0.004 kg m$^{-2}$ s$^{-1}$ when parameters are varied in turn. Sub-figures a) to e) show effect of grain size, zeta potential, meltwater EC, relative water saturation and density respectively.

### 5.5.4 Coupling FSM2 to the electrical model

It can be seen from equation 5.15 and 5.17 that the effective saturation is undefined when $S_w = S_{irr}$. For the electrical model, calculating the 'in-between-timestep' water saturation was calculated, because by definition in the free draining and bucket models, the water saturation is always less than or equal to the irreducible water saturation at the end of the timestep, and therefore the calculated SP at the end of the timestep would always be zero.

The mass conservation equation is:

$$\frac{\partial \theta_w}{\partial t} = -\frac{\partial Q}{\partial z} \tag{5.22}$$

This can be discretised as:

$$\frac{\theta_{w,k}^{(n)} - \theta_{w,k}^{(n-1)}}{\delta t} = \frac{Q_{k-1} - Q_k}{\Delta z_k} \tag{5.23}$$

for layer *k* at timestep *n*. If constant flux through the timestep is assumed, the mid-timestep water content can be calculated as:

$$\theta_{w,k}^{(n-1/2)} = \theta_{w,k}^{(n)} + \frac{\delta t}{2}\left(\frac{Q_k - Q_{k-1}}{\Delta z_k}\right) \tag{5.24}$$

This mid-timestep water saturation was calculated and used in the electrical model to generate synthetic self potential measurements.

### 5.5.5 Coupled model results

As shown above, the best performing configuration of FSM2 for predicting runoff parameterises density as a function of overburden, and uses a gravitational drainage hydrology model. Therefore this was the model configuration chosen to couple to the electrical model.

The electrical model was coupled to FSM2 and run for the 2018-2019 winter season. During the period of diurnal melting in late March 2019 (see Figure 5.39a), it was able to produce synthetic self potential signals of the same order of magnitude as the measured self potential signals, although the magnitudes were different from those measured. Because of the dependence on the modelled runoff, the modelled self potential signals had similar characteristics to the modelled runoff discussed above. The peaks were generally too early compared to the measured self potential, and the peaks were also too narrow. Figure 5.39b shows the inter-layer fluxes, which coincide well with the peaks of self potential, although

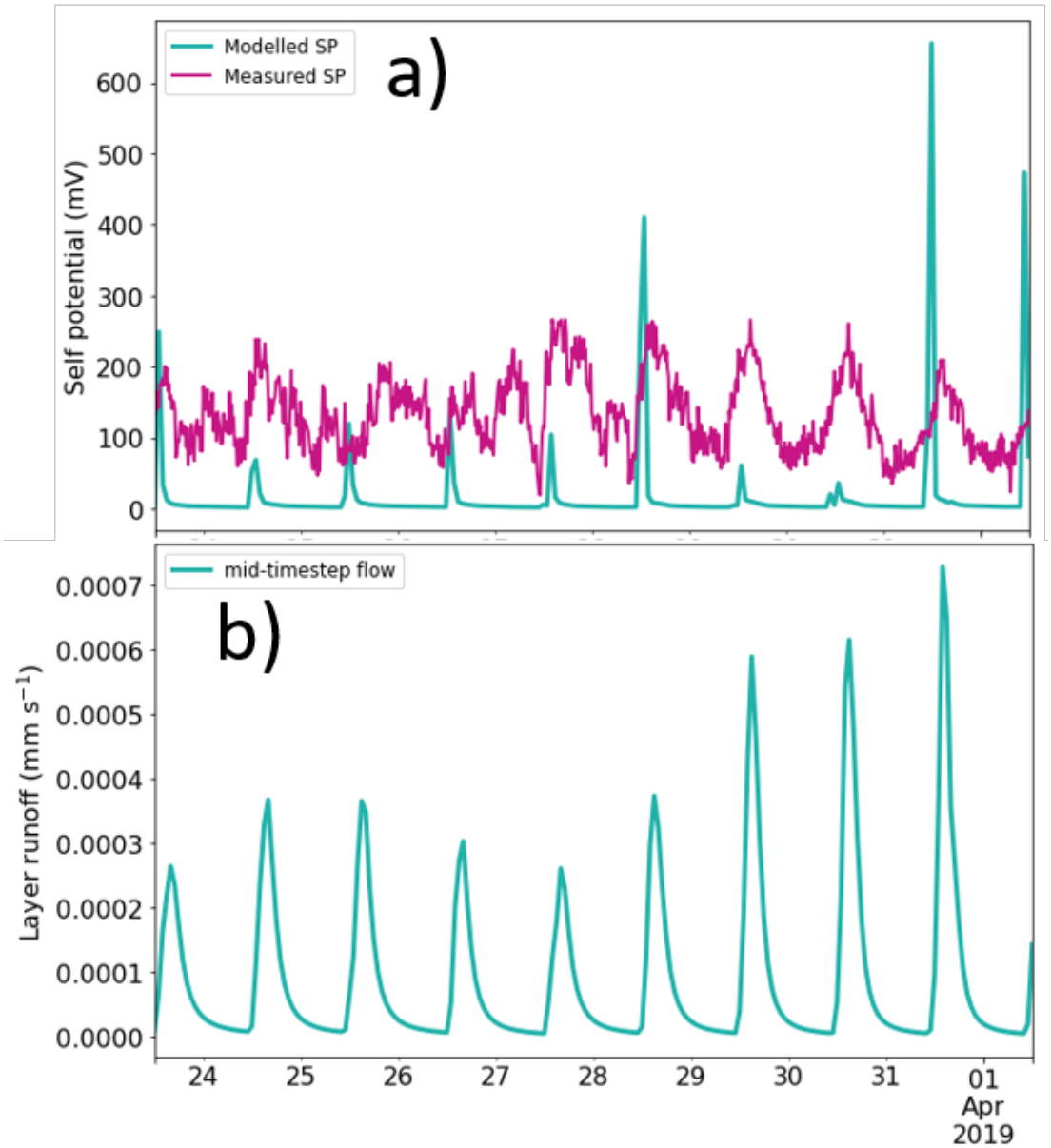


**Figure 5.39:** a) Modelled self potential during diurnal melting in late March 2019 using the electrical model coupled to FSM2 (density - overburden, gravitational drainage hydrology) and measured self potential signal. b) Modelled inter-layer meltwater flux for the same level at which self potential was measured.

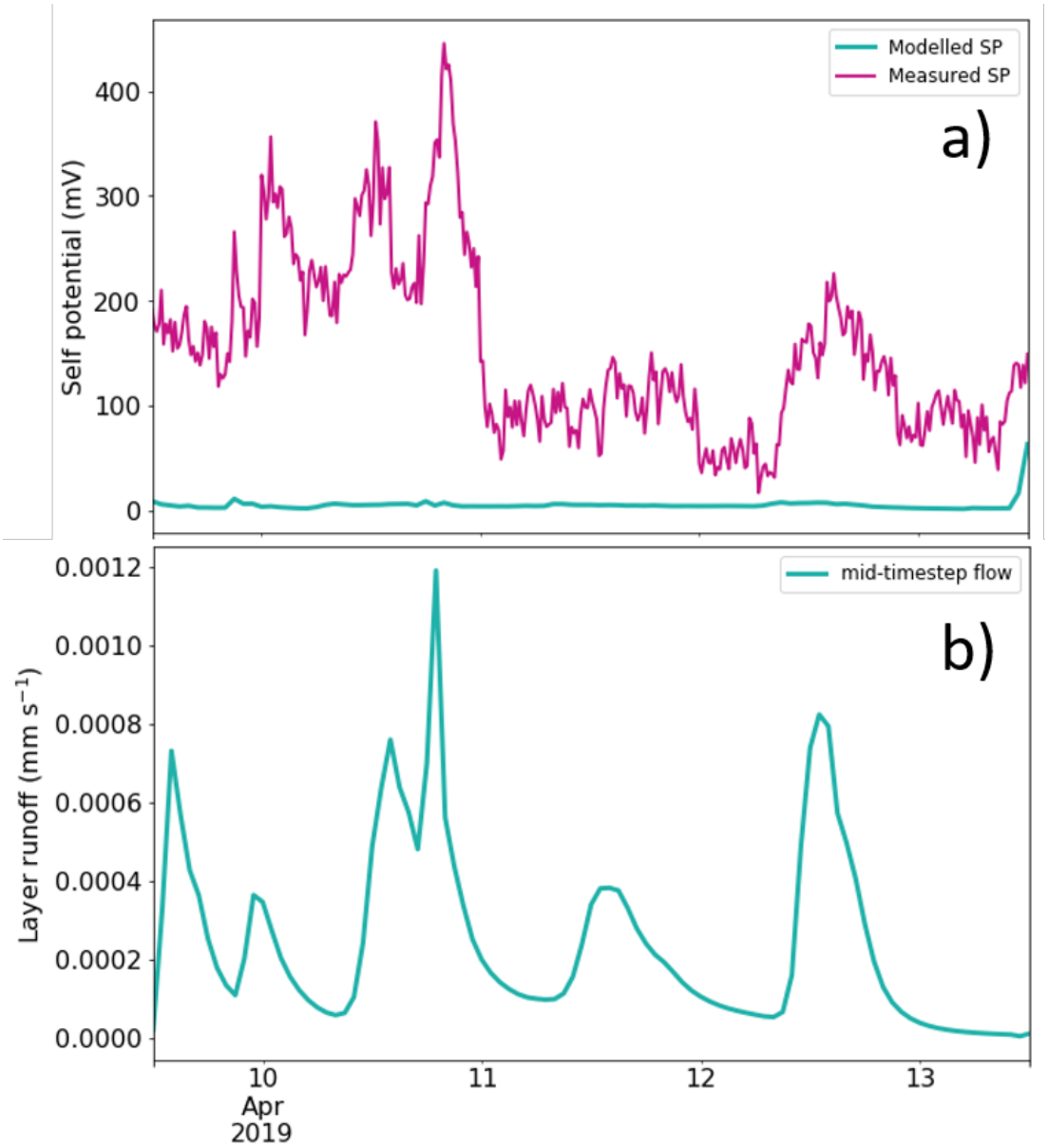


**Figure 5.40:** a) Modelled self potential during a rain-on-snow event in April 2019 using the electrical model coupled to FSM2 (density - overburden, gravitational drainage hydrology) and measured self potential signal. b) Modelled inter-layer meltwater flux for the same level at which self potential was measured.

again the peaks are narrower than the self potential peaks. During the rain-on-snow event in April, the model was not able to reproduce the measured self potential signals well at all (see Figure 5.40a). However, the modelled internal flux between layers matches the self potential data rather well in terms of timings and shapes of peaks.

### 5.5.6 Empirical relationship between modelled flow and measured self potential

Due to the electrical model being subject to large uncertainties because of its sensitivity to snow parameters, an empirical method was tried. For the period from mid-March to mid-April 2019, when the SP array was working well and has been shown above to be responsive to hydrological parameters in the snow, a linear relationship was derived between the mean measured self potential within the snow, and the modelled flux in the corresponding layers of the snowpack. FSM2 was used with the gravitational drainage hydrology and overburden density options. Figure 5.41 shows the linear relationship can give some predictive skill with a correlation of around 0.4. Figures 5.42 and 5.43 show this relationship applied to predict fluxes within the snowpack, compared with the modelled flux from FSM2. It can be seen from the March plot that the predicted flux compares well with the modelled flux, but in April the prediction was not as good. The locations of peaks matches well but the magnitude is quite different - out by as much as a factor of four on the 12th and 13th April. Given this mixed success with an empirical technique using model data, whilst it does give some insight in to the timings of peaks, it mostly highlights that using FSM2 is an effective way to predict internal fluxes. It also adds to the evidence that the modelled peaks of runoff (in this case internal) are too narrow, as found when comparing modelled basal runoff to observed runoff in section 5.3.5.

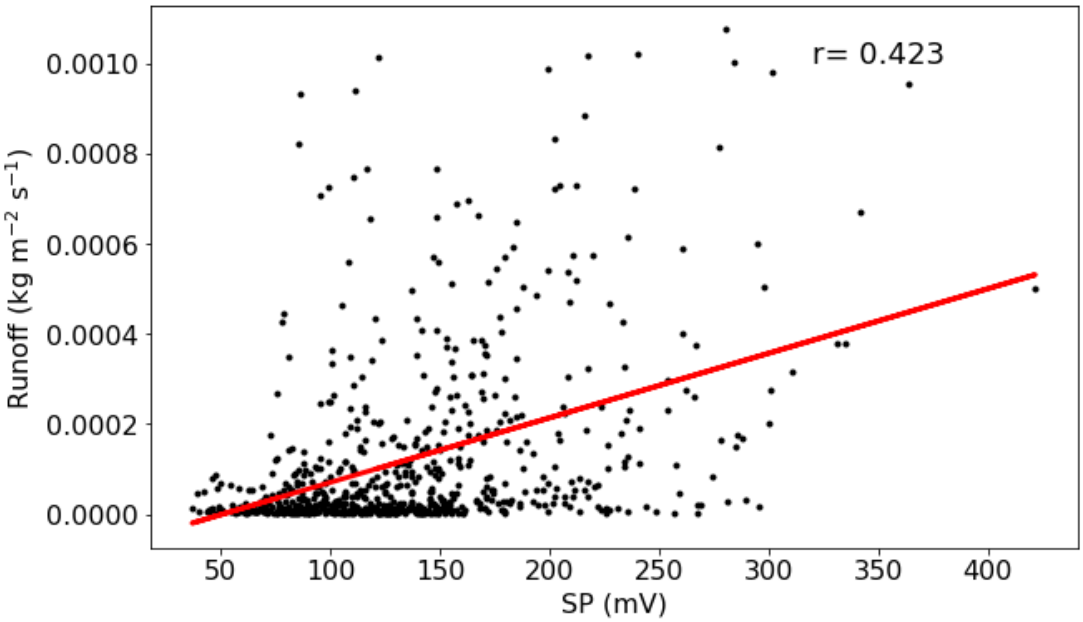


**Figure 5.41:** Linear fit between measured self potential and FSM2 modelled runoff at the same level in the snowpack for the melting period in spring 2019.

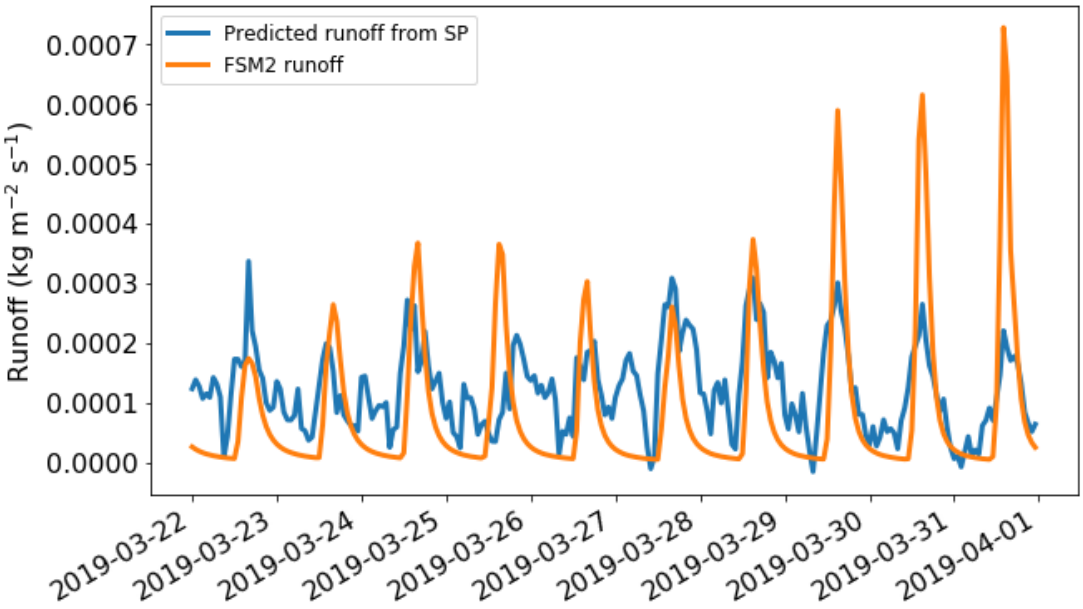


**Figure 5.42:** Predicted and modelled internal flux during diurnal melting in March 2019.

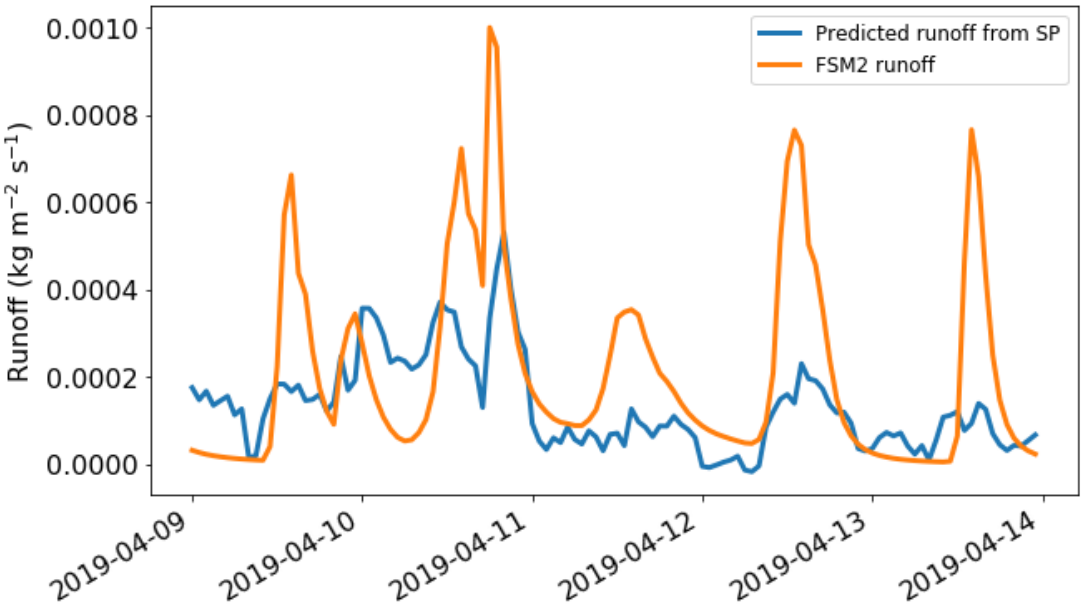


**Figure 5.43:** Predicted and modelled internal flux during rain-on-snow in April 2019.

# Chapter 6

# Discussion and conclusions

## 6.1 Introduction

This chapter sets out the extent to which the aims set out in chapter 2 have been met, and discusses the key findings of this research and their relevance to existing work. An outlook for future work is included, which sets out the ways this work can be exploited and improved in future, and outlines key learning points found during this research which will hopefully streamline and help future research to succeed. For ease of reference, the aims are restated here:

1. Design, build and install a system to measure electrical signals in the snowpack from both SP and ERT measurements
2. Relate these measurements to water content and fluxes in the snowpack, and test the system's sensitivity and utility for long term snow hydrology monitoring.
3. Run and evaluate a physically-based snow hydrology model's (FSM2) performance at predicting SWE and basal runoff using long time series of observed driving data at Col de Porte, and investigate the effects of parameter choice on model performance.
4. Couple FSM2 to a model of electrical processes in a thawing snow pack, in order to evaluate the capability of a coupled system to combine model and measured data to monitor snow hydrological variables.
5. Run FSM2 in a distributed framework over the region of the Alps around Col de Porte, and evaluate with the available verification data over several seasons to assess the performance of FSM2 over the region, and the effect of changing model parameters in a distributed framework.

## 6.2 Aims 1 and 2 - designing and building the geophysical array, and relating field measurements to snow hydrology

In this section the extent to which the aims have been met of building a geophysical array, and relating the measurements to hydrological and meteorological measurements, is discussed.

### 6.2.1 Self potential measurements

Self potential signals were successfully measured for (parts of) two winter seasons. Gaps in the data were present due to power outages, and a significant amount of the data were not used because the snow cover was not deep enough to cover all the electrodes. However, for two periods each season enough data were available to investigate the associated self potential signals.

During the periods of diurnal melting driven by solar radiation in late March 2019 and mid-March 2020 (figures 4.6 and 4.13), a diurnal cycle was visible in the SP signals, which ties in with expected generation of surface melt. In both cases SP signals were registered within the snowpack before runoff was detected in the lysimeters, showing the utility of the SP method as an internal meltwater flow sensor. The signals from the three different heights of measurement did not show any evidence of the highest sensors registering a signal first, followed by the lower ones as meltwater percolated vertically through the snow. The dye-tracing experiments showed the high speed of water percolation in this ripe snowpack (figure 4.7) which could explain the coincidence of peaks at all three levels. However, another perhaps more likely explanation is due to preferential flow along and near the poles delivering meltwater past the electrodes at roughly the same time. Additionally, the depressions that formed around the poles may have helped meltwater to preferentially flow towards and down the poles. In this context, whilst the method was as non-invasive and non-destructive as possible, it is likely that the measurement equipment influenced the measurements to some degree.

In the rain-on-snow events that occurred in mid-April 2019 and March 2020 (figures 4.8 and 4.12), peaks in the SP signal were attributable to both rainfall percolating through the snow, and subsequent surface melting due to positive air temperatures. However, by this stage in the season, preferential melting around the poles had exposed more of the electrodes (see figure 4.9), and one of these levels began to give spurious readings in 2019. It was still possible to see clear peaks in the one remaining level of usable data though. The SP peaks occurred earlier than the lysimeters registered peak runoff, again showing the utility of the SP method as a sensor of internal flows. With only one level of electrode data available, it was not possible to compare peaks in SP at different levels, but it is expected that the same preferential flow will have occurred close to the poles meaning that differences between readings at different heights will have been difficult to attribute to the timing of meltwater percolation vertically downwards.

The system was designed to withstand the demands of an alpine winter season, and it did generally prove to be durable enough. However, by the end of the first season it was clear that the poles had moved due to a combination of ground heave, and snow settling and movement. Due to the gentle slope in the topography, the snowpack crept along this gradient over the course of the season. This bent the poles and moved one of them several centimetres further into the ground than when initially installed. The electrodes themselves remained well-attached to the poles and provided stable readings, although the drift noted in the lowest layer of sensors by the April 2019 rain-on-snow event was an exception. It is possible that more electrodes would have recorded drift or spurious readings if they were buried in the snow for longer, but when they were in the open air the readings were noisy and subject to large temperature fluctuations as high as 10-20°C on sunny days followed by clear nights (e.g. figure 4.10b), so any drift was difficult to distinguish from other effects.

### 6.2.2 Strengths of SP system

Aside from some disturbance of the snowpack through preferential melting around the poles, the SP measurements were non-destructive, and required no intervention from a human observer. As shown in section 4 the SP measurements relate clearly to melt generation and flux during periods of melting, both in solar-radiation driven surface melting, and rain-on-snow events. The timing of SP peaks precedes those measured by lysimeters, indicating that the system was sensitive to internal water flux. The self potential signal was qualitatively similar to modelled internal fluxes, adding evidence that the self potential sensors were sensitive to internal water flux.

The SP system was inexpensive and simple to build and install, and withstood the extremes of two alpine winters successfully. The logger system was easy to program, and by using a common system (Campbell Scientific CR1000) it was very easy to add extra sensors to the same set-up to make additional measurements such as temperature, and soil moisture in the second season. The system had low power requirements, and while it was connected to mains power at Col de Porte, it would be straightforward to use battery power or solar panels at a more remote location without mains electricity. It was simple to make measurements at a high frequency (5 second intervals in this case) and the relatively small number of electrodes meant that data volumes were small enough to transfer over an internet connection without issues.

### 6.2.3 Limitations of SP system - array design

The SP system was of course subject to a significant number of limitations. The depth of snowpack required to cover the sensors was deep - approximately 50 cm. Whilst this amount of snow was present for a large part of the 2018-2019 winter, 2019-2020 was much less snowy, so long periods did not have enough snow to use the measurements. While the system was able to make measurements non-invasively, it was clear that the presence of the poles affected the snowpack over the season (see Figure 4.9). Preferential melting around the poles may not have only affected the flow of meltwater. The air gaps created around the poles also affected the electrical contact, so the depth of snow actually covering the electrodes properly was lower than the measured snowdepth nearby. This was particularly problematic in the second season when the snowpack was shallower. Using hollow poles was necessary due to supply constraints, weight and cost, but this may have allowed meltwater to flow quickly down the inside of the poles. This could have got inside when the snowpack was very deep through the top of the pole, or through where the electrodes were attached to the poles. Snow creep and movement at Col de Porte did cause the poles to move over the course of the season - a few cm over several months. This may have been less of a problem at a completely flat site, but given that most sites, especially in mountainous areas, are likely to have some sort of slope, this is worth bearing in mind. The poles held up after two seasons but only one season had deep snow cover for a long period; it's not clear how much they would have been damaged had the second year had as deep a snowpack as the first. Ground heave caused by frost may have contributed to pole movement too.

### 6.2.4 Limitations of SP system - data acquisition

The reference measurements were mostly stable, especially during the second season, but they were still subject to some variations of uncertain origin. These variations could have been caused by several possible factors: electrical interference from nearby infrastructure, effects of drying and wetting the soil and the porous Petiau electrode contacts, freezing and thawing effects or electrical issues with connections to the logger. The array electrode measurements were also subject to some jumps in the data which were difficult to explain with hydrological or meteorological reasons. By making measurements at five second intervals, it was possible to take longer period averages to remove some of this high-frequency variation, but at times they still affected the data, mostly during the earlier winter season. The system seemed to perform better when covered in snow rather than exposed to the air. Logger outages, probably caused by power supply issues, meant that some of both winters' measurements were not made. Fortunately most of the main periods of interest were uninterrupted.

### 6.2.5 Limitations of SP system - data interpretation

Whilst it was generally straightforward to relate meteorology and hydrology to the timing of peaks in the SP signal, the magnitudes of the signals were difficult to relate to the prevailing conditions. This is probably due to the large number of contributory variables to the magnitude of the signal, and the sensitivity of the signal to these variations (see sections 5.5.2 and 5.5.3). If the signal was responding to a straightforward hydrological signal such as a pulse of meltwater, the timing of this tied in well with peak air temperatures, peak incoming shortwave radiation or the timing of a period of rainfall. But the magnitude of this peak could be modulated by snow grain size, liquid water saturation, snow chemistry and snow density. Small changes in these variables result in large differences in the magnitude of the signal.

It was hoped that by having an array of measurements, differences between the signal at different vertical and horizontal positions could be related to heterogeneities in the fluxes of meltwater. Unfortunately this was not the case. In the vertical, this was partly limited by the lack of sufficient snow depth for much of the time. However, when there was enough snow present, there was no variation vertically that could be explained through hydrology or meteorological factors. There are two likely reasons for this. First, the already mentioned sensitivity to snow properties meant that the magnitude of the signals was controlled by more factors than just the runoff. Even if there were vertical differences in runoff, these were masked by variations in other properties meaning the magnitudes were difficult to interpret. Second, the speed with which the runoff percolated through the mature melting snow (see Figure 4.7) meant that differences between signals at measured heights that were tens of cm apart were impossible to differentiate from the high frequency variations present in the signal. From the dye tracing experiments the vertical velocity was in the order of 0.1 - 0.5 cm $s^{-1}$ i.e. when the dye was applied it took around 1 - 3 hours to reach the base of a 1 m deep snowpack. When these signals were smoothed for easier analysis, any possible vertical variation was even more difficult to see. Preferential flow down and around the poles may have also contributed to this lack of vertical resolution in the data.

In the horizontal plane, it was also difficult to relate differences in the signal between pole positions to meteorological and hydrological factors. This is partly due to the stochastic nature of flow through snow: it is very difficult to predict and observe these lateral heterogeneities. The position of the poles may have also played a part too. Because of the requirements of the ERT system, the four poles were placed in a square arrangement with a spacing of 75 cm. If the SP array was not constrained like this, it would have been possible to arrange the SP electrodes differently. A square with larger spacing or a line of poles over a longer lateral distance may have been able to detect horizontal differences better.

### 6.2.6 Electrical Resistivity Tomography

After failing to get ERT to work successfully in snow, this shows that perhaps there is a very good reason why there is no previously published literature covering this topic. Despite some indications that ERT might work as a detector of melting snow (see section 3.5), this project completely failed to implement successful measurements in the field. This was of course very disappointing, but hopefully some points from this experience can be taken forward to give any future work in this area a better chance of success.

The choice of the Geotom instrument was made partly due to its availability at BGS, but also due to its ability to make measurements with very low currents. This should have meant that despite the high resistivities expected in snow, measurements should have been possible. This low-current strategy is recommended for any future work. Despite the Geotom having been used in a long term monitoring experiment previously (Murton et al., 2016), the power and battery charging set up were the main problem with the experiment. Despite the improvements made after the first season, problems persisted meaning that no data were collected in the second season either. Clearly a long term test of the exact set up to be used was required, but unfortunately time and logistical constraints meant this was not possible. These problems were compounded by the COVID-19 lockdown; had it been possible to visit Col de Porte in March 2020 as planned then perhaps some data acquisition would have been possible. As well as thoroughly testing the power system, any future installations should test the performance of different electrode designs in laboratory experiments. The steel electrodes used in this project worked well in short experiments (see section 3.5) but thorough testing and a comparison with the improved mesh electrodes would have been insightful. Unfortunately time and logistics constraints did not permit this. Due to the power supply problems, the mesh electrode design (Figure 3.9) could not be evaluated at all due to the lack of data in the second season. Future installations of a prototype ERT system would not be as easy to upscale and develop into a network as the SP array. This is partly through the high cost of the measurement units and control equipment, and partly through their large power requirements.

Another direction in which the ERT could be taken in would be to develop the ground array as a sensor for snowmelt percolation, although this is not a novel concept (see French and Binley (2004)). However, this possible application of ERT could probably be much more cheaply achieved through dielectric soil moisture sensors to gain similar data about snowmelt percolation into the soil.

In summary, this work has confirmed the difficulties associated with ERT in snow hinted at by the lack of previous successful work. Although some useful insight has been gained about the possible pitfalls of this method, it seems likely that efforts would be better spent utilising more established measurement techniques such as GPR (Mitterer et al., 2011), GPS (Koch et al., 2014), and possibly SP measurements if the goal is to improve model representation of internal water dynamics in snow.

## 6.3 Aim 3 - evaluate FSM2 at Col de Porte

The model configuration which gave the 'best' performance depended very much on what the criteria for performance were, and different configurations gave good performance when evaluated over different timescales and when different variables were predicted.

As expected, the model configurations which accounted for storage of water in the snow layers and were able to refreeze water generally performed better (the bucket model and the gravitational drainage model) than the simplest model with free-draining hydrology. Parametrising density as a function of age gave the best results for predicting SWE for all hydrology parametrisations, and parametrising density as a function of overburden performed best when evaluating predicted runoff. However, for the free draining hydrology model, density as a function of age performed better for both runoff and SWE, for both the three and ten layer configurations.

The model gave very similar performance for the three and ten layer configurations when using the bucket model and gravitational drainage hydrology schemes (e.g. Figure 5.6). Because the number of layers was not relevant to the free draining hydrology (the water just drains to the base of the snowpack at the end of each timestep regardless of the number of layers or the properties of the layers), the performance was the same for both the three and ten layer models with this hydrology set up.

Because the performance of the model was so similar between the two different layer configurations, the benefit of running the model with greater vertical resolution was limited. Running with ten layers instead of three took slightly longer (although still under a minute) and created larger output files. Previous work on multi-layer models has generally focused on applications in avalanche prediction, such as Bartelt and Lehning (2002) and Brun et al. (1992), and in radiative transfer modelling chiefly for interpretation of remote sensing data e.g. Tuzet et al. (2017). Work to represent preferential flow in models, such as that by Katsushima et al. (2009) has used multilayer model frameworks, and this work has shown that representing some of these complex processes is possible using a flexible and quick-running model.

From the long period evaluation, SWE was best predicted using the density as a function of age parametrisation (Figure 5.4), and runoff was generally predicted best using density as a function of overburden. Since the main purpose of this study was to improve runoff prediction, the configuration with density as a function of overburden was chosen to be used for further analysis.

It is worth remembering that hourly runoff is very variable due to the heterogeneous nature of the snowpack, and the varying ability of instruments to measure it. At the hourly resolution, the two lysimeters at Col de Porte had a correlation coefficient of 0.782 (Figure 5.3). While this value would be very impressive for a model performance, this shows how different the two co-located instruments are when measuring such a variable quantity. This puts any model performance into context: the stochastic nature of runoff compared to say, SWE, is clear when model performances for these two variables are compared.

When looking at shorter timescales rather than evaluating the performance statistically over a long period, it is clear that the gravitational drainage model reproduces the overall shape of the runoff curve best during diurnal melting (Figures 5.7 and 5.8). The free draining model always lets too much runoff reach the base of the snow too quickly, and the bucket model is somewhere in between as it can cater for storage and refreezing in the snowpack. The difference between the two density formulations is not large for the free draining or bucket models, but during diurnal melting the gravitational drainage model shows a significant improvement, with the modelled magnitudes matching very well with the observed ones. For both density parametrisations, the runoff peak subsides too quickly compared to observations.

When looking at runoff and SWE over multiple seasons (Section 5.3.5), and when looking at runoff over short periods (Section 5.3.5), gravitational drainage produced the best results. But when looking at cumulative runoff and snowdepth over one season (Figures 5.9 and 5.10), the best performing model was not consistently the gravitational drainage model. With density as a function of age, the free draining model tracked the observed cumulative runoff most closely, and similarly the free draining model produced a better prediction of snowdepth with density as a function of age. Previous work, such as that by Wever et al. (2014) and Würzer et al. (2017), has focused on longer term evaluation, whereas this work looked at hourly timescales, as this is where combining SP and models may be able to add most value to predictions. Work which has looked at these shorter timescales has used idealised situations such as the analytical test case by Clark et al. (2017) or 2D modelling of preferential flow by Leroux and Pomeroy (2017).

### 6.3.1 Parameter adjustment

The irreducible water saturation was varied to investigate if this improved the shape of the modelled runoff and slowed the release of meltwater down. In general, the shape of the runoff peaks was not changed much by varying the irreducible water saturation (Figures 5.15 and 5.16), although the magnitude of peaks tended to be a little higher with lower $S_{ir}$. When observed runoff was low, low $S_{ir}$ produced peaks in runoff that were greater than the observed runoff, and high $S_{ir}$ produced no runoff at all in these situations. When the observed runoff was greater, there was much less difference between the different $S_{ir}$ scenarios. This suggests that there could be some sort of threshold value below which the runoff is affected by $S_{ir}$ to

a greater extent, and above which $S_{ir}$ does not have a large effect on the runoff produced by the model. This effect was less noticeable with density as a function of overburden than with density as a function of age. Work investigating $S_{ir}$ in snow has been carried out but mainly to try constrain its value experimentally such as by Coléou and Lesaffre (1998), but its effect on runoff has not been investigated widely.

When the varied irreducible water saturation was tested over a longer time period, it was found that the model performance improved as $S_{ir}$ tended towards zero (Figure 5.14). This is clearly not physically consistent, and also is the opposite conclusion to that derived qualitatively from the shorter period runoff curve shape.

With these results in mind, it was concluded that the optimum value of $S_{ir}$ was around 0.03, which is the default value in the model. This value seems to balance the improvement in long period model performance found by reducing $S_{ir}$, and the improvement in the shape of the runoff curve with increasing $S_{ir}$.

A similar analysis was performed by adjusting the saturated hydraulic conductivity ($k_{sat}$). This was only applicable to the gravitational drainage model. The aim of this adjustment was to increase the length of time that meltwater takes to flow to the base of the snowpack. When evaluated over a long time period, the changes in model performance were tiny. When the effect of changing $k_{sat}$ on the shape of the runoff curve was evaluated over short timescales, it was found, as expected, that reducing the permeability resulted in a slower release of meltwater (Figures 5.17 and 5.18). This change was fairly small though, which was expected after the tiny changes in performance seen over longer timescales.

## 6.4 Aim 4 - coupled electrical modelling

The electrical modelling part of this work sought to extend the work done by Kulessa et al. (2012) and Thompson et al. (2016) and develop their laboratory and field self potential measurements into an autonomous monitoring system. Part of this aim was to couple the electrical model developed in Kulessa et al. (2012) to a snow hydrology model in order to predict self potential signatures in snow.

The electrical model was successfully coupled to the snow model. However, it became clear through sensitivity analysis that the model is extremely sensitive to snow properties (Figure 5.38). Small changes in these properties result in huge differences in the modelled self potential signal. This is evidently not too much of a constraint when used during short periods of field study where snow properties can be measured easily, and often do not change much over the timescale of the experiment, as in Thompson et al. (2016). However, when using a model to predict these properties, it was apparent that these uncertainties meant that the possible errors in the self potential predictions were very large indeed, and were much greater

in magnitude than the expected signals of interest generated through liquid water motion. That said, it was still possible to model self potential signals for some periods, especially once the snowpack was mature and ripe, and undergoing fairly simple diurnal melt cycles (Figure 5.39). However, when conditions were more complex, such as under the rain-on-snow conditions that were investigated, modelling the self potential was much less successful (Figure 5.40).

The snow chemistry was not predicted by the snow model, so measured values taken during one week in March 2019 had to be assumed to be applicable for the whole two seasons. It is not clear how much effect this had on the predicted signals, but changing the electrical conductivity and snow pH do result in large changes to the modelled SP through affecting the zeta potential (Figure 5.38). To better constrain these snow chemistry properties and improve the modelling, continuous monitoring of the electrical conductivity and pH of the meltwater could be trialled. Due to logistical constraints this was not possible during this field experiment.

A simple empirical relationship between the measured self potential signal and the modelled internal water flux was tested. There was a clear relationship between the measured SP signals and the modelled internal fluxes (Figures 5.41, 5.42 and 5.43). This gave some confidence that the model was reproducing internal water dynamics that were realistic, however as was found with the basal runoff evaluations, the runoff tailed off too quickly when compared to the self potential signals. Magnitude was more difficult to represent, for the reasons noted above.

In conclusion, the electrical modelling showed some promise, but was very sensitive to snow properties. In order to better constrain these uncertainties, future implementations would benefit from monitoring of snow chemistry, and if possible other snow properties. The self potential signals were able to be easily used qualitatively to evaluate the timing of modelled runoff and internal flux, even if there were large uncertainties in the magnitude.

## 6.5 Aim 5 - distributed modelling

It was shown that FSM2 is relatively straightforward to run in a distributed framework, with model runs taking a few minutes to cover an area of 0.5 x 0.5$^\circ$ at a grid point separation of 0.01$^\circ$. Because of FSM2's flexible design, it was easy to compare different configurations with each other. It was clear that the main source of uncertainty was the driving data, which previous work such as by Günther et al. (2019) and Richter et al. (2020) has shown. Driving datasets from SAFRAN and AROME were compared with in situ observations at Col de Porte, and the results of FSM2 model simulations were also compared for the different driving datasets.

### 6.5.1 Numerical weather prediction uncertainty

Precipitation is notoriously variable across even small areas, and when complex topography is added in this can affect the precipitation intensity further. The resolution of the AROME driving data is 1.3 km, so any features which are on smaller scales than this will either be missed completely or need to be parametrised. Two of the elements of precipitation that are particularly difficult to model are convection, and orographic enhancement of frontal precipitation. The fact that AROME underestimates precipitation in general suggests that both of these phenomena are under-represented at Col de Porte. Convection often occurs at spatial scales of less than 1 km, and even when larger showery precipitation develops, sub-gridscale variation is common, especially in mountainous areas e.g. (Lean et al., 2008; Roberts and Lean, 2008; Tang et al., 2013). Frontal precipitation is typically on spatial scales many times greater than a 1.3 km grid, but embedded convection triggered by potential instability and interaction with mountains can cause sub-gridscale intensification of precipitation rates (Smith et al., 2015). In certain precipitation situations known as 'warm conveyors', strong wind flow, moist air and rising topography can combine to enhance the original precipitation rate by up to ten times (Hill et al., 1981). These situations are difficult to model, and if even there was only one such event per year that was poorly modelled or missed, the error in total precipitation for the year could be large.

Regarding precipitation type, the discrimination between snow and rain appears to be fairly realistic in the AROME data. The gap between AROME and observed snowfall is much smaller than the gap between AROME and observed rainfall by the end of the three year period (Figure 5.21). This could partly explain the success of the AROME SWE simulations if much of the precipitation error occurred in the snow-free part of the year.

Temperature showed biases in both the maximum and minimum temperatures (Figure 5.22). The mean minimum bias was actually around zero, but this masked a lot of variation. Maximum temperatures were on average around 2°C too warm in AROME, although again there was a lot of variation within this. Some important controls on maximum and minimum temperature include the radiation balance (i.e. cloud cover and shading), wind speed and snow cover. Generally, AROME had too much short wave radiation (i.e. too much direct sunshine and not enough cloud) and too little longwave radiation (i.e. too little longwave re-emittance from clouds and vegetation) (Figure 5.19). It is not surprising that a 1.3 km model would not model these variables perfectly, as the ancillary topography and land cover type data used is an approximation. The Col de Porte field site has a gentle slope and a slight northerly aspect, and is surrounded by forest on several sides. It is likely that these effects on the radiation balance are the primary cause of errors in the modelled temperatures. Wind has an effect too, and AROME's winds were in general too strong at Col de Porte. Stronger winds prevent efficient radiative heating (in the day time) or cooling (overnight), through turbulent mixing. This mixes air from aloft down to the surface and acts to damp extremes of temperature. Perhaps these

stronger winds mitigate the temperature errors somewhat, and it seems that radiation errors are the primary driver of temperature uncertainty. Another possible source of temperature error in the AROME data is the height and prevalence of temperature inversion conditions, which are a common feature in a continental climate with frequent anticyclonic episodes and can be modelled poorly (Valkonen et al., 2020; Vosper, 2004). Vertical model resolution can cause errors in inversion height. Errors in model representations of inversion formation such as consecutive nights of strong radiative surface cooling and adiabatic warming through descent can lead to mismatches too. Incorrect inversion height in a flat area may not have drastic effects on modelled surface temperature, but in a mountainous region, it could mean large errors in temperature depending on the height of the inversion and the topography.

The modelled wind biases are possibly caused by the representation of friction in the model. Errors could also occur due to the possible inversion issues mentioned above, as wind speed can be affected dramatically near inversions. It is also possible that AROME does not allow the boundary layer (that part of the atmosphere closest to the surface) to 'decouple' easily enough under radiative cooling overnight. This results in the wind speed falling close to zero near the surface, whilst the wind aloft remains close to its free-air speed. When this decoupling occurs, it can enable the temperature to fall more than it otherwise would, as well as causing errors in the modelled wind speed.

It is worth noting that the numerical weather prediction simulations are being made in a climate which is becoming more prone to extremes as the climate warms. This could mean that if the model is designed and calibrated for past climates, it may not simulate extremes due to global heating very well (Scher and Messori, 2019; Sheshadri et al., 2021).

The SAFRAN data (5.20) were generally closer to the observations, as might be expected as they incorporate observations in their data blend. There are still biases, predominantly caused through errors in representing the complex topography and shading from vegetation. These errors were smaller than with the AROME data because SAFRAN takes account of slope and aspect as well as elevation.

### 6.5.2 Distributed model at Col de Porte

With the meteorological uncertainties mentioned above in mind, AROME produced reasonable predictions of daily SWE and runoff at Col de Porte when compared with observations, and FSM2 driven with in situ data (Figures 5.24, 5.25, 5.26, 5.27 and 5.28). Given how good FSM2's performance is when driven with the in situ data, this says more about the quality of the AROME and SAFRAN driving data than the model itself. Bearing in mind the biases in precipitation noted above, the SWE simulations are good, with the best performance for SWE prediction when density is modelled as a function of age, which is the same configuration that performed best in the long period single site evaluation.

When modelled runoff is evaluated for FSM2 driven with AROME compared with either observed runoff or FSM2 driven with in situ data, the AROME runs produce too little runoff over the year (Figure 5.26). The deficit in cumulative precipitation tends to develop early in the season, then stays fairly similar through the snow-covered part of the year, before increasing again during the summer months. This is what might be expected given that the precipitation bias seems to be greater for rainfall than for snowfall.

When the daily difference between modelled and observed runoff is compared (Figure 5.25), FSM2 driven with in situ data shows the lowest mean difference as would be expected. FSM2 with in situ data shows the largest standard deviation in the difference. SAFRAN has a low mean difference and low standard deviation, and AROME has the highest mean difference but a relatively low standard deviation. The high standard deviation with the in situ data perhaps reflects the variability of the real driving, whereas the SAFRAN and AROME data exhibit fewer extremes, resulting in a lower standard deviation, but a greater mean absolute error. There was very little difference between the two density parametrisations by this metric.

As might be expected then, running the model with the dataset which incorporates observed data (SAFRAN) produces the best predictions of daily runoff and SWE when evaluated against in situ model data and observations. The difference between density configurations is marked when looking at SWE, but very small when looking at runoff.

### 6.5.3 Distributed model over the Chartreuse Alps

When evaluating FSM2 over the whole Chartreuse, the analysis was restricted to modelled snow cover fraction due to the remotely sensed data available. Firstly, when considering the mean snow covered fraction over the Chartreuse domain, the difference between the two density parametrisations was tested (Figures 5.31 and 5.32). This was found to make a reasonable difference to fit with observations when snow cover fraction was a linear function of snow depth. In this case, density as overburden performed best. However, when snow cover fraction was an asymptotic function of snow depth, there was very little difference between the two density configurations.

Modelling snow cover fraction as an asymptotic function of snow depth gave much better performance in all three snow seasons when compared with the remotely sensed data. The fact that the density configuration only noticeably affected the poorer snow cover fraction simulations suggests that for this distributed verification, the density model has greatest effect for shallow snow at lower elevations, or at the beginning and the end of the season. If the goal is to model these areas well, then the density model needs to be carefully selected. Conversely, if the area of interest is at a higher elevation with deep snow cover for much of the season, then snow cover fraction parametrisation and thus density choice will have less effect.

When some specific snowy days with clear satellite views were analysed, there were some deficiencies in the model snow cover simulation. Firstly a 'reference' model configuration was chosen (the best performing model in previous tests) (Figure 5.34). Lower elevation slopes and some slopes with a southerly aspect had too little snow in the reference simulations, and north facing mid-elevation slopes had too much snow. This could have been caused by the model driving data having deficiencies in its radiation budget caused by too much shading from topography or vegetation. These errors could also have been caused by FSM2's handling of snow lying under forest cover. It is beyond the scope of this work to evaluate FSM2's performance in forest situations, but work is ongoing to improve FSM2's performance and to improve understanding of the effect of forest cover on the surface radiation balance, such as by Mazzotti et al. (2020) and Mazzotti et al. (2021).

This reference model was compared to other model configurations (Figures 5.35, 5.36 and 5.37). For the different hydrology options, there was not much difference in performance with the bucket model. This was expected, as on daily timescales the performance of the gravitational model and bucket model were fairly similar, as they both account for storage of water and refreezing. The free draining model did show some differences though, with the free model having less snow cover on the days investigated. This also makes sense: if the model is not storing and refreezing water within the snowpack, then it is expected that it will lose snow cover more quickly than a model that does. This was most noticeable on the days analysed at some lower elevations, probably due to the smaller amounts of snow present.

Comparing density models (Figure 5.36) showed that the overburden model had less snow than the age model, and like the free draining hydrology model this tended to be at lower elevations. This could be due to the overburden model diagnosing densities that are too low for shallow snow cover, which results in earlier melting.

The snow cover fraction parametrisation had the largest difference between the reference model and comparison model (Figure 5.37). The linear snow cover option produced more snow cover over much of the domain, with the effect most marked around mid-elevations. Over higher areas with more snow, there was less difference.

### 6.5.4 Distributed model conclusions

It was clear from the analysis performed that FSM2 produced good simulations of snow variables when run with AROME data, both over the whole Chartreuse domain, and at the site specific level. The uncertainties and biases involved were predominantly caused by uncertainty in the driving data, although given some of the errors seemed to be focused on lower slopes with either steeper topography, shaded aspects, more tree cover, or a combination of these suggests that model parametrisations of these effects could be improved.

Given how well the model performed, it is encouraging for future work running such a flexible model over a whole region, and there is scope for a distributed FSM2 to be used successfully in many areas of study such as catchment hydrology, forest microclimate, large area avalanche risk modelling and ecological investigations.

## 6.6 Outlook and recommendations for future work

### 6.6.1 Future development of SP monitoring for snow hydrology applications

It is possible to note some improvements which could be made to the system to address some of the limitations outlined above. Clearly, the number of electrodes which were actually buried in the snowpack was too low, so an obvious improvement would be to position more electrodes lower on the poles, and put them closer together (vertically). For a site like Col de Porte, even if the maximum snow depth is enough to bury the poles, for most of the winter the poles will be exposed to some degree. To avoid the poles influencing the meltwater flow as much as possible, instead of mounting electrodes on poles one above another, poles of varying heights could be installed, with one electrode at the top of each pole. This would be similar to snow temperature sensors used in Switzerland as part of the IMIS network (Lehning et al., 1999). Whilst similar preferential flow and melt problems would undoubtedly be experienced to a degree, this style of installation could mean that the snow above the electrodes remained undisturbed. Another possible configuration of electrodes could be to employ 'settling disks' such as used for tracking snow layer heights and temperatures at Col de Porte (Lejeune et al., 2019). Something like this may reduce the problems with electrical contact and preferential flow along the poles as found in this study.

To reduce noise, siting the array in a more electrically quiet location would go some way to helping this, but in reality this may not be practical. Sites with the requisite infrastructure and power availability are likely to be electrically noisy environments. To mitigate this as much as possible, future installations should include steps to quantify the noise present, so that some of it can be subtracted from the signal, such as that carried out by Weigand et al. (2020). Improving electrode contact may also help reduce noise, as noise is likely to be less of an issue if electrical contact is better.

Whilst the remotely programmable logger set up was useful, the hard-wired multiplexer layout was a constraint. In future, a more flexible arrangement would allow for different combinations of dipoles to be measured, and easier identification of problem electrode pairs.

The difference in noise levels between the Petiau electrodes in the soil, and the lead strip electrodes on the poles was significant. Manufacturing smaller bespoke Petiau-style lead/lead chloride electrodes for mounting as the pole electrodes could be considered, as in the laboratory experiments in Kulessa et al. (2012), but this type of electrode would not be reliable if

exposed to the open air and repeated freezing and thawing cycles. It is possible that a better design using lead, or medical grade electroencephalogram materials (such as that used by Clayton (2021)) would be possible, however the issue of electrical contact will always be an issue with electrodes that are left in situ for long periods. Siting one electrode at the top of each pole could address some of these problems as discussed above.

SP measurements could be combined with temperature measurements at each electrode using thermistors. This would enable verification of when liquid water flow is possible, as in Marchenko et al. (2021), improving interpretation of the SP signals. Future experiments could use lysimeters within the snowpack rather than at the base (Kattelmann, 2000; Kinar and Pomeroy, 2015; Thompson et al., 2016) to quantify better how much flow is occurring within the snow and how this relates to the SP measurements, although this would be a destructive measurement and would not be suited to a monitoring campaign.

Tying in with possible future work using the electrical model, future SP campaigns should endeavour to include snow chemistry monitoring to better understand the evolution of the zeta potential and its effect on the magnitude of the measured SP signal. Extending the chemistry monitoring methodologies of Kulessa et al. (2012) and Thompson et al. (2016) would be a useful starting point.

Given the simplicity and inexpensive build and installation of the SP array, there is clearly the potential for it to be rolled out more widely over a catchment scale to investigate internal water fluxes within seasonal snowpacks. With the limitations on interpreting signal magnitude noted above in mind, the timings of the signals could still be useful for calibrating runoff models in distributed frameworks.

### 6.6.2 Possible future development of ERT array

Future work using ERT in snow should continue to use a low current approach as in this thesis, which was shown to work in laboratory experiments. More thorough laboratory testing using ERT in snow is necessary to ensure a more successful field campaign than in this project. If a successful laboratory system is set up, then attention should be focused on comparing the performance of different electrode designs to select the best design for field deployment. To mitigate risk of failure of a monitoring approach, future work could focus on a manual survey approach, alongside intensive snow property measurement, such as carrying out ERT measurements in the wall of a snow pit. If this was shown to work well, then future consideration could be given to monitoring approaches.

### 6.6.3 Modelling outlook

The work in this thesis, using an open source, flexible snow hydrology model, has underscored the value of easy-to-run modular models which make investigation of the effects of changing parameters straightforward. This thesis has also underlined the importance of marrying together any future modelling work with observational campaigns to evaluate performance, and guide future observation strategies.

Where previous work to understand the effects of parameter selection on model performance have often used cumbersome ensemble frameworks (Lafaysse et al., 2017), or huge numbers of model configurations (Essery et al., 2013), this work has highlighted the potential for FSM2 to be used in a simpler and more user-friendly workflow. This thesis highlights the importance of further work using FSM2 to make the most of its potential.

This work has focused on seasonal Alpine snow packs, and the applications for predicting meltwater flux in firn and Arctic snow could be a future area of study. Given the success of running FSM2 with NWP data in a distributed framework, further evaluation of this type of modelling would be insightful, such as across a larger area with surface observations available in addition to remtotely-sensed data, such as Switzerland or the western USA. Work using FSM2 and reanalysis data by Priestley and Ewing (2022) and Alonso-González et al. (2021) has also highlighted the applications of FSM2 to ecological and climatological studies.

The modular structure and simplicity of use of FSM2 could lend itself to incorporation into wider land surface models, such as JULES (Best et al., 2011) or CESM (Kay et al., 2015), to improve the representation of snow over existing schemes incorporated into these Earth system models.

Alongside further exploration of the relationship between snow chemistry and SP signals, any future coupling of an electrical model and a snow hydrology model as carried out in this thesis should endeavour to quantify and represent the effect of snow chemistry on zeta potential and hence the magnitude of SP signals. Alongside this, the promise of empirical investigation should be exploited. Making snow chemistry measurements can be difficult and time consuming, especially in a monitoring framework, so further investigation of the potential for an experimentally-derived relationship between SP and snow hydrology parameters could be combined with distributed modelling to understand meltwater flows and timings across a catchment-scale.

## 6.7 Summary of recommendations for future work

The key recommendations for future work based on the experience and conclusions in this project are listed below:

1. A robust system for quantification and removal of noise in the SP signals should be built into the system, such as running separate dipoles to measure noise, such as carried out by Weigand et al. (2020).
2. In order to exploit the possibility of detecting lateral and vertical heterogeneity in water flows, future arrays should have more electrodes at lower heights within the snow pack, and be spaced over a greater area, to increase the chance of being able to detect preferential flow paths and wetting front downward percolation.
3. Whilst the lead strip electrodes in this thesis worked well, investigation and comparison of performance of different configurations and electrode types should be carried out, such as installing electrodes on settling disks (Lejeune et al., 2019), on the tops of poles of different heights (Lehning et al., 1999) or using different electrodes (Clayton, 2021).
4. A low-current system already suited to monitoring deployment should be used for future ERT work in snow, such as the Geotom used in this thesis.
5. A thorough laboratory test experiment should be run before any field ERT deployment, to ensure remote control and power systems are functioning correctly.
6. Given the low cost of SP sensors, future work should investigate the potential to deploy sensors over a larger area coincident with existing meteorological and hydrological sensors, to enable SP signals to be used to calibrate melt timing in distributed modelling frameworks. Simple individual SP electrodes with loggers powered by battery power instead of mains electricity could be developed to allow more flexible deployment. Sensors should be deployed at a range of altitudes, land surface types and aspects, but location should be guided by modelling to highlight areas where obervations could impove model performance the most, such as at marginal locations.
7. Snow chemistry monitoring should be an integral part of any future attempts to couple an electrical model to a hydrology model, due to its large effect on SP signal magnitude. In the absence of this possibility, work should be focused towards empirical relationships between SP signal magnitude and meltwater parameters.
8. Future snow hydrology modelling experiments, including those coupling electrical models, and distributed models, should use modular, factorial or flexible models, such as FSM2, in order to allow quantification of the effect of changing model configurations.

## 6.8 Final conclusions

The main aim of this project was to develop an array for collecting geophysical data in seasonal snow, and use these data to improve a snow hydrology model. This aim has been partially achieved in this work, and the pitfalls and setbacks encountered are instructive for future work in this area.

The array construction was successful. It lasted mostly unscathed for two winters and seemed to be able to last longer if required. The hardware was simple, durable and inexpensive, which means it would be easy to roll out on a wider scale in future. The self potential measurements worked well in the main, although issues of preferential flow along the poles, noisy readings, and poor electrical contact were encountered. In future applications, many of these downsides could be remedied through better experiment design and calibration fairly easily, and with some better luck giving deep snow cover at the field site for the duration of the experiment. Additionally, an array without the constraints of having ERT electrodes too could be orientated better for measuring horizontal variations in the SP signal. In this context, SP has the potential to be used in a wider catchment-scale (or larger) network to detect when melting and liquid water movement begins in the snowpack, before lysimeters could register runoff. An SP array would be easier and cheaper to install than a full lysimeter.

This study has shown that SP measurements are able to be used as a snow hydrology monitor for the duration of a winter season. The SP signals were in general relatively straightforward to relate to meteorological and hydrological variables, and they provided the ability to qualitatively assess internal water fluxes in the absence of direct measurement. Unfortunately the possibility of detecting horizontal or vertical changes in the SP signal, and relating these to liquid flow in the snow, was not realised. This was possibly because the snow was too shallow to detect different timing of meltwater percolation, but the amount of noise was probably a factor too. It is likely that the poles of the array were too close together to detect lateral variations (due to needing to be close together for the ERT) so future experiments should spread the array out over a larger area or along a longer line.

The ERT measurements were evidently much less successful than the SP. While this project failed to get any good ERT data, lessons have been learned and hopefully, should anyone attempt similar work in future, they will be able to look at some of the problems encountered here and be able to take steps to mitigate these risks. Future work should include laboratory work to build on the experiments carried out here, and evaluate the performance of different electrode designs and power supply arrangements before deployment in the field.

The second part of the overarching aim of this project was to use geophysical data to improve the representation of liquid water in a snow model. Due to the large uncertainties present in the electrical model, this aim was difficult to approach mathematically, and data assimilation techniques were not used. However, the SP data were used qualitatively alongside standard

hydrological data to investigate meltwater generation and flow. The self potential data corroborated the lysimeter data, and also added value by indicating when liquid flow was occurring within the snowpack that had not reached the base of the snow. The measured self potential magnitudes were of the same order to those recorded in previous work.

Along with the lysimeter data, the SP data did guide some parameter adjustment in the snow model to attempt to improve the shape of the runoff curve. This was carried out qualitatively for short period runoff curves, as the statistical metrics used for the long period analysis changed very little when the parameters were changed. This was despite what appeared to be fairly large changes to the shape of the runoff curve, especially when $S_{ir}$ was varied. However, when looking at the different model evaluations carried out over a long period, over short specific runoff events and over a distributed area, the best model configuration depended very much on the circumstances of the evaluation, especially the timescale over which it was evaluated. To compare with SP measurements, short timescales were more useful, and for this the gravitational hydrology gave the best results, along with density as function of age. But the best configuration was different over longer timescales, and different again when used as a distributed model, so this work confirms that it is very difficult to find a one size fits all model that will perform optimally in most situations.

The distributed modelling showed that the configuration that performed well when driven with in situ data at Col de Porte also produced good results over the whole region, but only when the parametrisation for snow fraction as a function of snowdepth was asymptotic - when this was left as a linear function (which produced almost no change at Col de Porte), the change over the whole domain was significant. FSM2 proved to be an adaptable and useful model, running in a few minutes even for several decades or over a reasonably large area. The design of the model allowing the parameters to be set before compilation meant adjusting the model was straightforward and the workflow to evaluate different configurations was easy to implement.

This project has contributed a useful and interesting prototype geophysical array design to the field, and proved that there is utility in measuring self potential to understand internal melt dynamics in snow. It has also helped define the scope of possible future ERT work through highlighting areas for improvement and pitfalls to look out for. The work has shown the immense value of having easy-to-run, open-source physical hydrology models accessible to all, that are adaptable and scaleable with relative ease, designed to investigate the effect of different parameters and configurations. FSM2 provides a blueprint for the future direction of earth system modelling in all fields in its ease of use and flexibility which maximises the possibility for researchers from a variety of backgrounds to use it in their research.

This thesis has also underlined the importance and value of combining model-based investigation with observations. The ability to use observations to improve model simulations is vital. The number of locations for which high quality snow observation datasets are available for long time series is very small, so where we do have them, their exploitation is key to improving model predictions. Simultaneously, models allow us to analyse and understand where best to focus our observation efforts, both on landscape scales, and on centimetre (or smaller) scales within the snowpack, for example in areas where models perform less well. This two-way relationship between observations and models is only going to become more important in the decades to come: whilst land-based observations may remain relatively sparse, remotely-sensed data volumes are increasing and in order to interpret and exploit them to their full potential, processes within the snow must be modelled so that observations can be understood.

Appendix A

# Model evaluation plots

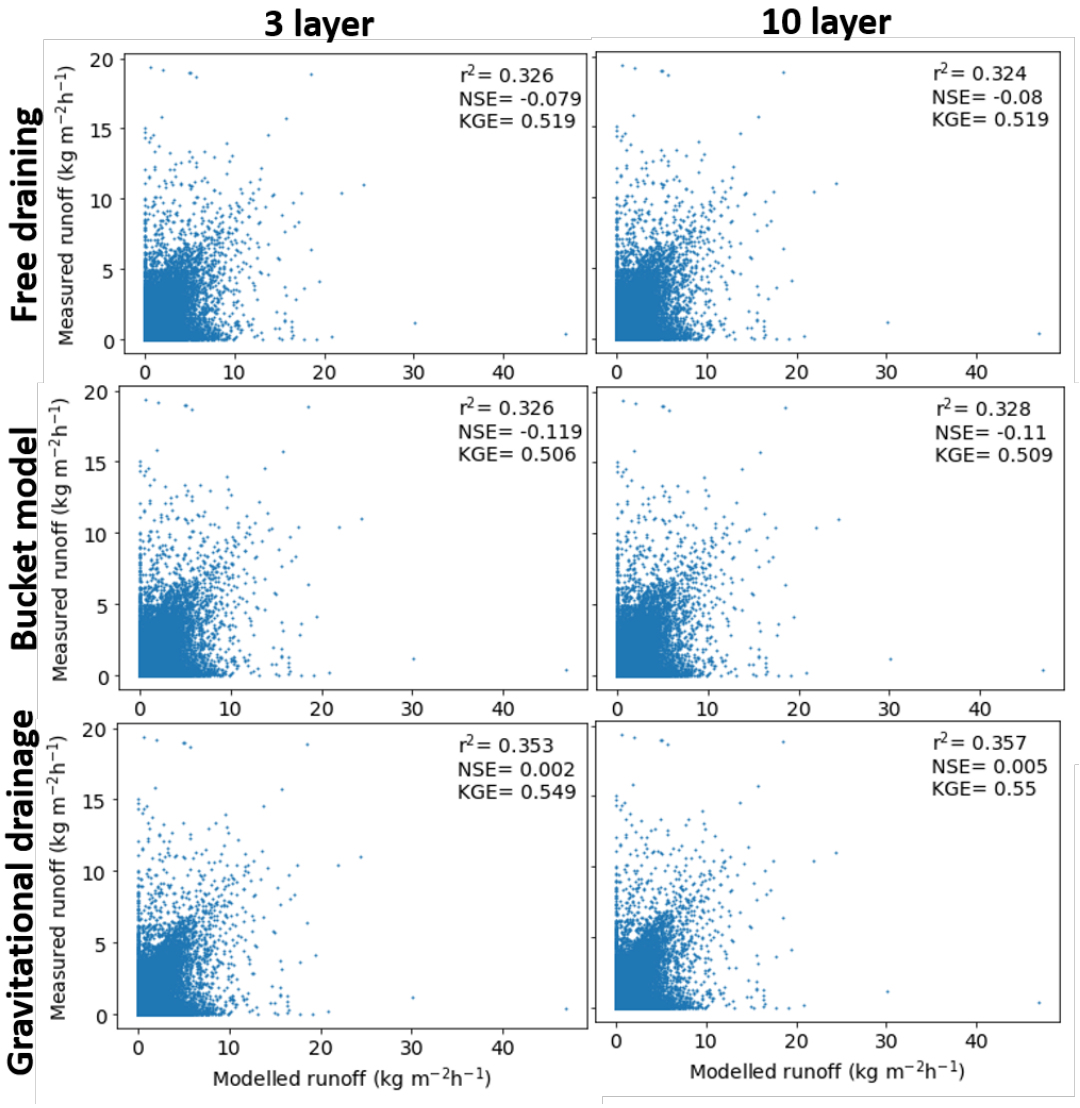


**Figure A.1:** Three and ten layer FSM2 simulations of hourly runoff with density as a function of age

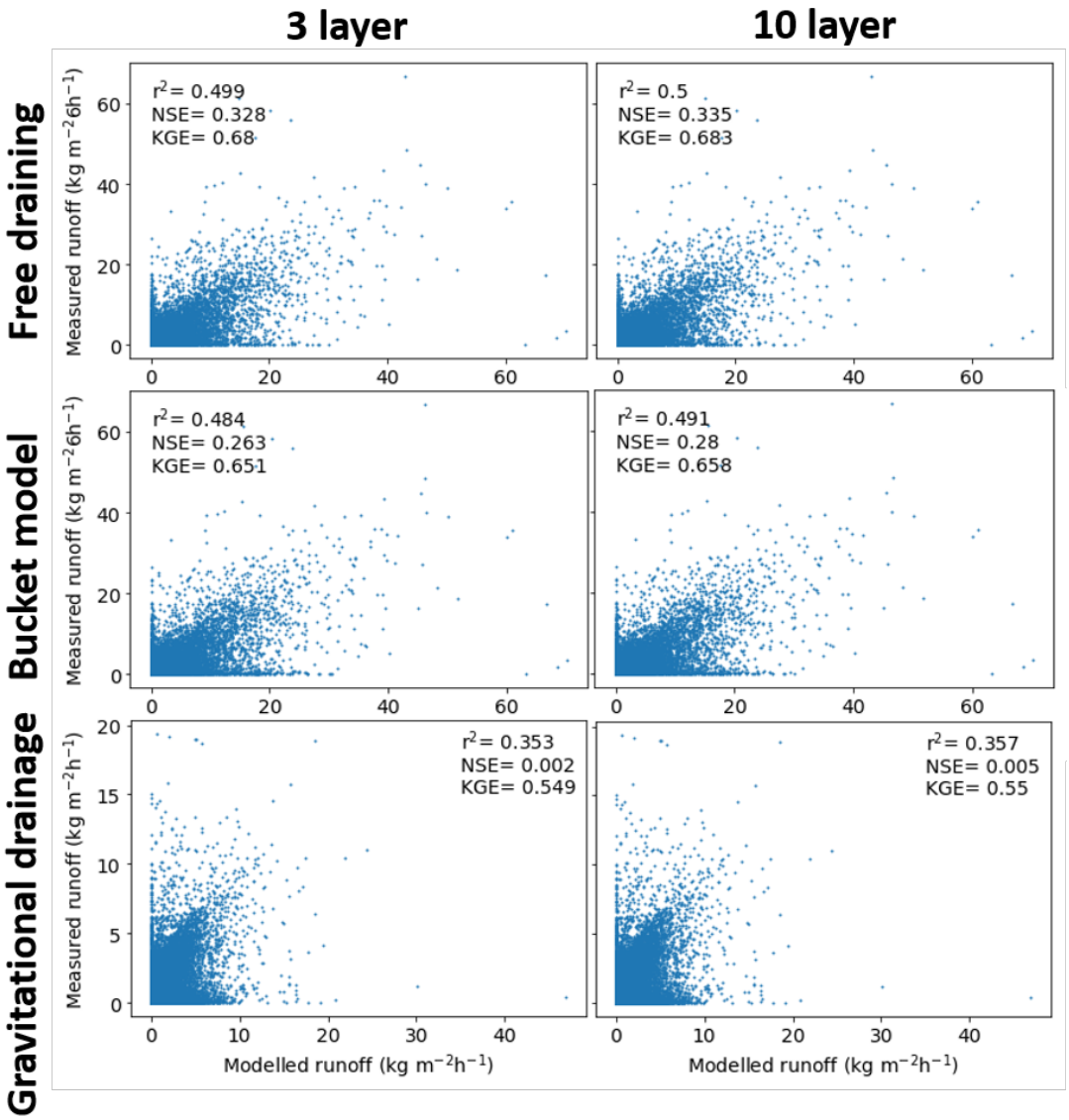


**Figure A.2:** Three and ten layer FSM2 simulations of 6-hourly runoff with density as a function of age

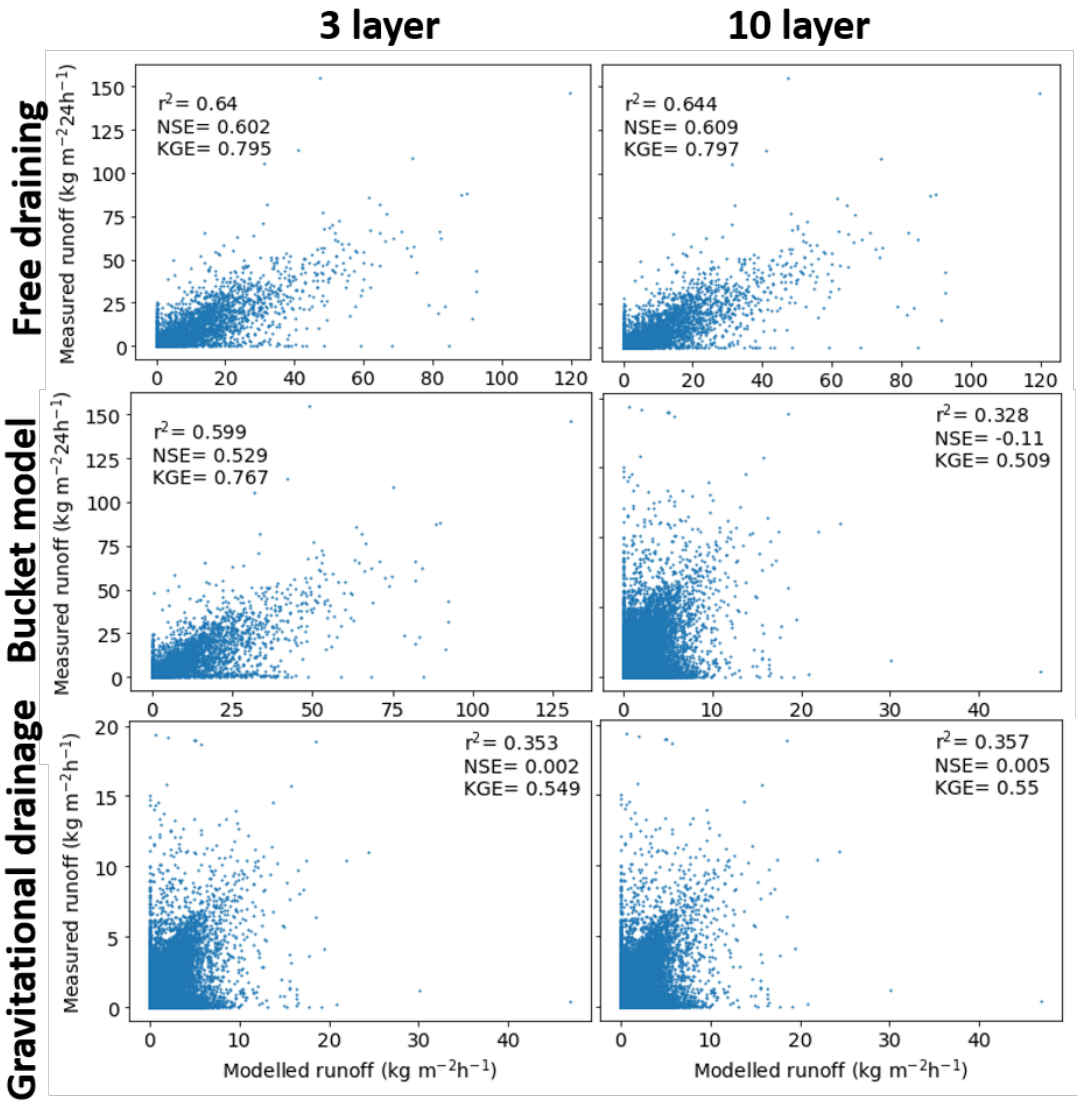


**Figure A.3:** Three and ten layer FSM2 simulations of daily runoff with density as a function of age

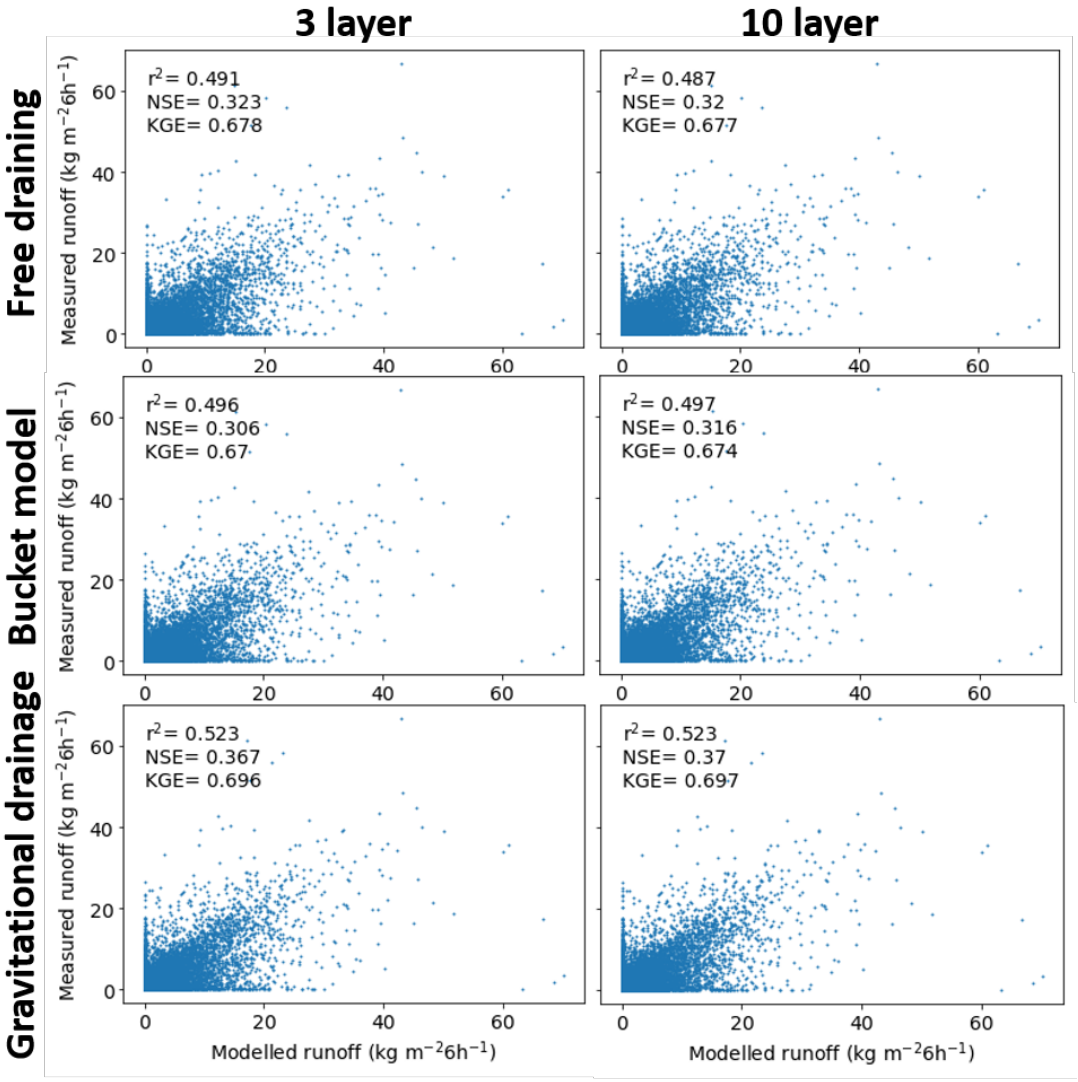


**Figure A.4:** Three and ten layer FSM2 simulations of 6-hourly runoff with density as a function of overburden

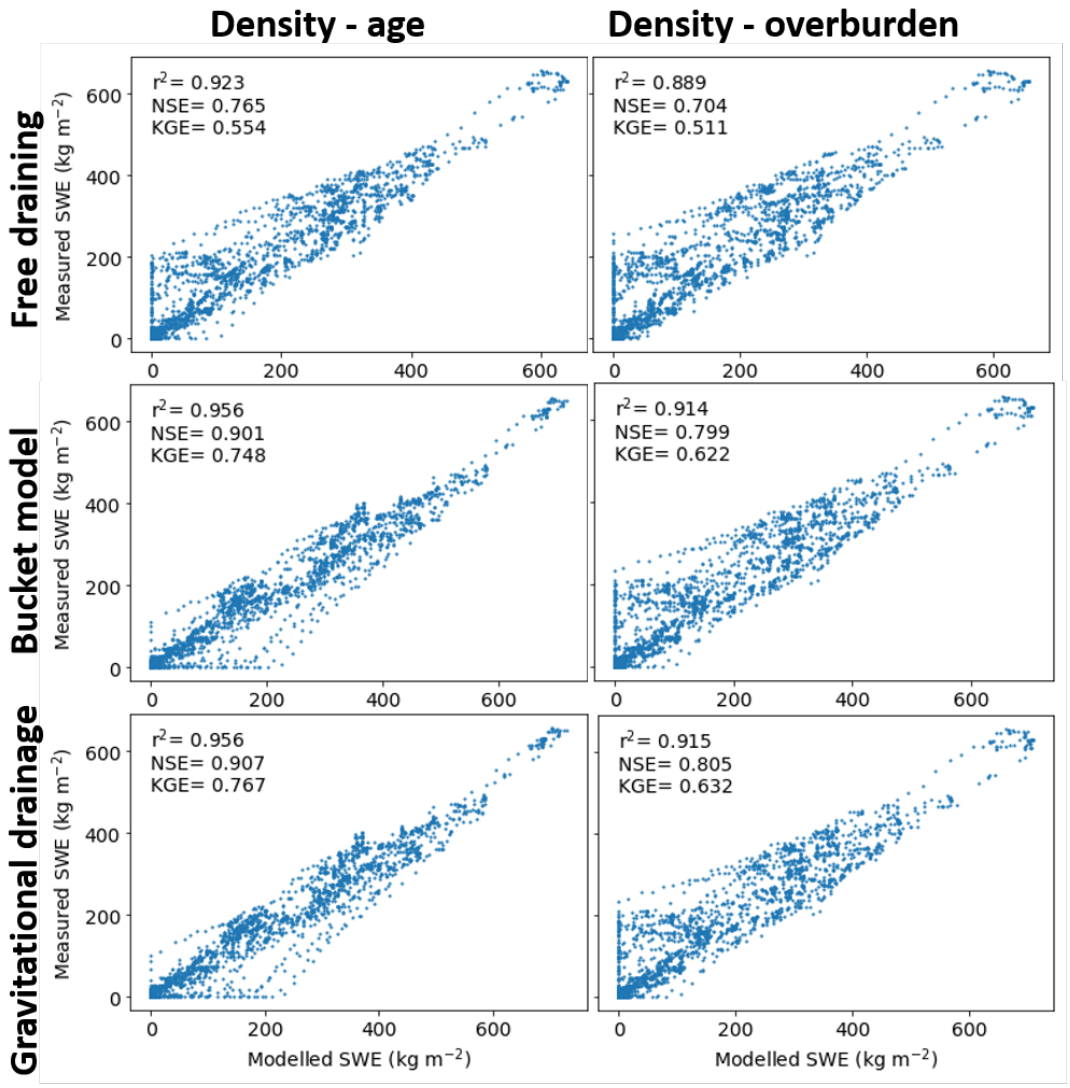


**Figure A.5:** Ten layer FSM2 simulations of SWE

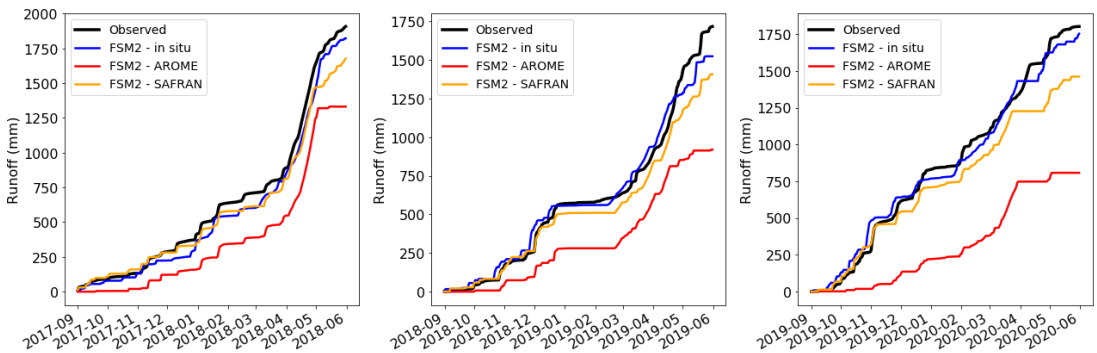


**Figure A.6:** Cumulative runoff for 2017 - 2020 at Col de Porte with density modelled as a function of snow overburden.

# Appendix B

# Gravitational drainage equations

To solve the water balance equation (equation 5.8), snow layer $k$ with ice and liquid masses $I_k$ and $W_k$, and thickness $\Delta z_k$ has volumetric water content

$$\theta_{w,k} = \frac{W_k}{\theta_w \Delta z_k} \tag{B.1}$$

and porosity

$$\phi_k = 1 - \frac{I_k}{\rho_i \Delta z_k}. \tag{B.2}$$

An implicit upwind scheme is is used to discretise the water balance equation

$$\frac{\theta_{w,1}^{(n)} - \theta_{w,1}^{(n-1)}}{\delta t} = \frac{1}{\Delta z_1}\left[Q_1 - \left(\frac{\theta_{w,1}^{(n)} - \theta_{r,1}}{\phi_1 - \theta_{r,1}}\right)^3\right], k = 1, \tag{B.3}$$

$$\frac{\theta_{w,1}^{(n)} - \theta_{w,k}^{(n-1)}}{\delta t} = \frac{1}{\Delta z_k}\left[\left(\frac{\theta_{w,k-1}^{(n)} - \theta_{r,k-1}}{\phi_{k-1} - \theta_{r,k-1}}\right)^3 - \left(\frac{\theta_{w,k}^{(n)} - \theta_{r,k}}{\phi_k - \theta_{r,k}}\right)^3\right], 1 < k \leq N. \tag{B.4}$$

$k = 1$ for the top snow layer, so the flux into this layer from above is $Q_1 = (M + R_f)/\rho_w$ where $M$ is input of surface melting and $R_f$ is rainfall. Layer liquid water contents at the end of timestep $n$ are found by the Newton-Raphson method:

$$r_1 = \frac{\theta_{w,1}^{(n)} - \theta_{w,1}^{(n-1)}}{\delta t} + \frac{1}{\Delta z_1}\left[Q_1 - \left(\frac{\theta_{w,1}^{(n)} - \theta_{r,1}}{\phi_1 - \theta_{r,1}}\right)^3\right] \tag{B.5}$$

$$r_k = \frac{\theta_{w,1}^{(n)} - \theta_{w,k}^{(n-1)}}{\delta t} + \frac{1}{\Delta z_k}\left[\left(\frac{\theta_{w,k}^{(n)} - \theta_{r,k}}{\phi_k - \theta_{r,k}}\right)^3 - \left(\frac{\theta_{w,k+1}^{(n)} - \theta_{r,k+1}}{\phi_{k+1} - \theta_{r,k+1}}\right)^3\right] \tag{B.6}$$

Zeros in the liquid balance residuals are sought by iterating

$$\sum_{k=1}^{N} \frac{\partial r_j}{\partial \theta^{(n)}} \Delta\theta_k + r_j = 0 \tag{B.7}$$

(a bidiagonal matrix solved by forward substitution) and

$$\theta_{w,k}^{(n)} \mapsto \theta_{w,k}^{(n)} + \Delta\theta_k \tag{B.8}$$

Appendix C

# Distributed model evaluation - supplementary plots

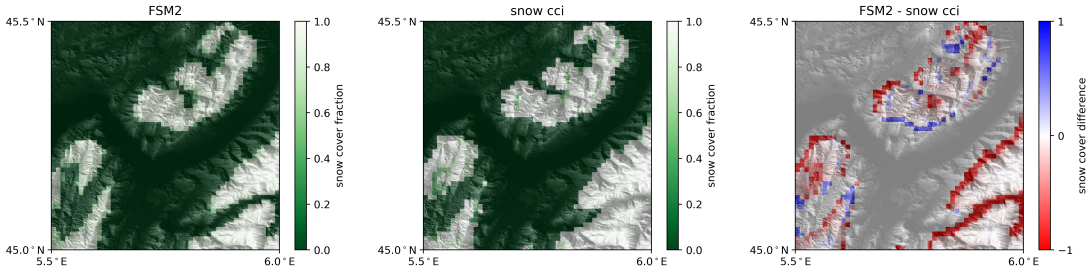


**Figure C.1:** 'Reference' FSM2 modelled, observed and model-observation difference in snow cover fraction on 24th January 2018 over Chartreuse domain.

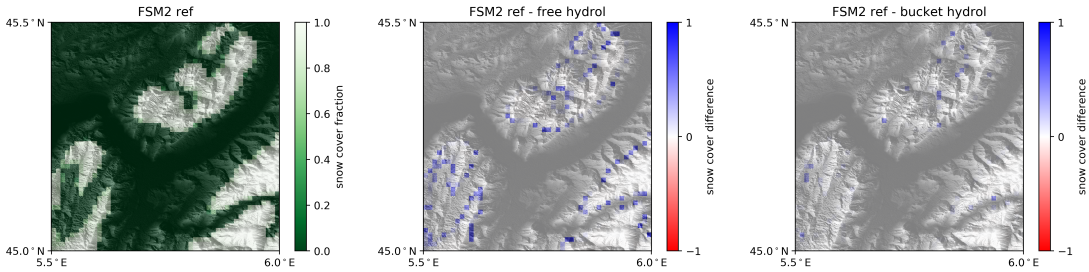


**Figure C.2:** 'Reference' FSM2 compared with free draining and bucket hydrology models on 24th January 2018 over Chartreuse domain.

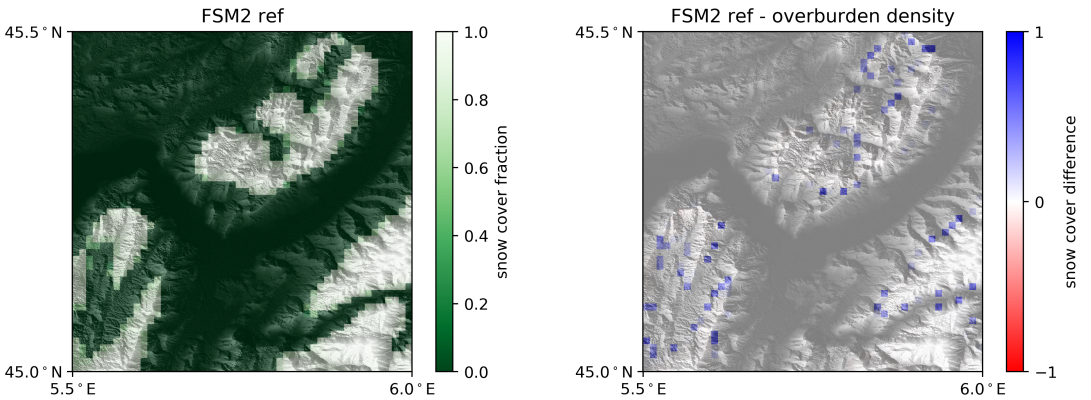


**Figure C.3:** 'Reference' FSM2 compared with density as a function of overburden model on 24th January 2018 over Chartreuse domain.

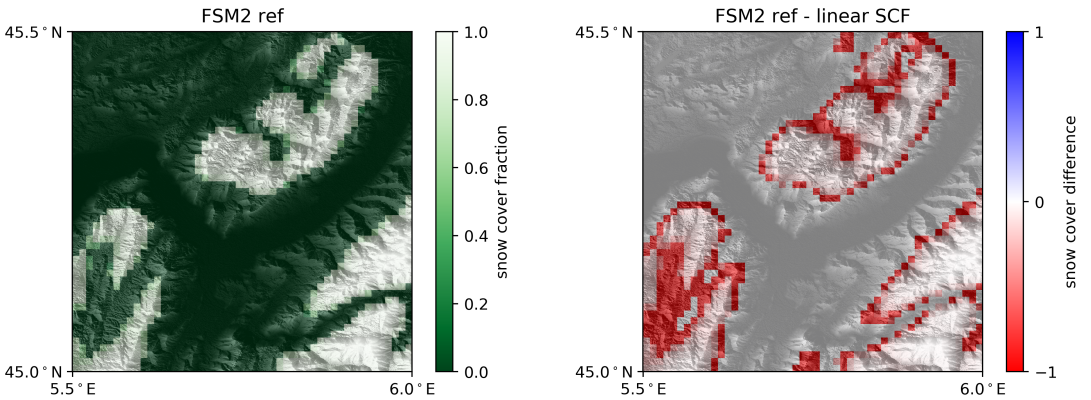


**Figure C.4:** 'Reference' FSM2 compared with snow cover fraction as a linear function of snowdepth on 24th January 2018 over Chartreuse domain.

# Bibliography


Adams, R. M., Houston, L. L., and Weiher, R. F. (2004). *The value of snow and snow information service*.

Albert, M. and Krajeski, G. (1998). A fast, physically based point snowmelt model for use in distributed applications. *Hydrological Processes*, 12(March):1809–1824.

Alonso-González, E., Gutmann, E., Aalstad, K., Fayad, A., Bouchet, M., and Gascoin, S. (2021). Snowpack dynamics in the Lebanese mountains from quasi-dynamically downscaled ERA5 reanalysis updated by assimilating remotely sensed fractional snow-covered area. *Hydrology and Earth System Sciences*, 25(8):4455–4471.

Avanzi, F., Hirashima, H., Yamaguchi, S., Katsushima, T., and De Michele, C. (2016). Observations of capillary barriers and preferential flow in layered snow during cold laboratory experiments. *Cryosphere*, 10(5):2013–2026.

Barnett, T. P., Adam, J. C., and Lettenmaier, D. P. (2005). Potential impacts of a warming climate on water availability in snow-dominated regions. *Nature*, 438(November):303–309.

Barraclough, T. (2014). Strain softening and strain localisation in irreversible deformation of snow.

Bartelt, P. and Lehning, M. (2002). A physical SNOATACK model for the Swiss avalanche warning Part I: numerical model. *Cold Regions Science and Technology*, 35(3):123–145.

Bauman, P. (2005). 2-D resistivity surveying for hydrocarbons—a primer. *CSEG Recorder*, April 2005:25–33.

Best, M. J., Pryor, M., Clark, D. B., Rooney, G. G., Essery, R. L. H., Ménard, C. B., Edwards, J. M., Hendry, M. A., Porson, A., Gedney, N., Mercado, L. M., Sitch, S., Blyth, E., Boucher, O., Cox, P. M., Grimmond, C. S. B., and Harding, R. J. (2011). The Joint UK Land Environment Simulator (JULES), model description – Part 1: Energy and water fluxes. *Geoscientific Model Development*, 4(3):677–699.

Betts, A. K. and Ball, J. H. (1997). Albedo over the boreal forest. *Journal of Geophysical Research: Atmospheres*, 102(D24):28901–28909.

Boone, A. and Etchevers, P. (2001). An Intercomparison of Three Snow Schemes of Varying Complexity Coupled to the Same Land Surface Model: Local-Scale Evaluation at an Alpine Site. *Journal of Hydrometeorology*, 2(4):374–394.

Brun, E., David, P., Sudul, M., and Brunot, G. (1992). A numerical model to simulate snow-cover stratigraphy for operational avalanche forecasting. *Journal of Glaciology*, 38(128):13–22.

Brun, E., Martin, , Simon, V., Gendre, C., and Coleou, C. (1989). An energy and mass model of snow cover suitable for operational avalanche forecasting. *Journal of Glaciology*, 35(121):333–342.

Calonne, N., Flin, F., Morin, S., Lesaffre, B., du Roscoat, S. R., and Geindreau, C. (2011). Numerical and experimental investigations of the effective thermal conductivity of snow. *Geophysical Research Letters*, 38(23).

Calonne, N., Geindreau, C., Flin, F., Morin, S., Lesaffre, B., Rolland du Roscoat, S., and Charrier, P. (2012). 3-D image-based numerical computations of snow permeability: links to specific surface area, density, and microstructural anisotropy. *The Cryosphere*, 6(5):939–951.

Calonne, N., Milliancourt, L., Burr, A., Philip, A., Martin, C. L., Flin, F., and Geindreau, C. (2019). Thermal Conductivity of Snow, Firn, and Porous Ice From 3-D Image-Based Computations. *Geophysical Research Letters*, 46(22):13079–13089.

Campbell, F. M., Nienow, P. W., and Purves, R. S. (2006). Role of the supraglacial snowpack in mediating meltwater delivery to the glacier system as inferred from dye tracer investigations. *Hydrological Processes*, 20(4):969–985.

Chambers, J. E., Wilkinson, P. B., Weller, A. L., Meldrum, P. I., Ogilvy, R. D., and Caunt, S. (2007). Mineshaft imaging using surface and crosshole 3D electrical resistivity tomography: A case history from the East Pennine Coalfield, UK. *Journal of Applied Geophysics*, 62(4):324–337.

Chave, A. D., Jones, A. G., Mackie, R., and Rodi, W. (2012). *The Magnetotelluric Method*. Cambridge University Press, Cambridge.

Clark, M. P., Nijssen, B., and Luce, C. H. (2017). An analytical test case for snow models. *Water Resources Research*, 53(1):909–922.

Clayton, W. S. (2021). Measurement of unsaturated meltwater percolation flux in seasonal snowpack using self-potential. *Journal of Glaciology*, page 1–16.

Colangelo, G., Lapenna, V., Perrone, A., Piscitelli, S., and Telesca, L. (2006). 2D Self-Potential tomographies for studying groundwater flows in the Varco d'Izzo landslide (Basilicata, southern Italy). *Engineering Geology*, 88(3-4):274–286.

Colbeck, S. C. (1972). A theory of water percolation in snow. *Journal of Glaciology*, 11(63):369–385.

Colbeck, S. C. (1974). The capillary effects on water percolation in homogeneous snow. *Journal of Glaciology*, 13(67):85–97.

Colbeck, S. C. (1976). An analysis of water flow in dry snow. *Water Resources Research*, 12(3):523–527.

Coléou, C. and Lesaffre, B. (1998). Irreducible water saturation in snow: experimental results in a cold laboratory. *Annals of Glaciology*, 26:64–68.

Corry, C. E., Demoully, G. T., and Gerety, M. T. (1983). Field Procedure Manual for Self-Potential Surveys. pages 1–52.

Deems, J. S., Painter, T. H., and Finnegan, D. C. (2013). Lidar measurement of snow depth: a review. *Journal of Glaciology*, 59(215):467–479.

Denoth, A. (1994). An electronic device for long-term snow wetness recording. *Annals of Glaciology*.

Deschamps-Berger, C., Gascoin, S., Berthier, E., Deems, J., Gutmann, E., Dehecq, A., Shean, D., and Dumont, M. (2020). Snow depth mapping from stereo satellite imagery in mountainous terrain: evaluation using airborne laser-scanning data. *The Cryosphere*, 14(9):2925–2940.

Di Maio, R., Mauriello, P., Patella, D., Petrillo, Z., Piscitelli, S., Siniscalchi, A., and Veneruso, M. (1997). Self-potential, geoelectric and magnetotelluric studies in Italian active volcanic areas. *Annali di Geofisica*, 40(2):519–537.

Doherty, R., Kulessa, B., Ferguson, A. S., Larkin, M. J., Kulakov, L. A., and Kalin, R. M. (2010). A microbial fuel cell in contaminated ground delineated by electrical self-potential and normalized induced polarization data. *Journal of Geophysical Research: Biogeosciences*, 115(G3):1–11.

Domine, F., Picard, G., Morin, S., Barrere, M., Madore, J.-B., and Langlois, A. (2019). Major Issues in Simulating Some Arctic Snowpack Properties Using Current Detailed Snow Physics Models: Consequences for the Thermal Regime and Water Budget of Permafrost. *Journal of Advances in Modeling Earth Systems*, 11(1):34–44.

Douville, H., Royer, J., and Mahfouf, J. (1995). A new snow parameterization for the Meteo-France climate model. *Climate Dynamics*, 35:21–35.

Durand, Y., Brun, E., Merindol, L., Guyomarc'h, G., Lesaffre, B., and Martin, E. (1993). A meteorological estimation of relevant parameters for snow models. *Annals of glaciology*, 18:65–71.

Dutra, E., Balsamo, G., Viterbo, P., Miranda, P. M. A., Beljaars, A., Schär, C., and Elder, K. (2010). An Improved Snow Scheme for the ECMWF Land Surface Model: Description and Offline Validation. *Journal of Hydrometeorology*, 11(4):899 – 916.

Dutra, E., Viterbo, P., Miranda, P. M. A., and Balsamo, G. (2012). Complexity of Snow Schemes in a Climate Model and Its Impact on Surface Energy and Hydrology. *Journal of Hydrometeorology*, 13(2):521–538.

EAWS, E. (2021). Fatalities statistics.

Egbert, G. D. and Booker, J. R. (1992). Very long period magnetotellurics at Tucson observatory: implications for mantle conductivity. *Journal of Geophysical Research*, 97(B11).

Eisenberg, D. and Warner, K. E. (2005). Effects of Snowfalls on Motor Vehicle Collisions, Injuries, and Fatalities. *American Journal of Public Health*, 95(1):120–124. PMID: 15623871.

Essery, R. (2015). A factorial snowpack model (FSM 1.0). *Geoscientific Model Development*, 8(12):3867–3876.

Essery, R., Kontu, A., Lemmetyinen, J., Dumont, M., and Ménard, C. B. (2016). A 7-year dataset for driving and evaluating snow models at an Arctic site (Sodankylä, Finland). *Geoscientific Instrumentation, Methods and Data Systems*, 5(1):219–227.

Essery, R., Morin, S., Lejeune, Y., and B Ménard, C. (2013). A comparison of 1701 snow models using observations from an alpine site. *Advances in Water Resources*, 55:131–148.

Estilow, T. W., Young, A. H., and Robinson, D. A. (2015). A long-term Northern Hemisphere snow cover extent data record for climate studies and monitoring. *Earth System Science Data*, 7(1):137–142.

Etchevers, P., Martin, E., Brown, R., Fierz, C., Lejeune, Y., Bazile, E., Boone, a., Dai, Y.-J., Essery, R. L. H., Fernandez, a., Gusev, Y., Jordan, R., Koren, V., Kowalczyk, E., Nasonova, O., Pyles, R. D., Schlosser, a., Shmakin, a. B., Smirnova, T. G., Strosser, U., Verseghy, D., Yamazaki, T., Yang, Z.-L., Nasonova, N. O., and Strasser, U. (2004). Validation of the surface energy budget simulated by several snow models. *Annals of Glaciology*, 38:150–158.

Fierz, C., Armstrong, R., Durand, Y., Etchevers, P., Greene, E., McClung, D., Nishimura, K., Satyawali, P., and Sokratov, S. (2009). The international classification for seasonal snow on the ground. *IHP-VII Technical Documents in Hydrology*, 83(1):90.

Forster, R. R., Box, J. E., Van Den Broeke, M. R., Miège, C., Burgess, E. W., Van Angelen, J. H., Lenaerts, J. T., Koenig, L. S., Paden, J., Lewis, C., Gogineni, S. P., Leuschen, C., and McConnell, J. R. (2014). Extensive liquid meltwater storage in firn within the Greenland ice sheet. *Nature Geoscience*, 7(2):95–98.

Foster, J., Hall, D., Kelly, R., and Chiu, L. (2009). Seasonal snow extent and snow mass in South America using SMMR and SSM/I passive microwave data (1979–2006). *Remote Sensing of Environment*, 113(2):291–305.

Frappart, F., **, G. R., and Famiglietti, J. S. (2011). Water balance of the Arctic drainage system using GRACE gravimetry products. *International Journal of Remote Sensing*, 32(2):431–453.

French, H. and Binley, A. (2004). Snowmelt infiltration: Monitoring temporal and spatial variability using time-lapse electrical resistivity. *Journal of Hydrology*, 297(1-4):174–186.

Friedel, S., Byrdina, S., Jacobs, F., and Zimmer, M. (2004). Self-potential and ground temperature at Merapi volcano prior to its crisis in the rainy season of 2000-2001. *Journal of Volcanology and Geothermal Research*, 134(3):149–168.

Gallet, J.-C., Domine, F., Zender, C. S., and Picard, G. (2009). Measurement of the specific surface area of snow using infrared reflectance in an integrating sphere at 1310 and 1550 nm. *The Cryosphere*, 3(2):167–182.

Gibert, D., Le Mouël, J. L., Lambs, L., Nicollin, F., and Perrier, F. (2006). Sap flow and daily electric potential variations in a tree trunk. *Plant Science*, 171(5):572–584.

Gouttevin, I., Krinner, G., Ciais, P., Polcher, J., and Legout, C. (2012). Multi-scale validation of a new soil freezing scheme for a land-surface model with physically-based hydrology. *The Cryosphere*, 6(2):407–430.

Groisman, P. Y., Karl, T. R., and Knight, R. W. (1994a). Observed Impact of Snow Cover on the Heat Balance and the Rise of Continental Spring Temperatures. *Science*, 263(5144):198–200.

Groisman, P. Y., Karl, T. R., Knight, R. W., and Stenchikov, G. L. (1994b). Changes of Snow Cover, Temperature, and Radiative Heat Balance over the Northern Hemisphere. *Journal of Climate*, 7(11):1633 – 1656.

Guichet, X., Jouniaux, L., and Pozzi, J.-P. (2003). Streaming potential of a sand column in partial saturation conditions. *Journal of Geophysical Research: Solid Earth*, 108(B3).

Günther, D., Marke, T., Essery, R., and Strasser, U. (2019). Uncertainties in Snowpack Simulations—Assessing the Impact of Model Structure, Parameter Choice, and Forcing Data Error on Point-Scale Energy Balance Snow Model Performance.

Gupta, H. V., Kling, H., Yilmaz, K. K., and Martinez, G. F. (2009). Decomposition of the mean squared error and NSE performance criteria: Implications for improving hydrological modelling. *Journal of Hydrology*, 377(1-2):80–91.

Hall, D. K., Comiso, J. C., DiGirolamo, N. E., Shuman, C. A., Box, J. E., and Koenig, L. S. (2013). Variability in the surface temperature and melt extent of the Greenland ice sheet from MODIS. *Geophysical Research Letters*, 40(10):2114–2120.

Hallikainen, M., Halme, P., Takala, M., and Pulliainen, J. (2003). Combined active and passive microwave remote sensing of snow in Finland. In *IGARSS 2003. 2003 IEEE International Geoscience and Remote Sensing Symposium. Proceedings (IEEE Cat. No.03CH37477)*, volume 2, pages 830–832 vol.2.

Hanzer, F., Günther, D., Strasser, U., Premier, V., Callegari, M., Marin, C., and Notarnicola, C. (2020). Process-based simulation of snow cover evolution in ski resorts using the AMUNDSEN model : results and validation Snow management modeling § Physically based snowpack models. *EGU General Assembly 2020*, (May).

Havens, S., Marshall, H.-P., Pielmeier, C., and Elder, K. (2013). Automatic Grain Type Classification of Snow Micro Penetrometer Signals With Random Forests. *IEEE Transactions on Geoscience and Remote Sensing*, 51(6):3328–3335.

He, C., Liou, K.-N., Takano, Y., Chen, F., and Barlage, M. (2019). Enhanced Snow Absorption and Albedo Reduction by Dust-Snow Internal Mixing: Modeling and Parameterization. *Journal of Advances in Modeling Earth Systems*, 11(11):3755–3776.

He, Z. H., Parajka, J., Tian, F. Q., and Blöschl, G. (2014). Estimating degree-day factors from MODIS for snowmelt runoff modeling. *Hydrology and Earth System Sciences*, 18(12):4773–4789.

Heilig, A., Eisen, O., MacFerrin, M., Tedesco, M., and Fettweis, X. (2018). Seasonal monitoring of melt and accumulation within the deep percolation zone of the Greenland Ice Sheet and comparison with simulations of regional climate modeling. *The Cryosphere*, 12(6):1851–1866.

Heilig, A., Mitterer, C., Schmid, L., Wever, N., Schweizer, J., Marshall, H.-P., and Eisen, O. (2015). Seasonal and diurnal cycles of liquid water in snow—Measurements and modeling. *Journal of Geophysical Research: Earth Surface*, 120(10):2139–2154.

Hill, F. F., Browning, K. A., and Bader, M. J. (1981). Radar and raingauge observations of orographic rain over south Wales. *Quarterly Journal of the Royal Meteorological Society*, 107(453):643–670.

Hirashima, H., Yamaguchi, S., Sato, A., and Lehning, M. (2010). Numerical modeling of liquid water movement through layered snow based on new measurements of the water retention curve. *Cold Regions Science and Technology*, 64(2):94–103.

Holmes, J., Chambers, J., Meldrum, P., Wilkinson, P., Boyd, J., Williamson, P., Huntley, D., Sattler, K., Elwood, D., Sivakumar, V., Reeves, H., and Donohue, S. (2020). Four-dimensional electrical resistivity tomography for continuous, near-real-time monitoring of a landslide affecting transport infrastructure in British Columbia, Canada. *Near Surface Geophysics*, 18(4):337–351.

Hottelet, C., Blazkova, S., and Bicik, M. (1994). Application of the ETH snow model to three basins of different character in Central Europe. *Nordic Hydrology (Denmark)*, 25(1):113–128.

Hu, K., Jougnot, D., Huang, Q., Looms, M. C., and Linde, N. (2020). Advancing quantitative understanding of self-potential signatures in the critical zone through long-term monitoring. *Journal of Hydrology*, 585(February):124771.

Humphrey, N. F., Harper, J. T., and Pfeffer, W. T. (2012). Thermal tracking of meltwater retention in Greenland's accumulation area. *Journal of Geophysical Research: Earth Surface*, 117(F1).

Jardani, A., Dupont, J. P., and Revil, A. (2006). Self-potential signals associated with preferential groundwater flow pathways in sinkholes. *Journal of Geophysical Research: Solid Earth*, 111(9):1–13.

Jones, H. G., Pomeroy, J. W., Walker, D. A., and Hohem, R. W. (2001). *Snow ecology*. Cambridge University Press.

Jordan, R. E. (1991). A one-dimensional temperature model for a snow cover: Technical documentation for SNTHERM. 89.

Jordan, R. E., Hardy, J. P., Perron Jr, F. E., and Fisk, D. J. (1999). Air permeability and capillary rise as measures of the pore structure of snow: an experimental and theoretical study. *Hydrological Processes*, 13(12-13):1733–1753.

Kallay, N., Čop, A., Chibowski, E., and Holysz, L. (2003). Reversible charging of the ice–water interface: II. Estimation of equilibrium parameters. *Journal of Colloid and Interface Science*, 259(1):89–96.

Katsushima, T., Kumakura, T., and Takeuchi, Y. (2009). A multiple snow layer model including a parameterization of vertical water channel process in snowpack. *Cold Regions Science and Technology*, 59(2-3):143–151.

Katsushima, T., Yamaguchi, S., Kumakura, T., and Sato, A. (2013). Experimental analysis of preferential flow in dry snowpack. *Cold Regions Science and Technology*, 85:206–216.

Kattelmann, R. (2000). Snowmelt lysimeters in the evaluation of snowmelt models. *Annals of Glaciology*, 31:405–410.

Kay, A. L. (2016). A review of snow in Britain: The historical picture and future projections. *Progress in Physical Geography*, 40(5):676–698.

Kay, J. E., Deser, C., Phillips, A., Mai, A., Hannay, C., Strand, G., Arblaster, J. M., Bates, S. C., Danabasoglu, G., Edwards, J., Holland, M., Kushner, P., Lamarque, J.-F., Lawrence, D., Lindsay, K., Middleton, A., Munoz, E., Neale, R., Oleson, K., Polvani, L., and Vertenstein, M. (2015). The Community Earth System Model (CESM) Large Ensemble Project: A Community Resource for Studying Climate Change in the Presence of Internal Climate Variability. *Bulletin of the American Meteorological Society*, 96(8):1333 – 1349.

Kinar, N. J. and Pomeroy, J. W. (2015). Measurement of the physical properties of the snowpack. *Reviews of Geophysics*, 53:481–544.

Koch, F., Henkel, P., Appel, F., Schmid, L., Bach, H., Lamm, M., Prasch, M., Schweizer, J., and Mauser, W. (2019). Retrieval of Snow Water Equivalent, Liquid Water Content, and Snow Height of Dry and Wet Snow by Combining GPS Signal Attenuation and Time Delay. *Water Resources Research*, 55(5):4465–4487.

Koch, F., Prasch, M., Schmid, L., Schweizer, J., and Mauser, W. (2014). Measuring snow liquid water content with low-cost gps receivers. *Sensors (Switzerland)*, 14(11):20975–20999.

Kodama, M., Nakai, K., Kawasaki, S., and Wada, M. (1979). An application of cosmic-ray neutron measurements to the determination of the snow-water equivalent. *Journal of Hydrology*, 41(1):85–92.

Kokhanovsky, A., Rozanov, V. V., Aoki, T., Odermatt, D., Brockmann, C., Krüger, O., Bouvet, M., Drusch, M., and Hori, M. (2011). Sizing snow grains using backscattered solar light. *International Journal of Remote Sensing*, 32(22):6975–7008.

Krinner, G., Derksen, C., Essery, R., Flanner, M., Hagemann, S., Clark, M., Hall, A., Rott, H., Brutel-Vuilmet, C., Kim, H., Ménard, C. B., Mudryk, L., Thackeray, C., Wang, L., Arduini, G., Balsamo, G., Bartlett, P., Boike, J., Boone, A., Chéruy, F., Colin, J., Cuntz, M., Dai, Y., Decharme, B., Derry, J., Ducharne, A., Dutra, E., Fang, X., Fierz, C., Ghattas, J., Gusev, Y., Haverd, V., Kontu, A., Lafaysse, M., Law, R., Lawrence, D., Li, W., Marke, T., Marks, D., Ménégoz, M., Nasonova, O., Nitta, T., Niwano, M., Pomeroy, J., Raleigh,

M. S., Schaedler, G., Semenov, V., Smirnova, T. G., Stacke, T., Strasser, U., Svenson, S., Turkov, D., Wang, T., Wever, N., Yuan, H., Zhou, W., and Zhu, D. (2018). ESM-SnowMIP: Assessing snow models and quantifying snow-related climate feedbacks. *Geoscientific Model Development*, 11(12):5027–5049.

Kulessa, B. (2003). Cross-coupled flow modeling of coincident streaming and electrochemical potentials and application to subglacial self-potential data. *Journal of Geophysical Research*, 108(B8):2381.

Kulessa, B. (2007). A critical review of the low-frequency electrical properties of ice sheets and glaciers. *Journal of Environmental and Engineering Geophysics*, 12(1):23–36.

Kulessa, B., Chandler, D., Revil, A., and Essery, R. (2012). Theory and numerical modeling of electrical self-potential signatures of unsaturated flow in melting snow. *Water Resources Research*, 48(February):1–18.

Kulessa, B., Hubbard, B., and Brown, G. H. (2006). Time-lapse imaging of subglacial drainage conditions using three-dimensional inversion of borehole electrical resistivity data. *Journal of Glaciology*, 52(176):49–57.

Kulessa, B., Hubbard, B., Brown, G. H., and Becker, J. (2003). Earth tide forcing of glacier drainage. *Geophysical Research Letters*, 30(1):11–1.

Kuras, O., Wilkinson, P. B., Meldrum, P. I., Oxby, L. S., Uhlemann, S., Chambers, J. E., Binley, A., Graham, J., Smith, N. T., and Atherton, N. (2016). Geoelectrical monitoring of simulated subsurface leakage to support high-hazard nuclear decommissioning at the Sellafield Site, UK. *Science of the Total Environment*, 566-567:350–359.

Lafaysse, M., Cluzet, B., Dumont, M., Lejeune, Y., Vionnet, V., and Morin, S. (2017). A multiphysical ensemble system of numerical snow modelling. *Cryosphere*, 11(3):1173–1198.

Lean, H. W., Clark, P. A., Dixon, M., Roberts, N. M., Fitch, A., Forbes, R., and Halliwell, C. (2008). Characteristics of high-resolution versions of the Met Office Unified Model for forecasting convection over the United Kingdom. *Monthly Weather Review*, 136(9):3408–3424.

Legault, J. M., Carriere, D., and Petrie, L. (2008). Synthetic model testing and distributed acquisition dc resistivity results over an unconformity uranium target from the Athabasca Basin, northern Saskatchewan. *The Leading Edge*, 27(1):46–51.

Lehning, M. (2009). R.L. Armstrong and E. Brun, eds. 2008. Snow and climate: physical processes, surface energy exchange and modelling. *Journal of Glaciology*, 55(190):384–384.

Lehning, M., Bartelt, P., Brown, B., Russi, T., Stöckli, U., and Zimmerli, M. (1999). SNOWPACK model calculations for avalanche warning based upon a new network of weather and snow stations. *Cold Regions Science and Technology*, 30(1-3):145–157.

Lejeune, Y., Dumont, M., Panel, J. M., Lafaysse, M., Lapalus, P., Le Gac, E., Lesaffre, B., and Morin, S. (2019). 57 years (1960-2017) of snow and meteorological observations from a mid-altitude mountain site (Col de Porte, France, 1325m of altitude). *Earth System Science Data*, 11(1):71–88.

Leroux, N. R. and Pomeroy, J. W. (2017). Modelling capillary hysteresis effects on preferential flow through melting and cold layered snowpacks. *Advances in Water Resources*, 107:250–264.

Li, D., Wrzesien, M. L., Durand, M., Adam, J., and Lettenmaier, D. P. (2017). How much runoff originates as snow in the western United States, and how will that change in the future? *Geophysical Research Letters*, 44(12):6163–6172.

Liston, G. E., Haehnel, R. B., Sturm, M., Hiemstra, C. A., Berezovskaya, S., and Tabler, R. D. (2007). Simulating complex snow distributions in windy environments using SnowTran-3D. *Journal of Glaciology*, 53(181):241–256.

MacAllister, D. J., Jackson, M. D., Butler, A. P., and Vinogradov, J. (2016). Tidal influence on self-potential measurements. *Journal of Geophysical Research: Solid Earth*, 121(12):8432–8452.

Marchenko, S. A., van Pelt, W. J. J., Pettersson, R., Pohjola, V. A., and Reijmer, C. H. (2021). Water content of firn at Lomonosovfonna, Svalbard, derived from subsurface temperature measurements. *Journal of Glaciology*, page 1–12.

Masson, V., Champeaux, J.-L., Chauvin, F., Meriguet, C., and Lacaze, R. (2003). A global database of land surface parameters at 1-km resolution in meteorological and climate models. *Journal of Climate*, 16(9):1261 – 1282.

Matzl, M. and Schneebeli, M. (2006). Measuring specific surface area of snow by near-infrared photography. *Journal of Glaciology*, 52(179):558–564.

Mazzotti, G., Essery, R., Webster, C., Malle, J., and Jonas, T. (2020). Process-level evaluation of a hyper-resolution forest snow model using distributed multisensor observations. *Water Resources Research*, 56.

Mazzotti, G., Webster, C., Essery, R., and Jonas, T. (2021). Increasing the physical representation of forest-snow processes in coarse-resolution models: Lessons learned from upscaling hyper-resolution simulations. *Water Resources Research*, 57(5):e2020WR029064.

Meyer, J. and Skiles, S. M. (2019). Assessing the Ability of Structure From Motion to Map High-Resolution Snow Surface Elevations in Complex Terrain: A Case Study From Senator Beck Basin, CO. *Water Resources Research*, 55(8):6596–6605.

Miller, C. R., Routh, P. S., Brosten, T. R., and McNamara, J. P. (2008). Application of time-lapse ERT imaging to watershed characterization. *Geophysics*, 73(3):G7–G17.

Mitterer, C., Heilig, A., Schweizer, J., and Eisen, O. (2011). Upward-looking ground-penetrating radar for measuring wet-snow properties. *Cold Regions Science and Technology*, 69(2-3):129–138.

Mollaret, C., Hilbich, C., Pellet, C., Flores-Orozco, A., Delaloye, R., and Hauck, C. (2019). Mountain permafrost degradation documented through a network of permanent electrical resistivity tomography sites. *The Cryosphere*, 13(10):2557–2578.

Moore, J. R., Boleve, A., Sanders, J. W., and Glaser, S. D. (2011). Self-potential investigation of moraine dam seepage. *Journal of Applied Geophysics*, 74(4):277–286.

Morin, S., Lejeune, Y., Lesaffre, B., Panel, J.-M., Poncet, D., David, P., and Sudul, M. (2012). A 18-yr long (1993–2011) snow and meteorological dataset from a mid-altitude mountain site (Col de Porte, France, 1325 m alt.) for driving and evaluating snowpack models. *Earth System Science Data Discussions*, 5(1):29–45.

Mudryk, L., Santolaria-otín, M., and Brutel-vuilmet, C. (2020). in the Evolution of Snow Cover.

Murton, J. B., Kuras, O., Krautblatter, M., Cane, T., Tschofen, D., Uhlemann, S., Schober, S., and Watson, P. (2016). Monitoring rock freezing and thawing by novel geoelectrical and acoustic techniques. *Journal of Geophysical Research: Earth Surface*, 121(12):2309–2332.

Musselman, K. N., Addor, N., Vano, J. A., and Molotch, N. P. (2021). Winter melt trends portend widespread declines in snow water resources. *Nature Climate Change*, 11(5):418–424.

Nagler, T., Schwaizer, G., Keuris, L., Hetzenecker, H., and Metsämäki, S. (2021). ESA Snow Climate Change Initiative (Snow-cci): Daily global Snow Cover Fraction - snow on ground (SCFG) from MODIS (2000-2019), version 1.0. *NERC EDS Centre for Environmental Data Analysis*.

Nash, J. and Sutcliffe, J. (1970). River flow forecasting through conceptual models part I — A discussion of principles. *Journal of Hydrology*, 10(3):282–290.

Niu, G.-Y., Seo, K.-W., Yang, Z.-L., Wilson, C., Su, H., Chen, J., and Rodell, M. (2007). Retrieving snow mass from GRACE terrestrial water storage change with a land surface model. *Geophysical Research Letters*, 34(15).

Notarnicola, C. (2020). Hotspots of snow cover changes in global mountain regions over 2000–2018. *Remote Sensing of Environment*, 243:111781.

Ohmura, A. (2001). Physical basis for the temperature-based melt-index method. *Journal of Applied Meteorology*, 40(4):753 – 761.

Olick, D. (2019). Climate change is taking a toll on the $20 billion winter sports industry - and swanky ski homes could lose value.

Peitzsch, E., Birkeland, K. W., and Hansen, K. J. (2008). Water movement and capillary barriers in a stratified and inclined snowpack. In *International Snow Science Workshop*.

Pérez Díaz, C. L., Muñoz, J., Lakhankar, T., Khanbilvardi, R., and Romanov, P. (2017). Proof of concept: Development of snow liquid water content profiler using CS650 reflectometers at Caribou, ME, USA. *Sensors (Switzerland)*, 17(3).

Petiau, G. (2000). Second Generation of Lead-lead Chloride Electrodes for Geophysical Applications. *Pure and Applied Geophysics*, 157(3):357–382.

Pfeffer, W. T. and Humphrey, N. F. (1996). Determination of timing and location of water movement and ice-layer formation by temperature measurements in sub-freezing snow. *Journal of Glaciology*, 42(141):292–304.

Pielmeier, C. and Schneebeli, M. (2003). Stratigraphy and changes in hardness of snow measured by hand, ramsonde and snow micro penetrometer: a comparison with planar sections. *Cold Regions Science and Technology*, 37(3):393–405. ISSW 2002: International Snow Science Workshop.

Pomeroy, J., Gray, D., and Landine, P. (1993). The Prairie Blowing Snow Model: characteristics, validation, operation. *Journal of Hydrology*, 144(1):165–192.

Priestley, A. and Ewing, S. (2022). Modelling past mountain snow cover in Scotland using a high-resolution snow model and downscaled meteorological reanalysis . Presented at the RSPB Conservation Science Annual Science Meeting, Online.

Priestley, A., Kulessa, B., Essery, R., Lejeune, Y., Le Gac, E., and Blackford, J. (2021). Towards the development of an automated electrical self-potential sensor of melt and rainwater flow in snow. *Journal of Glaciology*, page 1–13.

Pritchard, H. D., Farinotti, D., and Colwell, S. (2021). Measuring Changes in Snowpack SWE Continuously on a Landscape Scale Using Lake Water Pressure. *Journal of Hydrometeorology*, 22(4):795 – 811.

Proksch, M., Löwe, H., and Schneebeli, M. (2015). Density, specific surface area, and correlation length of snow measured by high-resolution penetrometry. *Journal of Geophysical Research: Earth Surface*, 120(2):346–362.

Revil, A., Ahmed, A. S., and Jardani, A. (2017). Self-potential: A Non-intrusive Ground Water Flow Sensor. *Journal of Environmental and Engineering Geophysics*, 22(3):235–247.

Revil, A., Linde, N., Cerepi, A., Jougnot, D., Matthäi, S., and Finsterle, S. (2007). Electrokinetic coupling in unsaturated porous media. *Journal of colloid and interface science*, 313(1):315–327.

Revil, A., Mendonça, C. A., Atekwana, E. A., Kulessa, B., Hubbard, S. S., and Bohlen, K. J. (2010). Understanding biogeobatteries: Where geophysics meets microbiology. *Journal of Geophysical Research: Biogeosciences*, 115(G1):1–22.

Revil, A., Naudet, V., Nouzaret, J., and Pessel, M. (2003). Principles of electrography applied to self-potential electrokinetic sources and hydrogeological applications. *Water Resources Research*, 39(5):1–15.

Revuelto, J., Azorin-Molina, C., Alonso-González, E., Sanmiguel-Vallelado, A., Navarro-Serrano, F., Rico, I., and Ignacio López-Moreno, J. (2017). Meteorological and snow distribution data in the Izas Experimental Catchment (Spanish Pyrenees) from 2011 to 2017. *Earth System Science Data*, 9(2):993–1005.

Richards, L. A. (1931). Capillary conduction of liquids through porous mediums. *Physics*, 1(5):318–333.

Riche, F. and Schneebeli, M. (2013). Thermal conductivity of snow measured by three independent methods and anisotropy considerations. *The Cryosphere*, 7(1):217–227.

Richter, B., van Herwijnen, A., Rotach, M. W., and Schweizer, J. (2020). Sensitivity of modeled snow stability data to meteorological input uncertainty. *Natural Hazards and Earth System Sciences*, 20(11):2873–2888.

Roberts, N. M. and Lean, H. W. (2008). Scale-selective verification of rainfall accumulations from high-resolution forecasts of convective events. *Monthly Weather Review*, 136(1):78–97.

Rucker, D., Loke, M., Levitt, M., and Noonan, G. (2010). Electrical-resistivity characterization of an industrial site using long electrodes. *Geophysics Special Section - Hydrogeophysics - electric and electromagnetic methods*.

Scher, S. and Messori, G. (2019). How global warming changes the difficulty of synoptic weather forecasting. *Geophysical Research Letters*, 46(5):2931–2939.

Schmid, L., Heilig, A., Mitterer, C., Schweizer, J., Maurer, H., Okorn, R., and Eisen, O. (2014). Continuous snowpack monitoring using upward-looking ground-penetrating radar technology. *Journal of Glaciology*, 60(221):509–525.

Schneebeli, M. (1995). Development and stability of preferential flow paths in a layered snowpack. *Biogeochemistry of Seasonally Snow Covered Basins*, 228.

Schneebeli, M., Coléou, C., Touvier, F., and Lesaffre, B. (1998). Measurement of density and wetness in snow using time-domain reflectometry. *Annals of Glaciology*, 26:69–72.

Schneebeli, M., Pielmeier, C., and Johnson, J. B. (1999). Measuring snow microstructure and hardness using a high resolution penetrometer. *Cold Regions Science and Technology*, 30(1):101–114.

Schneebeli, M. and Sokratov, S. A. (2004). Tomography of temperature gradient metamorphism of snow and associated changes in heat conductivity. *Hydrological Processes*, 18(18):3655–3665.

Sheshadri, A., Borrus, M., Yoder, M., and Robinson, T. (2021). Midlatitude Error Growth in Atmospheric GCMs: The Role of Eddy Growth Rate. *Geophysical Research Letters*, 48(23):e2021GL096126. e2021GL096126 2021GL096126.

Shimizu, H. (1970). Air permeability of deposited snow. *Contributions from the Institute of Low Temperature Science*.

Sicart, J. E., Hock, R., and Six, D. (2008). Glacier melt, air temperature, and energy balance in different climates: The Bolivian Tropics, the French Alps, and northern Sweden. *Journal of Geophysical Research: Atmospheres*, 113(D24).

Sill, W. R. (1983). Self-potential modeling from primary flows. *Geophysics*, 48(1):76–86.

Smith, S. A., Vosper, S. B., and Field, P. R. (2015). Sensitivity of orographic precipitation enhancement to horizontal resolution in the operational Met Office Weather forecasts. *Meteorological Applications*, 22(1):14–24.

Sommer, W. and Fiel, R. (2009). Snow Pack Analyser ( SPA ) for snow water equivalent ( SWE ) and liquid water content. (November):1–10.

Sommerfeld, R. A., Mosier, A. R., and Musselman, R. C. (1993). CO2, CH4 and N2O flux through a Wyoming snowpack and implications for global budgets. *Nature*, 361(6408):140–142.

Stein, J. (1997). Monitoring the dry density and the liquid water content of snow using time domain reflectometry (TDR). *Cold Regions Science and Technology*, 25:123–136.

Steppuhn, H., Gray, D. M., and Male, D. H. (1981). *Snow and Agriculture. In The Handbook of snow: Principles, processes, management and use*. Pergamon Press.

Stillman, D. E., MacGregor, J. A., and Grimm, R. E. (2013). The role of acids in electrical conduction through ice. *Journal of Geophysical Research: Earth Surface*, 118(1):1–16.

Sturm, M., Holmgren, J., König, M., and Morris, K. (1997). The thermal conductivity of seasonal snow. *Journal of Glaciology*, 43(143):26–41.

Sundström, N., Gustafsson, D., Kruglyak, A., and Lundberg, A. (2012). Field evaluation of a new method for estimation of liquid water content and snow water equivalent of wet snowpacks with GPR. *Hydrology Research*, 44(4):600–613.

Takala, M., Pulliainen, J., Metsamaki, S. J., and Koskinen, J. T. (2009). Detection of snowmelt using spaceborne microwave radiometer data in eurasia from 1979 to 2007. *IEEE Transactions on Geoscience and Remote Sensing*, 47(9):2996–3007.

Tang, Y., Lean, H. W., and Bornemann, J. (2013). The benefits of the Met Office variable resolution NWP model for forecasting convection. *Meteorological Applications*, 20(4):417–426.

Tape, K. D., Rutter, N., Marshall, H. P., Essery, R., and Sturm, M. (2010). Instruments and methods recording microscale variations in snowpack layering using near-infrared photography. *Journal of Glaciology*, 56(195):75–80.

Tedesco, M. and Miller, J. (2007). Observations and statistical analysis of combined active–passive microwave space-borne data and snow depth at large spatial scales. *Remote Sensing of Environment*, 111(2):382–397. Remote Sensing of the Cryosphere Special Issue.

Tedesco, M. and Monaghan, A. J. (2009). An updated Antarctic melt record through 2009 and its linkages to high-latitude and tropical climate variability. *Geophysical Research Letters*, 36(18).

Thompson, S., Kulessa, B., and Luckman, A. (2012). Integrated electrical resistivity tomography (ERT) and self-potential (SP) techniques for assessing hydrological processes within glacial lake moraine dams. *Journal of Glaciology*, 58(211):849–858.

Thompson, S. S., Kulessa, B., Benn, D. I., and Mertes, J. R. (2017). Anatomy of terminal moraine segments and implied lake stability on Ngozumpa Glacier, Nepal, from electrical resistivity tomography (ERT). *Scientific Reports*, 7(1):1–12.

Thompson, S. S., Kulessa, B., Essery, R. L., and Lüthi, M. P. (2016). Bulk meltwater flow and liquid water content of snowpacks mapped using the electrical self-potential (SP) method. *Cryosphere*, 10(1):433–444.

Tiuri, M., Sihvola, A., Nyfors, E., and Hallikaiken, M. (1984). The Complex Dielectric Constant of Snow at Microwave Frequencies. *IEEE J. Oceanic. Eng.*, 9(5):377–382.

Todd Walter, M., Brooks, E. S., McCool, D. K., King, L. G., Molnau, M., and Boll, J. (2005). Process-based snowmelt modeling: does it require more input data than temperature-index modeling? *Journal of Hydrology*, 300(1):65–75.

Tsai, Y.-L. S., Dietz, A., Oppelt, N., and Kuenzer, C. (2019). Remote Sensing of Snow Cover Using Spaceborne SAR: A Review. *Remote Sensing*, 11(12).

Tsokas, G. N., Tsourlos, P. I., Vargemezis, G., and Novack, M. (2008). Non-destructive electrical resistivity tomography for indoor investigation: the case of Kapnikarea Church in Athens. *Archaeological Prospection*, 15(1):47–61.

Tuzet, F., Dumont, M., Lafaysse, M., Picard, G., Arnaud, L., Voisin, D., Lejeune, Y., Charrois, L., Nabat, P., and Morin, S. (2017). A multilayer physically based snowpack model simulating direct and indirect radiative impacts of light-absorbing impurities in snow. *Cryosphere*, 11(6):2633–2653.

Uhlemann, S., Dafflon, B., Peterson, J., Ulrich, C., Shirley, I., Michail, S., and Hubbard, S. S. (2021). Geophysical monitoring shows that spatial heterogeneity in thermohydrological dynamics reshapes a transitional permafrost system. *Geophysical Research Letters*, 48(6):e2020GL091149. e2020GL091149 2020GL091149.

Valkonen, T., Stoll, P., Batrak, Y., Køltzow, M., Schneider, T. M., Stigter, E. E., Aashamar, O. B., Støylen, E., and Jonassen, M. O. (2020). Evaluation of a sub-kilometre NWP system in an Arctic fjord-valley system in winter, journal = Tellus A: Dynamic Meteorology and Oceanography. 72(1):1–21.

Valéry, A., Andréassian, V., and Perrin, C. (2014). 'As simple as possible but not simpler': What is useful in a temperature-based snow-accounting routine? Part 1 – Comparison of six snow accounting routines on 380 catchments. *Journal of Hydrology*, 517:1166–1175.

Verseghy, D. L. (1991). Class—A Canadian land surface scheme for GCMS. I. Soil model. *International Journal of Climatology*, 11(2):111–133.

Vikhamar-Schuler, D., Hanssen-Bauer, I., Schuler, T. V., Mathiesen, S. D., and Lehning, M. (2013). Use of a multilayer snow model to assess grazing conditions for reindeer. *Annals of Glaciology*, 54(62):214–226.

Vionnet, V., Brun, E., Morin, S., Boone, A., Faroux, S., Le Moigne, P., Martin, E., and Willemet, J. M. (2012). The detailed snowpack scheme Crocus and its implementation in SURFEX v7.2. *Geoscientific Model Development*, 5(3):773–791.

Viviroli, D., Zappa, M., Gurtz, J., and Weingartner, R. (2009). An introduction to the hydrological modelling system PREVAH and its pre- and post-processing-tools. *Environmental Modelling Software*, 24(10):1209–1222.

Vosper, S. B. (2004). Inversion effects on mountain lee waves. *Quarterly Journal of the Royal Meteorological Society*, 130(600):1723–1748.

Voytek, E. B., Barnard, H. R., Jougnot, D., and Singha, K. (2019). Transpiration- and precipitation-induced subsurface water flow observed using the self-potential method. *Hydrological Processes*, 33(13):1784–1801.

Wang, L., Wolken, G. J., Sharp, M. J., Howell, S. E. L., Derksen, C., Brown, R. D., Markus, T., and Cole, J. (2011). Integrated pan-Arctic melt onset detection from satellite active and passive microwave measurements, 2000–2009. *Journal of Geophysical Research: Atmospheres*, 116(D22).

Wang, T., Ottle, C., Boone, A., Ciais, P., Brun, E., Morin, S., Krinner, G., Piao, S., and Peng, S. (2013). Evaluation of an improved intermediate complexity snow scheme in the ORCHIDEE land surface model. *Journal of Geophysical Research: Atmospheres*, 118(12):6064–6079.

Warren, S. G. (1984). Impurities in Snow: Effects on Albedo and Snowmelt (Review). *Annals of Glaciology*, 5:177–179.

Weigand, M., Wagner, F. M., Limbrock, J. K., Hilbich, C., Hauck, C., and Kemna, A. (2020). A monitoring system for spatiotemporal electrical self-potential measurements in cryospheric environments. *Geoscientific Instrumentation, Methods and Data Systems*, 9(2):317–336.

Wever, N., Fierz, C., Mitterer, C., Hirashima, H., and Lehning, M. (2014). Solving Richards Equation for snow improves snowpack meltwater runoff estimations in detailed multi-layer snowpack model. *Cryosphere*, 8(1):257–274.

Wever, N., Schmid, L., Heilig, A., Eisen, O., Fierz, C., and Lehning, M. (2015). Verification of the multi-layer SNOWPACK model with different water transport schemes. *Cryosphere*, 9(6):2271–2293.

Wilkinson, P. B., Chambers, J. E., Meldrum, P. I., Ogilvy, R. D., Mellor, C. J., and Caunt, S. (2005). A Comparison of Self-Potential Tomography with Electrical Resistivity Tomography for the Detection of Abandoned Mineshafts. *Journal of engineering and environmental geophysics*, 10(4):381–389.

Williams, M. W., Erickson, T. A., and Petrzelka, J. L. (2010). Visualizing meltwater flow through snow at the centimetre-to-metre scale using a snow guillotine. *Hydrological Processes*, 24(15):2098–2110.

WMO (2019). Essential climate variables.

Würzer, S., Jonas, T., Wever, N., and Lehning, M. (2016). Influence of Initial Snowpack Properties on Runoff Formation during Rain-on-Snow Events. *Journal of Hydrometeorology*, 17(6):1801–1815.

Würzer, S., Wever, N., Juras, R., Lehning, M., and Jonas, T. (2017). Modelling liquid water transport in snow under rain-on-snow conditions - Considering preferential flow. *Hydrology and Earth System Sciences*, 21(3):1741–1756.

Yamaguchi, S., Katsushima, T., Sato, A., and Kumakura, T. (2010). Water retention curve of snow with different grain sizes. *Cold Regions Science and Technology*, 64(2):87–93.

Zege, E., Katsev, I., Malinka, A., Prikhach, A., Heygster, G., and Wiebe, H. (2011). Algorithm for retrieval of the effective snow grain size and pollution amount from satellite measurements. *Remote Sensing of Environment*, 115(10):2674–2685.